The Theory and Application of Optical Diagnostic Techniques in the Combustion Chamber of a Diesel Engine

Zur Erlangung des akademischen Grades
Doktor der Ingenieurwissenschaften
der Fakultät für Maschinenbau
Karlsruher Institut für Technologie (KIT)

genehmigte
Dissertation
von

M.Sc. Stephen Busch

aus Wheatridge

Tag der mündlichen Prüfung *17.05.2013*
Hauptreferent: Prof. Dr.-Ing. Ulrich Spicher
Korreferent: Prof. Dr.-Ing. Martin Gabi

Foreword from the Author

This dissertation was written during my time at the Institut für Kolbenmaschinen at the Karlsruhe Institute of Technology. It is the result of over three years of work within the Deutsche Forschungsgemeinschaft's Collaborative Research Centre 606, subproject C4. This project demanded the very best work that I was capable of and repeatedly revealed the limits of my talents. Any part of this thesis that can be considered a success would not have been possible without the help and the support of my advisors, coworkers, family, friends, and Lord and Savior. With these words I express my sincere gratitude to those who helped me.

First, I am grateful to Professor Spicher for giving me the opportunity to earn my doctorate under his supervision at the Institut für Kolbenmaschinen. The trust that he placed in me and the freedom that he gave me to learn and explore were much appreciated. Thanks are also due to Professor Gabi for his willingness in taking on the role of second examiner.

I thank Dr.-Ing. Heiko Kubach for helping me to secure the scholarship that allowed me to get started as a doctoral candidate at the IFKM. Dr.-Ing. Uwe Wagner is to be thanked for his unwavering support and trust throughout my project. I very much appreciate the help and technical support with issues in the test bench that I received from Dr.-Ing. Sören Bernhardt. My group leader, Dipl.-Ing. Jürgen Pfeil, was always there when I needed a steady hand or some sound technical advice, so I thank him for his support.

My thanks go to Mr. Marcus Weber for the extraordinary and tedious technical support in the test bench that my project required. I am grateful to Mr. Ernst Hummel and the other technicians in the machine shop who patiently and reliably produced countless parts in support of my project and made me a better mechanical engineer. Mr. Michael Busch is to be thanked for his IT support and for faithfully maintaining so many machines on which my work depended.

The image-splitting optical relays that were used in this work could not have been successfully implemented without the selfless support that I received from Dr. Marcus Butzbach, for which I am very grateful. The cooperation with the Institute for Chemical Technology and Polymer Chemistry, and in particular with Professor Dr. Rainer Suntz and Dr.-Chem. Martin Roßbach in the scope of the RAYLIX investigations was an honor and a privilege for which I am also grateful. I thank the doctoral candidates at the Institut für Kolbenmaschinen for the many helpful discussions and particularly Dipl.-Ing. Florian Bach for the productive and enjoyable atmosphere in our office.

I thank Dr.-Ing. Uwe Wagner, Dipl.-Ing. Jürgen Pfeil, and Dipl.-Wi.-Ing. Andreas Binde for proofreading this dissertation.

I am grateful to my family for the constant love and support they have shown me. I cannot begin to express my gratitude to my parents for the sacrifices they made to provide me with an education.

Finally, I thank my Lord and Savior for the many blessings He has bestowed upon me, but especially for patience, clarity, forgiveness, and perseverance. This work is dedicated to His glory.

The Theory and Application of Optical Diagnostic Techniques in the Combustion Chamber of a Diesel Engine

Zusammenfassung

Die Entwicklung moderner Dieselbrennverfahren hinsichtlich minimierter Abgasemissionen und der gleichzeitigen Beibehaltung guter Wirkungsgrade erfordert weitere Kenntnisse über die zugrunde liegenden Phänomene, die im Brennraum stattfinden. Zu diesem Zweck werden aufwändige Simulationstools wie zum Beispiel sogenannte Large Eddy Simulations (LES) in Kombination mit reduzierten chemischen Reaktionsmechanismen eingesetzt. Die erfolgreiche Umsetzung solcher Simulationen erfordert unter anderem die Validierung und Abstimmung mit am Motorenprüfstand experimentell gewonnenen Messdaten, die häufig optisch erfasst werden. Gegenstand der vorliegenden Arbeit ist die Umsetzung ausgewählter optischer Messtechniken in einem neuen, optisch zugänglichen Heavy Duty Dieselmotor und die Analyse der am Prüfstand gewonnenen Ergebnisse vor dem Hintergrund des heutigen Wissenstands. Der Schwerpunkt dabei liegt auf der Rußbildung bzw. auf der Rußoxidation.

In Kapitel 1 wird eine kurze Einleitung in das Thema gegeben. Kapitel 2 befasst sich mit den Grundlagen der Dieselmotorischen Verbrennung, den für Dieselmotoren relevanten Schadstoffbildungsprozessen und dem Stand der Technik im Bereich Dieselmotoren der Heavy Duty Klasse. Bei Dieselmotoren mit Direkteinspritzung wird in der Nähe des oberen Totpunkts flüssiger Kraftstoff unter sehr hohem Druck in eine heiße, dichte Umgebung mit einer Mehrlochdüse eingespritzt. Durch das Air-Entrainment gelangt heiße Luft in den Kraftstoffstrahlen und sorgt für die Erhitzung und Verdampfung des Kraftstoffes. Die Temperatur des dabei entstehenden Luft-Kraftstoff-Gemisches liegt oberhalb der Zündgrenze, so dass nach einem kurzen Verzug es zu einer Selbstzündung des bereits aufbereiteten Gemischs kommt. Unmittelbar danach bildet sich eine stehende, turbulente, abgehobene Diffusionsflamme um jeden Kraftstoffstrahl und die quasi-stationäre Phase, auch die diffusionskontrollierte Verbrennung genannt, beginnt. Nach wie vor wird der eingespritzte Kraftstoff von der Luft erhitzt und verdampft. Die beigemischte Luftmenge reicht für ein stöchiometrisches Luft-Kraftstoff-Verhältnis nicht aus und so entsteht eine fette, vorgemischte Reaktionszone stromabwärts des flüssigen Strahls. Hier entstehen unvollständige Verbrennungsprodukte und Rußvorläufer, die im inneren des Strahls nicht vollständig oxidiert werden können. Die Temperaturen nach der vorgemischten Reaktion betragen etwa 1600 K, was in Kombination mit dem vorherrschenden Luftmangel optimale Randbedingungen für die Rußbildung darstellt. Diese unvollständigen Verbrennungsprodukte werden in der nahezu stöchiometrischen Diffusionsflamme weitestgehend verbrannt. Bei den

hohen Temperaturen werden Stickoxide in der Diffusionsflamme und in den heißen verbrannten Gasen gebildet.

In Kapitel 3 wird zuerst der im Rahmen dieser Arbeit entwickelte optisch zugängliche Dieselmotor kurz beschrieben, so wie der Motorprüfstand. Danach werden die zum Einsatz kommenden Messtechniken beschrieben, so wie deren Umsetzung im Prüfstand. Als erstes wird elastische Lichtstreuung nach der Mie-Theorie erläutert. Simulationsergebnisse werden herangezogen, um dieses komplexe Phänomen zu veranschaulichen. Auf die laserinduzierten Inkandeszenz (LII) wird eingegangen, da diese ein Bestandteil der RAYLIX-Messtechnik ist. In dieser Arbeit kommt die RAYLIX-Technik, die aus planarer Rayleigh-Streuung, planarer LII und Extinktion besteht, zum ersten Mal im Brennraum eines Dieselmotors zum Einsatz. Eine Kombination aus neu entwickelter Hardware und Software wird erläutert, die für die Untersuchungen mit der Zwei-Farben-Methode verwendet werden. Es handelt sich um eine Bildteiler-Optik und eine umfangreiche Reihe an Softwaretools, die eine räumlich aufgelöste Bestimmung von Flammentemperaturen und KL-Werten ermöglicht. Abschließend wird eine Technik zur Abbildung von OH-Chemilumineszenz vorgestellt, wobei ein neuer Lösungsansatz in Form eines lichtstarken optischen Zugangs zum Einsatz kommt.

Kapitel 4 befasst sich mit der Bewertung der entwickelten Messtechniken und den Ergebnissen, die am Prüfstand gemessen wurden. Zwei Betriebspunkte werden dargestellt, die als Basis für verschiedene Parametervariationen dienen: ein Betriebspunkt mit geringer Last, der für die RAYLIX-Untersuchungen verwendet wurde und ein Betriebspunkt bei Teillast, der Untersuchungen der quasi-stationären Phase der Verbrennung ermöglicht. Speziell bei der Analyse des Teillast-Betriebspunkts erweist sich die Zwei Farben Methode als gut geeignet, räumlich und zeitlich aufgelöste Informationen über den Verbrennungsablauf zu erschließen, vor allem in der späten Phase der Verbrennung. Die Auswirkungen der Voreinspritzung auf die Entflammung und Verbrennung der Haupteinspritzung werden unter anderem mit der OH-Chemilumineszenz-Diagnostik dargestellt und erklärt. Der Betrieb mit einer Makroemulsion aus Dieselkraftstoff, Ethanol und Wasser (E10W10) wurde im Rahmen dieser Arbeit untersucht, insbesondere mithilfe der RAYLIX-Messtechnik. Durch den Einsatz von dieser und anderen optischen Methoden werden Einblicke in die Änderungen der Teilprozesse gegeben. Die drastische Reduktion der Rußemissionen wird anhand der Messergebnisse erklärt. Eine Zusammenfassung und ein kurzer Ausblick in Kapitel 5 runden die Arbeit ab.

Table of Contents

1. Introduction and Motivation 1

2. Diesel Combustion, Pollutant Formation and its Application 3

2.1. Diesel Combustion 3

2.2. Pollutant Formation 9

2.2.1. Unburned Hydrocarbons and Carbon Monoxide 11

2.2.2. Soot 11

2.2.3. NO_x 16

2.3. State of the Art for Heavy Duty Diesel Engines 17

3. Experimental Setup and Measurement Techniques 21

3.1. Optically Accessible Engine 21

3.2. Test Bench 24

3.3. Optical Measurement Techniques 25

3.3.1. Elastic Scattering 25

3.3.2. Laser-Induced Incandescence 29

3.3.3. RAYLIX 31

3.3.4. Two Color Method 36

3.3.5. OH Chemiluminescence Visualization 47

3.3.6. Summary of Measurement Techniques 50

4. Results and Discussion 51

4.1. Operating Points 51

4.1.1. Low Load 51

4.1.2. Part Load 52

4.2. Characterization of the Part Load Operating Point 53

4.2.1. Cylinder pressure trace 53

4.2.2. Mie scattering 53

4.2.3. OH Chemiluminescence 55

4.2.4. Two Color Method 58

4.3. Rail Pressure Variation 67

4.3.1. Mie Scattering 68

4.3.2. OH Chemiluminescence 69

4.3.3. Natural Soot Luminosity 70

4.4. Effects of the Pilot Injection 72

4.4.1. OH Chemiluminescence 73

4.4.2. Two Color Method 77

4.5. Comparison of E10W10 and Diesel 79

4.5.1. Mie Scattering 82

4.5.2. OH Chemiluminescence 83

4.5.3. RAYLIX 84

4.5.4. Two Color Method 89

5. Summary and Outlook 93

Table of Figures

Figure 2-1: Simulated flow field; swirl plane 7 mm below the cylinder head, 10 ° CA BTDC, 1000 rpm, motored, naturally aspirated operation 4
Figure 2-2: Schematic of a Diesel injection jet (adapted from [] and [11]). 5
Figure 2-3: λ-T diagram; region of > 1% soot concentration calculated for n-heptane with a residence time of 2 ms (data taken from []); NOx estimated from [] 6
Figure 2-4: Simplified conceptual model of the quasi-steady phase of Diesel combustion according to Dec (adapted from [23]). The upper labels describe the physical pheonomena and the lower labels describe some of the measurement techniques used to determine the nature of these phenomena.... 8
Figure 2-5: 2008 emissions of PM2.5 and PM10 in the United States (data from [46]) 10
Figure 2-6: HACARC reaction mechanism 13
Figure 2-7: Particle growth with the HACARC mechanism 14
Figure 2-8: NO_x and PM regulations for heavy duty Diesel engines since 1990 [] 18
Figure 2-9: Example of an exhaust aftertreatment system to meet Euro VI regulations (taken from [85]) 19
Figure 3-1: Cross sectional view of the optically accessible engine 21
Figure 3-2: Combustion chamber with endoscopic access, slotted piston and laser sheet 23
Figure 3-3: Piston designs. Left: observation cutout and slot for laser sheet; right: modified observation cutout and no laser sheet slot 23
Figure 3-4: Elastic scattering 25
Figure 3-5: Vertically polarized component of scattering intensity for four different particle diameters; logarithmic scaling. 26
Figure 3-6: Polarization ratio for scattering in air at a scattering angle of 90°; wavelength of incident light: 532 nm 28
Figure 3-7: Ratio of LII intensity to soot radiation at 2000 K; filter transmission curves for LII measurements . 30
Figure 3-8: Working principle of the image-splitting relay optics used for RAYLIX measurements 32
Figure 3-9: Laser and camera timing for RAYLIX measurements 32
Figure 3-10: Experimental setup for RAYLIX investigations 33
Figure 3-11: Blackbody spectral emissive powers as a function of wavelength with temperature as a parameter 37
Figure 3-12: Overview of data processing software for two color method measurements 39
Figure 3-13: Sketch of image-splitting optical relay used for two color method experiments 40
Figure 3-14: Simulated transmitted emissive powers for wavelengths of 550 and 750 nm 41
Figure 3-15: Definitions of solid angle, differential areas, and projected differential areas 42
Figure 3-16: Simulated deviations in measured temperatures for two different filter combinations. Left: FWHM = 10 nm; right: FWHM = 40 nm 44
Figure 3-17: Simulated deviations in measured KL values for three different filter combinations. Left: perfect filters; middle: FWHM = 10 nm; right: FWHM = 40 nm 44
Figure 3-18: Effect of distance between flame and endoscope on the calculated flame temperature 45
Figure 3-19: Assumed and actual window transmission (qualitative) as they are affected by fouling 46
Figure 3-20: Depiction of optical system used for OH chemiluminescence imaging 47
Figure 3-21: CAD cross section of the optical access used for OH chemiluminescence imaging 48
Figure 3-22: Optical setup used for OH chemiluminescence imaging 49
Figure 3-23: Filter transmission curves used for OH chemiluminescence imaging 49
Figure 4-1: Averaged, filtered cylinder pressure trace for the mid load operating point. Gray solid line: fired pressure trace; black dotted line: calculated motored pressure trace. 53

Figure 4-2: Example of Mie scattering image and identification of fuel jets. Standard part load operating point, 4 ° CA $ASOI_I$. 54
Figure 4-3: Penetration depths for the part load operating point; the start of combustion is indicated by a gray beam 55
Figure 4-4: OH chemiluminescence image; average of 20 cycles, 10 µs exposure duration; imaged crank angle 6 ° CA $ASOI_I$ 56
Figure 4-5: Limiting angles for logarithmic intensity profiles 56
Figure 4-6: Logarithmic radial intensity profiles for a crank angle of 6 ° $ASOI_I$ 56
Figure 4-7: Averaged logarithmic radial intensity profiles for the part load operating point at various crank angles 57
Figure 4-8: Example of a data-averaged flame temperature image, calculated from an ensemble average of 20 working cycles; image at 7.9 °CA ATDC, 10.9 ° CA $ASOI_I$ 59
Figure 4-9: Series of data-averaged (over 20 working cycles) temperature (left column) and KL (right column) images for the part load operating point 60
Figure 4-10: Three regions of interest for analysis of the two color pyrometry images. 61
Figure 4-11: Data averaged mean temperature profiles for three regions of interest 61
Figure 4-12: Control volume for a portion of a fuel jet with entrainment air 62
Figure 4-13: Data averaged (over 20 working cycles) mean KL profiles for three regions of interest 63
Figure 4-14: Mean temperature and KL profiles in the downstream and upstream regions for two individual working cycles (thin lines); data-averaged (over 20 working cycles) mean temperature and KL profiles in the upstream and downstream regions (thick lines) 64
Figure 4-15: Mean data-averaged temperature profiles in the downstream region for two different measurement series. Reference measurement points at the beginning: thick gray lines; reference measurement points with fouled windows: thin gray lines (without correction); dashed black lines (with correction). 66
Figure 4-16: Normalized engine-out indicated specific soot emissions for rail pressures of 1600, 1800, and 2000 bar 67
Figure 4-17: Liquid penetration depths for rail pressures of 1600 (thin black line), 1800 (light gray line), and 2000 (thick dark gray line) bar; the start of the main combustion is indicated with a gray beam ... 68
Figure 4-18: Averaged logarithmic radial intensity profiles for the part load operating point at 8 ° CA $ASOI_I$ ... 70
Figure 4-19: Mean, data-averaged soot luminosities (measured through the 700 nm bandpass filter) for the upstream (top) and downstream (bottom) regions of interest with rail pressure as a parameter 71
Figure 4-20: Averaged, filtered cylinder pressure traces for the part load operating points with (thick gray line) and without (thin black line) a pilot injection 72
Figure 4-21: Average OH chemiluminescence intensity profiles as a function of crank angle after the start of the main injection for the part load operating point with and without a pilot injection 73
Figure 4-22: OH chemiluminescence images for the part load operating point with a pilot injection; the bottom row of images is comprised of ensemble averages of the five individual cycle images 74
Figure 4-23: OH chemiluminescence images for the part load operating point without a pilot injection; the bottom row of images is comprised of ensemble averages of the five individual cycle images 75
Figure 4-24: Averaged logarithmic radial intensity profiles for the part load operating point with (gray curves) and without (black curves) a pilot injection for a range of crank angles 76
Figure 4-25: Mean, data averaged (over 20 working cycles) temperature and KL profiles in the downstream and upstream regions for the part load operating point with a pilot injection (gray lines) and without a

pilot injection (black lines); data are plotted against degrees crank angle after the indicated start of the main injection; median downstream KL profiles are shown as dotted lines for the sake of comparison with the mean 77
Figure 4-26: Cylinder pressure traces for the low load operating point with Diesel fuel and E10W10; traces with 30% EGR are displayed as dashed lines 80
Figure 4-27: Normalized engine-out indicated specific soot emissions for Diesel fuel (gray) and E10W10 (black) with 0%, 15%, and 30% EGR 81
Figure 4-28: Cylinder pressure traces for the part load operating point with Diesel fuel and E10W10; the indicated start of the main injection is shown with a dotted line at 3 ° CA BTDC 82
Figure 4-29: Composite thresholded images for Diesel fuel and E10W10, 1.1 ° CA $ASOI_I$; gray indicates the presence of an E10W10 scattering signal and the absence of a Diesel scattering signal; black indicates scattering with Diesel but not with E10W10 83
Figure 4-30: Averaged logarithmic radial intensity profiles for the part load operating point with Diesel fuel (gray curves) and with E10W10 (black curves) 84
Figure 4-31: Single-shot raw Rayleigh and LII images (from the same measurement) with a non-linear, false color representation; imaged at 6.8 ° CA $ASOI_I$ 85
Figure 4-32: Individual cycle images of mean particle diameter for a crank angle of 6.9 ° CA $ASOI_I$; comparison between Diesel fuel and E10W10 for EGR rates of 0, 15, and 30% 86
Figure 4-33: Individual cycle images of particle volume fraction for a crank angle of 6.9 ° CA ASOII; comparison between Diesel fuel and E10W10 for EGR rates of 0, 15, and 30% 87
Figure 4-34: Soot volume in the measurement volume as a function of crank angle for Diesel fuel (gray lines) and E10W10 (black lines) for different EGR rates: 0% EGR (solid lines), 15% EGR (dashed lines), and 30% EGR (dotted lines) 88
Figure 4-35: Maximum data-averaged soot luminosities (measured through the 700 nm bandpass filter) for Diesel fuel (gray) and E10W10 (black) as functions of crank angle for the part load operating point. 89
Figure 4-36: Mean, data averaged (over 20 working cycles) temperature and KL profiles in the downstream and upstream regions for the part load operating point with Diesel fuel (gray lines) and E10W10 (black lines) 90
Figure 4-37: Adiabatic flame temperatures for n-heptane and an E10W10 mixture with n-heptane as a function of λ 91

Nomenclature

Abbreviation	Description
° CA	Degrees crank angle
3D-CFD	Three dimensional computational fluid dynamics
AFR_s	Stoichiometric air / fuel ratio
ASC	Ammonia slip catalyst
$ASOI_I$	After the indicated start of injection (start of injection control signal)
ATDC	After top dead center
BTDC	Before top dead center
CAD	Computer-aided design
CCD	Charge coupled device
CMOS	Complementary metal oxide semiconductor
CNC	Computerized numerical control
CRC	Collaborative Research Centre
DOC	Diesel oxidation catalyst
DPF	Diesel particulate filter
E10W10	Macroemulsion of 80 vol% Diesel fuel, 10 vol%ethanol, and 10 vol% water
EGR	Exhaust gas recirculation
FWHM	Full width at half maximum
GDP	Gross domestic product
HACARC	Hydrogen-abstraction-carbon-addition-ring-closure
HCCI	Homogeneous charge compression ignition
ICCD	Intensified CCD
LES	Large eddy simulation
LHV	Lower heating value
LII	Laser induced incandescence
PAH	Polycyclic aromatic hydrocarbons
PEEK	Polyether ether ketone
PIV	Particle image velocimetry
PLIF	Planar laser induced fluorescence
PM	Particulate matter
$PM_{2.5}$	Particulate matter with a median aerodynamic diameter less than 2.5 µm
PM_{10}	Particulate matter with a median aerodynamic diameter less than 10 µm
RAYLIX	Combination of planar Rayleigh scattering, planar LII, and total extinction
RTV	Room temperature vulcanizing
SCR	Selective catalytic reduction
SOI_I	Indicated start of injection (start of injection control signal)
TDC	Top dead center
TEM	Transmission electron microscope / microscopy
UV	Ultraviolet
VGT	Variable geometry turbine

Physical Quantities

Symbol	Units	Description
a_j, b_j	-	Complex coefficients for scattering amplitude functions
c_o	m/s	Speed of light in a vacuum
c_p	kJ / (kg K)	Specific heat at constant pressure
C_D	-	Discharge coefficient
$C_{HH/VV}$	m^2	Horizontal / vertical differential scattering cross sections
C_1	W μm^4 / m^2	First radiation constant
C_2	μm K	Second radiation constant
C_{sca}	m^2	Scattering cross section
d	mm, μm, nm	Diameter
$dA_{det/flame/lamp}$	m^2	Differential area of detector / flame / calibration lamp
$dA_{i/j}$	m^2	Differential area of surface i / j
$E_{\lambda,b}$	W / (m^2 μm)	Blackbody spectral emissive power
E_λ	W / (m^2 μm)	Gray body spectral emissive power
E_p, E_v	N/C	Parallel and perpendicular components of an electric field
f_{cal}	W/$m^2\mu$m sr counts	Calibration factor for two color pyrometry measurements
f_V	m^{-3}	Volume fraction
h	m^2 kg/s	Planck's constant
H	counts	Intensity of a CCD or CMOS pixel
I_λ	W/m^2 μm sr	Spectral intensity
$I_{HH/VV}$	W/m^2	Horizontally / vertically polarized scattering intensity
I, I_0	W/m^2	Intensity of incident light
$IMEP_n$	MPa	Net indicated mean effective pressure
K_b	J/K	Stefan-Boltzmann constant
K, K_{ext}, K_{sca}	m^{-1}	Absorption, extinction, and scattering coefficient
L	m	Optical pathlength through a flame
m	-	Complex index of refraction
m_p	kg	Particle mass
$\dot{m}$	kg/s	Mass flow rate
n	-	Real index of refraction
N_V	m^{-3}	Particle number density
p	Pa, bar, MPa	Pressure
p(r)	-	Particle size distribution
$\dot{q}$	W	Power, rate of energy transfer
$\dot{Q}_\lambda$	W/nm	Spectral emissive power
Q_{sca}	-	Scattering efficiency
r	m	Radius or radial distance
s	m	Distance between scatterer and observer
S_{1-4}	-	Mie scattering amplitude functions
T	K	Temperature
T_a	K	Apparent, brightness, or blackbody temperature
v_f	m/s	Magnitude of the fuel velocity
x	m	Axial distance

Symbol	Units	Description
α	-, rad	Two color method empirical constant, jet spreading angle
α_{LII}	m^{-3} $counts^{-1}$	Calibration factor for LII signal
ε_{λ}	-	Monochromatic emissivity
$\varepsilon_{i,j}$	rad	Radiometric angles
θ	rad	Scattering angle
λ	nm, -	Wavelength, air-fuel equivalence ratio
π_j	-	Function used to calculate scattering amplitude
ρ	kg/m^3	Density
σ	-	Standard deviation of a particle distribution
τ_j	-	Function used to calculate scattering amplitude
φ	rad	Polarization angle of incident light
Ω	sr	Solid angle between emitter and detector

1. Introduction and Motivation

Direct injection Diesel engines, because of their high efficiencies, are the power plant of choice for a wide variety of both mobile and stationary applications. Their high compression ratios, unthrottled and often turbocharged operation, and globally lean mixtures contribute to their high thermodynamic efficiency. The unsurpassed convenience and energy density of liquid hydrocarbons is unlikely to ever be achieved by that of even the most advanced lithium ion batteries [1]. These inherent advantages will ensure that Diesel engines will remain indispensable for many applications for the foreseeable future. For example, freight traffic in Europe, which is largely dependent on transport by sea and via trucks [2], is projected to continue to increase until at least 2030 [3]. Freight transport in particular has been tradionally and remains closely tied to gross domestic product (GDP), so GDP growth is accompanied by growth in freight traffic [4]. These modes of transportation rely heavily on Diesel engines, so the Diesel's disadvantages in terms of pollutant emissions will continue to be both a source of societal concern and a topic of substantial research activities.

New technologies have enabled and will continue to enable improvements in the Diesel combustion process. Engine-out emission levels remain unacceptably high for significant portions of the engine operating map, so that sophisticated exhaust aftertreatment systems are typically necessary in order for engines to meet the legislated regulations. Because these systems increase costs and complexity, create packaging problems, and negatively affect fuel economy, the goal of Diesel combustion development is to reduce and/or eliminate the necessity for aftertreatment systems while maintaining the high efficiency of the Diesel engine. It remains uncertain if such a goal is attainable for the entire engine operating map and for dynamic engine operation. As such, research continues at all levels to better understand and control the underlying processes responsible for combustion and pollutant formation.

Significant improvements in computing have made advanced simulation techniques in complex combustion devices such as Diesel engines possible. One such approach is to simulate the flow inside the cylinder using large eddy simulations (LES) and to couple LES with reaction mechanisms and pollutant formation models. The successful application of such simulation techniques in practical combustion devices such as Diesel engines provides great insight into the underlying processes and pollutant formation mechanisms. Validation of these models is ideally achieved with optically-obtained measurement data, although this process is often not straightforward, depending on which simulation data and which experimental data are being compared.

Research activities within the Collaborative Research Centre (CRC) 606 have been devoted to the investigation of many aspects of non-stationary combustion over three funding periods spanning 12 years [5]. Within the CRC 606, three subprojects are directly related to this work. The first subproject involves the implementation of LES in the combustion chambers of gasoline direct injection and Diesel engines. The second involves the integration of an advanced, integral combustion model into an existing computational fluid dynamics code for the purpose of performing simulations of all types of engine combustion systems (e.g. gasoline direct injection, homogeneneous charge compression ignition, and Diesel). The work performed on the third subproject in its final funding period is the subject of this dissertation.

The goal of this subproject was to extend previous experimental investigations of Diesel combustion to provide more understanding of the following processes:

- Gas exchange processes and in-cylinder flow

- Fuel injection and mixture formation
- Combustion and soot formation
- Soot oxidation and emission behavior

Furthermore, these investigations were to be performed in one and the same optical research engine, the design of which was completed during the previous funding period. To achieve the stated goals, the following measurement techniques were to be adapted to and applied in the combustion chamber of the new engine:

- Particle image velocimetry (PIV)
- Mie scattering
- RAYLIX
- OH chemiluminescence imaging
- Two color pyrometric imaging

As a first step, the design of the engine is revised and finalized. The production parts are modified where possible, and new parts are built to enable optical accessiblity. After the engine is built, tested, and successfully put into operation, the focus shifts towards the development and application of the aforementioned measurement techniques in the combustion chamber. The intention of the PIV measurements is to gain an understanding of the bulk flow within the combustion chamber. Mie scattering images provide insight about the liquid phase fuel penetration into the cylinder, and thus of the spray vaporization behavior. The RAYLIX technique is a combination of planar Rayleigh scattering, planar laser induced incandescence, and total extinction. It provides two dimensional images showing mean particle diameters, particle volume fractions, and particle number densities in the planar observation volume. OH chemiluminescence imaging identifies locations in the combustion chamber in which high temperature, near-stoichiometric combustion takes place. As such, the information produced with this imaging technique gives insight into the air entrainment and thus mixture formation processes within the jet, as well as into the inflammation phase of combustion. The two color method is to be adapted to provide temperature and soot KL value information with not only a high temporal resolution, but also with a high spatial resolution. The imaging technique that is developed represents a substantial improvement in spatial resolution over the methods previously employed in this subproject, which involve a comparatively simple fiber optic probe and spatially integrated measurements with photomultipliers.

The data acquired with these measurement techniques provide deep insight into several aspects of the Diesel combustion process, and will serve to validate the LES and combustion models that are being developed as part of the other subprojects. The focus of this dissertation is on the former. It is divided into five chapters, the first of which is the introduction and motivation. The second chapter discusses the current state of knowledge of Diesel combustion and pollutant formation (in particular soot formation). The topic of chapter three is the experimental engine, the theory behind the measurement techniques, and their implementation in the test bench. In chapter four, experimental results are presented for a variety of investigations. Where applicable, the individual measurement techniques are evaluated and suggestions for future development are made. The analysis of the experimental data demonstrate the abilities of these techniques to provide detailed information about the underlying processes responsible for soot formation in the combustion chamber. The fifth and final chapter is a summary of the work and a short outlook.

2. Diesel Combustion, Pollutant Formation and its Application

In the first section of this chapter, the impacts of pollutants produced by Diesel engines on human health are briefly discussed. The mechanisms by which carbon dioxide and unburned hydrocarbons form are then described. A substantial amount of attention is given to the soot formation process, as it is extremely complex and the dependence of the process on the fuel and on the local thermochemical environment is important when considering the experimental results produced in this work. Formation mechanisms for oxides of nitrogen are summarized; here, the thermal mechanism is of primary importance. Regions of the combustion chamber with high temperatures and excess oxygen are conducive to the formation of oxides of nitrogen (NO_x), and locally rich conditions lead to soot formation. Measures to decrease NO_x emissions generally decrease combustion temperatures and therewith the desirable oxidation of soot, and increased soot oxidation as a result of higher combustion temperatures leads to higher NO_x emissions. This behavior is known as the soot-NO_x tradeoff and remains a fundamental development issue for Diesel combustion systems. Traditionally, the most significant emissions of Diesel engines are soot and NO_x, but unburned hydrocarbons and carbon monoxide have become an issue with the introduction of low temperature combustion strategies.

The second section is devoted to the description of the current understanding of combustion in a heavy duty, direct injection Diesel engine. This discussion begins with an overview of the in-cylinder environment, and then describes the combustion event, starting with the injection of liquid fuel and continuing with the mixture formation process, ignition processes, and the development of a quasi-steady, lifted turbulent flame jet. Particular emphasis is placed on the means in which soot has been observed to escape the combustion chamber before being oxidized.

The third and final section of this chapter is devoted to heavy duty Diesel engine emission regulations and the newest generation of engines that have successfully been designed to meet these regulations. Problems associated with exhaust aftertreatment systems are described, as is the current the state of Diesel combustion system research.

2.1. Diesel Combustion

The combustion process in a modern heavy duty Diesel engine with direct injection is extremely complex. Liquid fuel is injected at high pressures into a hot, dense environment near top dead center. The liquid fuel must be atomized, vaporized, and mixed with the hot air, whereby the fuel is heated to its autoignition temperature. The fuel that is injected during this ignition delay reacts rapidly, and soon a lifted turbulent flame forms around each fuel spray. The fuel that continues to be injected and heated by mixing with air reacts just upstream of the tip of the liquid spray, but sufficient mixing has not occurred to enable complete combustion of the fuel-air mixture. The products of this rich premixed reaction propagate downstream into the oxygen-poor center of the combustion plume. Here, the thermochemical environment is well-suited for soot formation and growth. These products of the rich combustion are consumed in a thin flame front that forms at the periphery of the plume, where mixing with oxygen from the unburned gas creates a near-stoichiometric flame front. The high temperatures in this flame front are effective at oxidizing soot but also lead to the production of NO_x. The combustion products are mixed with the cooler, unburned gas, which can potentially freeze pollutant concentrations at levels above their equilibrium values. Soot is

deposited on combustion chamber walls and some of this likely appears later in the exhaust after it desorbs during the blowdown process. During the combustion, the piston moves down in its working stroke and the temperatures and pressures inside the cylinder decrease as work is extracted from the gas. This reduces the likelihood of the last pockets of soot being oxidized and thus contributes to engine-out soot emissions. This entire process is completed within a few tens of milliseconds, after which the exhaust gas is expelled and replaced with air and residual gas, and the process repeats. In this section, these subprocesses are described based on information available in the literature. Emphasis is placed on pollutant formation, particularly soot formation.

As the air and residual gas are compressed during the compression stroke, the temperature and density of the gas also increase. At the time of injection near top dead center, the temperatures are typically on the order of 1000 K and the density is between 15 and 25 kg/m^3 [51]. For the standard, part load operating point studied in this work, the temperature calculated with a polytropic compression (coefficient 1.36) is estimated to be approximately 830 K. The corresponding density in the cylinder is then approximately 23 kg/m^3. The use of a pilot injection increases temperatures and pressures, as well as densities, to some extent. Typical flow conditions within heavy duty engines are quiescent, and in the engine used in this work a slight swirl flow is present. The in-cylinder flow has been simulated with a 3D, RANS-based CFD simulation [6]; an example of the swirl flow is shown in Figure 2-1. PIV measurements taken inside the engine in motored operation show that in the tumble plane, measured velocities near the end of compression are typically less than 10 m/s, and the flow field appears qualitatively different in every working cycle [7]. In this environment, it is expected that the turbulent kinetic energy of the injected fuel is more substantial than the kinetic energy of the gases in the cylinder, that is until the injection event is finished [8].

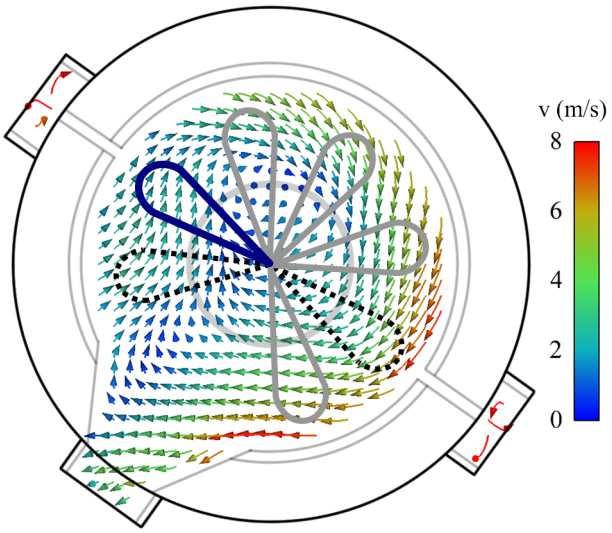

Figure 2-1: Simulated flow field; swirl plane 7 mm below the cylinder head, 10 ° CA BTDC, 1000 rpm, motored, naturally aspirated operation

Because the pressure in a common-rail system is high even at the beginning of injection, cavitation likely occurs in the needle seat and in the injector orifices as soon as fuel begins to flow, which has significant implications for the spray break-up [9]. Turbulence within the orifice also plays an important role in spray break up. Shown schematically in Figure 2-2 is a single injection jet as it propagates outwards from the injector tip. The discussion here focuses on one injection jet, but is generally applicable to all jets in a heavy duty engine.

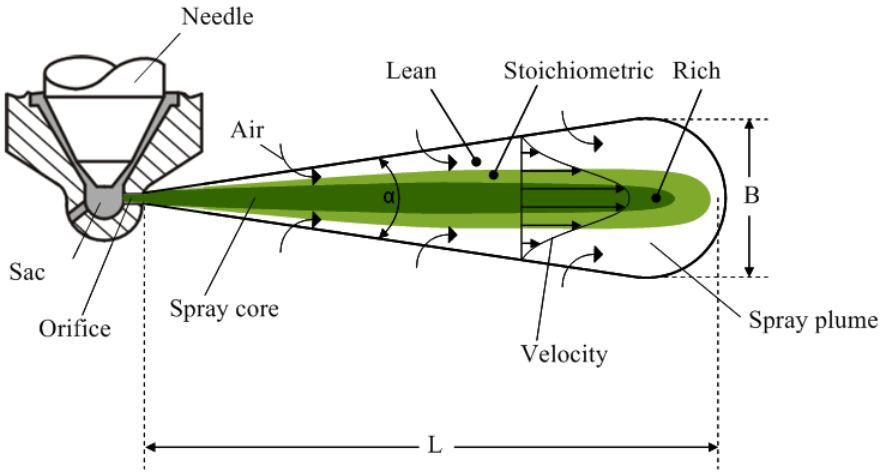

Figure 2-2: Schematic of a Diesel injection jet (adapted from [10] and [11]).

The cavitation and turbulence within the nozzle helps the primary break-up of a liquid stream into ligaments and larger droplets directly downstream of the orifice. For a detailed description of the current understanding of these effects, the reader is referred to [11]. Since the measurement techniques in this work cannot spatially resolve these effects and the injector geometry is held constant, this topic is not discussed in detail here. Aerodynamic forces between the air around the jet and the liquid fuel break up the ligaments and larger droplets into smaller droplets and pull air into the jet. The behavior of these smaller droplets are defined by the deceleration due to aerodynamic drag, convective heat transfer from the entrained air, and mass transfer of vaporized fuel away from the droplet [51]. The aerodynamic drag is strongest for the frontmost droplets in the jet; they are slowed and pushed out of the way by the faster moving droplets in the core, which causes the jet to spread radially outward from the jet axis [9]. The velocity profile of the droplets in the jet is shown in Figure 2-2. The largest, fastest moving droplets are found in the core of the spray. As they are broken up, they are slowed down by aerodynamic forces, so the velocities decrease with increasing distance from the jet axis. As the smaller droplets begin to vaporize, a mixture of fuel and air develops and surrounds the jet. The energy required to vaporize the fuel (the fuel's heat of vaporization) is taken from the air's sensible enthalpy, so temperatures decrease where fuel is being vaporized. The competing thermal effects of heating through mixing with air and cooling through vaporization of fuel influence the local ignition chemistry. After a certain development phase, the penetration depth of the liquid core remains stable. Espey and Dec determined that the stable penetration depth of a Diesel fuel jet is strongly dependent on the temperature and the density of the air in the cylinder. For conditions typical for Diesel combustion, they measured liquid penetration depths of between 13 and 30 mm,. Furthermore, they cite research showing that larger injector hole diameters lead to longer penetration depths [12]. This is in agreement with the results of Wiartalla, considering the relatively large orifice sizes employed in his work [13], and it was also confirmed by Siebers in [14]. Siebers also determined that the liquid penetration depth is not significantly affected by rail pressure, and the lower volatility components of a multicomponent fuel determine the length of the liquid fuel core. In general, shorter penetration depths mean more effective air entrainment and vaporization of the fuel and therefore a faster mixing process. In a small-bore passenger car Diesel engine, the penetration of the liquid fuel may reach the piston bowl wall, which has significant implications for the ensuing combustion and pollutant formation. These effects will not be discussed here, so the interested reader is referred to [52, 15].

The progress of a packet of fuel as it is injected into the combustion chamber, vaporized and mixed, and then burned, can be effectively visualized on a λ-T diagram, where λ is the air-fuel equivalence ratio and T is the temperature. Such a diagram is shown in Figure 2-3. At the top is a region in which soot formation occurs for n-heptane with a residence time of 2 ms such that concentrations are greater than 1%. The region at the bottom right has been calculated with the Zeldovich mechanism, also for a residence time of 2 ms. The solid line represents the adiabatic flame temperature of n-heptane with a starting temperature and pressure of 722 K and a starting pressure of 62.9 bar, respectively. These represent the conditions near TDC for the mid load point measured in these investigations. The flame temperatures have been calculated with the STANJAN equilibrium code [16] for n-heptane and an emulsion of n-heptane, 10 vol% water, and 10 vol% ethanol, as a function of λ. It should be noted that temperatures in rich zones ($\lambda \approx 0.5$) can momentarily exceed these computed temperatures before equilibrium is achieved [18].

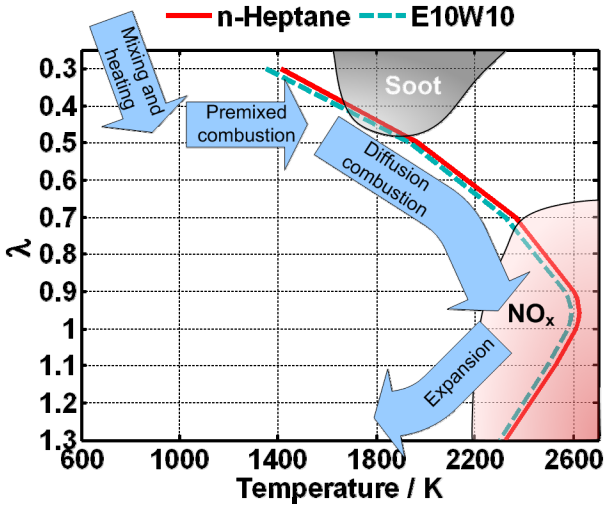

Figure 2-3: λ-T diagram; region of > 1% soot concentration calculated for n-heptane with a residence time of 2 ms (data taken from [17]); NOx estimated from [18] .

The mixing process is represented on this diagram with the arrow at the top left that is labeled "Mixing and Heating". This means that mixing is represented by movement towards higher λ values, and heating by movement towards higher temperatures.

Chemiluminescence resulting from the first fuel decomposition reactions is first observed to occur in the sheath of fuel-air mixture around and in the downstream portion of the spray plume and move downstream as time progresses [19]. The authors attributed this chemiluminescence signal primarily to formaldehyde (CH_2O) and CH, but to a lesser extent to HCO, that form during these first reactions. However, chemiluminescence is first observed before significant heat release can be measured. Chemiluminescence from the OH radical was not detected early during the ignition delay period, so it is asserted that these first observable species are typical of those formed in cool flames [19, 20]. Investigations with Rayleigh scattering suggest that air-fuel equivalence ratios in the gas mixture downstream of the liquid jet shown in Figure 2-2 are between 0.25 and 0.5 at the time of ignition, so the initial ignition takes place in rich mixtures [21]. The heat released by these cool flames increases temperatures until the high-temperature mechanism takes over [22]. Soon after the appearance of the chemiluminescence signal and simultaneous with the start of significant heat release, PAHs have been measured in the portion of the spray downstream of the liquid core [23]. They are not found only at the edges of the plume, rather they are distributed volumetrically throughout the jet. Soot luminescence can be measured shortly after the PAHs

are first observed in the downstream portion of the spray plume, and these luminous emissions quickly overwhelm the chemiluminescence signals. The locations at which soot is observed vary from cycle to cycle [24]. Soot was also measured shortly after ignition just downstream of the liquid jet in the constant volume chamber used in [13].

The products of the rich premixed reactions are small hydrocarbon fragments, for example C_2H_2, C_2H_4, and C_3H_3, as well as larger fuel fragments, CO, and H_2O. The temperature of the products is typically on the order of 1600 K – 1700 K [25]. This is also illustrated in Figure 2-3 by the arrow labeled "Premixed Combustion." This combination of temperatures and chemical species is well-suited for soot formation, and because the oxygen that had been entrained to this point has been consumed in this premixed reaction, there is little to no fresh oxygen available in the spray plume to promote further oxidation of hydrocarbons. As the first, premixed stage of the combustion ends, a lifted, turbulent diffusion flame forms around the spray plume. In the flame front, air from outside the plume diffuses towards the plume and oxidizes the hydrocarbons, soot, and CO. The injection continues, as do the processes of spray break-up, mixing, and vaporization. The rich premixed reaction zone remains downstream of the liquid jet and continues to provide its combustion products to the downstream portion of the flame, where PAH and soot are formed and later oxidized in the turbulent front. High concentrations of soot are observed to form at the front of the head of the plume, and as the combustion progresses the particles in the head are observed to increase in size and to envelop more of the head of the jet [23]. The extinction measurements of Wiartalla also show the highest soot concentrations in the head of the plume for an injection amount of 14 mm^3 at 2.49 ms after the start of injection, but it seems that this flame jet develops differently in the absence of external influence by a piston bowl [13].

Combustion in the flame front is nearly stoichiometric, so combustion temperatures are high; this is shown in Figure 2-3 with the arrow labeled "Diffusion combustion". Under these conditions, concentrations of OH radicals are observed to be very high in the thin turbulent flame front, even higher than their equilibrium values. On the fuel side of the front, OH concentrations are low because OH reacts very readily with the hydrocarbon fragments and soot. Concentrations of OH decrease rapidly in the high-pressure post-flame gases, so the locations of highly concentrated OH radicals are taken to be a reliable marker of this flame front under Diesel conditions [26]. Techniques have also been developed that make use of OH chemiluminescence to determine the lift-off length of the turbulent flame [27,28]; these are discussed briefly in the next chapter. The lift-off length is defined in this case to be the distance between the injector orifice and the rapid increase in OH chemiluminescence signal. It is an indicator of the amount of air that is entrained into the fuel jet, and thus has been used to determine the effects of various operating parameters on the air entrainment process [28]. For example, Siebers and Higgins determined that increasing gas temperatures decreases the lift-off length and therefore the amount of air entrained up to the lift-off length. Increases in gas density decrease the lift-off length, but because the air entrained is more dense, the amount of air entrained up to the lift-off length is not significantly affected by changes in density. Smaller injector orifices lead to shorter lift-off lengths, but the enhanced air entrainment due to the smaller orifice size is the dominant factor, and so air entrainment is increased significantly for smaller orifices. Higher velocities due to increased injection pressures lead to longer lift-off lengths and thus improved air entrainment. Finally, Siebers and Higgins show that the amount of visible soot luminosity decreases substantially with the amount of air entrained. The effects of proximity to in-cylinder surfaces and of swirl flow on lift off length were studied by Musculus, but the results did not provide a complete understanding of these effects [29]. This is represented in Figure 2-3 by an enhanced mixing process, which brings air fuel ratios to higher values before the heat released by the

combustion increases the temperatures, thus avoiding conditions under which significant amounts of soot form.

Relative nitric oxide concentrations have been measured in the combustion chamber of a Diesel engine using PLIF; they are observed not as products of the rich premixed reaction, but on the lean side of the turbulent diffusion flame front [30]. A smaller amount of NO is also observed to form in the post-flame gases. This is in agreement with Figure 2-3; NO formation forms either with slightly lean combustion and with higher combustion temperatures. Musculus examined NO formation in a Diesel engine in greater detail [31]. Engine-out NO emissions depend on the combustion temperatures and residence times, which are affected by: combustion phasing and thus the duration that thermal NO is able to form in the hot post-flame gases before decreasing temperatures effectively freeze reactions involving NO; the amount of soot formed during the combustion and thus the extent of radiative heat loss experienced by the flame; compression heating of the post-flame burned gases; and mixing of the post-flame gases with cooler air.

The phenomena described above are summarized in Figure 2-4, which is based on Dec's conceptual combustion model [23]. The temporal relationships of these phenomena are not shown in the diagram, rather the spatial relationships are depicted. The combustion in any single working cycle is not believed to look like the jet structure shown in the figure. For instance, the turbulent diffusion flame front is highly corrugated and the soot particles are typically found in different regions of the cylinder for every working cycle. The regions depicted in the figure simply indicate the locations where these phenomena are observed to occur. Also summarized in the figure are some of the optical measurement techniques that were employed to enable the current understanding of Diesel combustion in a heavy duty Diesel engine with direct injection.

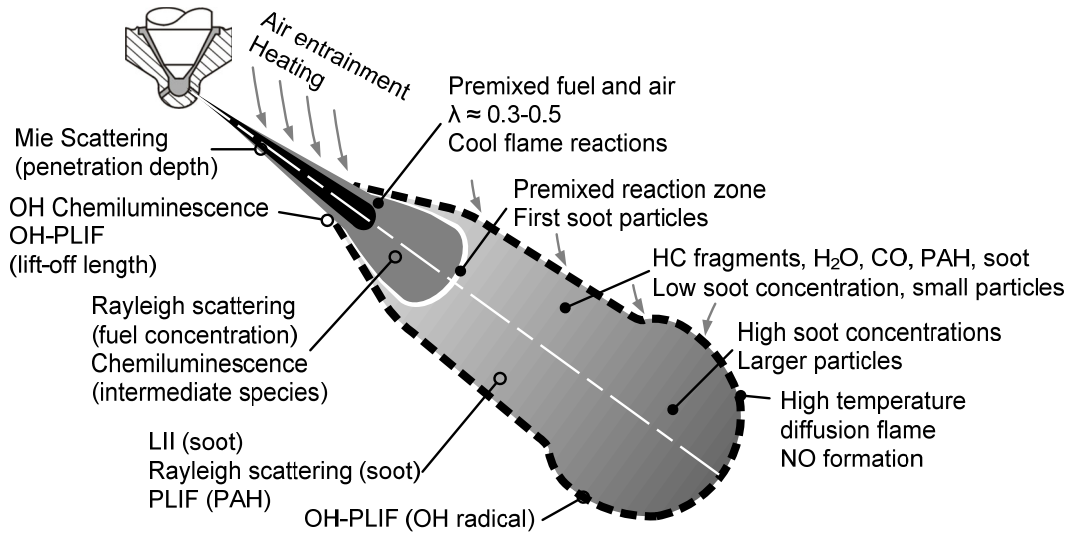

Figure 2-4: Simplified conceptual model of the quasi-steady phase of Diesel combustion according to Dec (adapted from [23]). The upper labels describe the physical pheonomena and the lower labels describe some of the measurement techniques used to determine the nature of these phenomena

As combustion progresses and the plume continues to grow, vortices around the outside of the head of the jet form and the region in which soot can be measured expands. The in-cylinder swirl flow deflects the downstream portion of the plume. For high swirl numbers (above 4), Spicher et al. showed that with a multihole injector, the individual spray plumes may be so deformed that they interact with each other, which has a significant impact on soot formation [32, 33, 34].

The possibility exists that the head of the Diesel jet interacts with the combustion chamber wall, i.e. the wall of the piston bowl. Soot may be deposited on the relatively cool surfaces. Suhre and Foster examined this phenomenon and concluded that soot is deposited on the wall primarily by thermophoresis (driven by thermal gradients) [35].

The balance of soot formation and soot oxidation within the combustion chamber determine how much soot is present in the exhaust gas. The current belief is that soot formed in the jet during Diesel combustion would be oxidized if it passed through the high temperature diffusion flame, but this flame may be extinguished during the expansion stroke and so this soot cannot be fully oxidized [65]. Dec and Tree did not observe soot outside of the turbulent flame front (marked by the presence of an OH-PLIF signal), but they did measure that after this flame front makes contact with the wall, it is eventually extinguished at the wall, thus providing a means for soot deposits to form [36]. However, in a follow-on study, Tree and Dec determined that the contribution of soot wall deposition is not the most significant source of engine-out soot emissions, so other mechanisms must be responsible for the soot found in the exhaust [37]. As suggested by Kent and Wagner, temperature plays a very important role in the oxidation process [38]. For a variety of laboratory flames, they determined that soot burnout ceases below approximately 1300 K. Dec and Kelly-Zion examined soot burnout with a combination of LII and OH-PLIF in more detail [39]. They determined that late during the last phase of combustion, diffusion flames (soot clouds surrounded by OH fluorescence) could still be identified long after the end of injection and the breakdown of the jet structure. Furthermore, they observe that these pockets of soot are not always able to be consumed before the exhaust valve opens. This can be caused by a lack of sufficient time for oxidation in a still-burning zone, either due to late combustion phasing or higher engine speeds, or by extinguishing of the oxidation reactions that exist around the soot pockets. The latter is closely linked with combustion and burned gas temperatures, and so it is strongly influenced by the use of diluents.

Developing modern Diesel combustion systems means optimizing many factors including soot and NO_x emissions, packaging, and costs. NO_x aftertreatment systems are expensive, require complex control strategies, and create packaging problems. Upon inspection of Figure 2-3, it becomes clear that both soot and NO_x emissions can be reduced through lean, low temperature combustion. Enhancements to the mixture formation process can provide such leaner mixtures, and lower temperatures are best achieved by decreasing oxygen concentrations, often through the use of EGR. In order to decrease pollutant emissions to the lowest possible level, these measures must to be optimized to the greatest extent possible without impacting fuel economy.

2.2. Pollutant Formation

As is the case with many practical combustion systems, the combustion process in a real Diesel engine is not complete, so combustion products other than CO_2 and H_2O are found in the exhaust gases. These include unburned hydrocarbons, carbon monoxide (CO), oxides of nitrogen (NO_x), and soot; Diesel engine exhaust has been classified as carcinogenic by the International Agency for Research on Cancer, which is part of the World Health Organization. In particular, Diesel exhaust has been identified as a cause of lung cancer [40]. The avoidance of soot and NO_x has shaped the development of Diesel combustion systems for decades.

CO and unburned hydrocarbons result from incomplete combustion of hydrocarbon fuels. CO is hazardous to human health; when it is inhaled, it bonds to hemoglobin, thus reducing the hemoglobin's ability to deliver oxygen to body tissues. In small doses, this can cause cardiovascular and neurobehavioral changes. In high doses or after prolonged exposure,

unconsciousness or death can result. CO is particularly dangerous because it has neither odor, nor taste, nor color. It is non-irritating, so humans are unable to detect it [41].

Exposure to oxides of nitrogen aggravates respiratory problems and leads to airway inflammation [42]. Also, nitric oxide (NO) oxidizes in the atmosphere to form NO_2, and upon reaction with sunlight, NO_2 decomposes into NO and O. The oxygen atom combines with an oxygen molecule to form ozone, O_3 [43]. Ground level ozone irritates the throat and causes respiratory problems and aggravates respiratory diseases. It also causes significant damage to trees and crops [44]. In addition, ozone, atomic oxygen, and molecular oxygen can also react with hydrocarbons in the atmosphere to form highly reactive hydrocarbon free radicals, which in turn can react with NO_2, thus forming the components of smog [43]. Finally, NO_x can react with other compounds in the atmosphere to form ultrafine particles [42].

In this work, the word soot is used to describe the carbonaceous fraction of non-soluble particulate matter that form during the combustion in the cylinder of a Diesel engine. In general, particulate matter is classified by its size. The first subclassifications are fine and ultrafine particles. Fine particles are divided into two size classes, those with aerodynamic diameters less than 10 μm (PM_{10}) and those with aerodynamic diameters less than 2.5 μm ($PM_{2.5}$). Strictly speaking, $PM_{2.5}$ means that 50% of the particles classified as $PM_{2.5}$ are passed through a selective size inlet with an aerodynamic diameter of 2.5 μm, and the same is true for PM_{10} [45]. Ultrafine particles are defined as having aerodynamic diameters of less than 100 nm.

A significant amount of fine and ultrafine particulates found in the atmosphere are attributed to fossil fuel combustion. Figure 2-5 shows the contributions of various natural and anthropogenic sources to PM_{10} and $PM_{2.5}$ for the year 2008 in the United States [46].

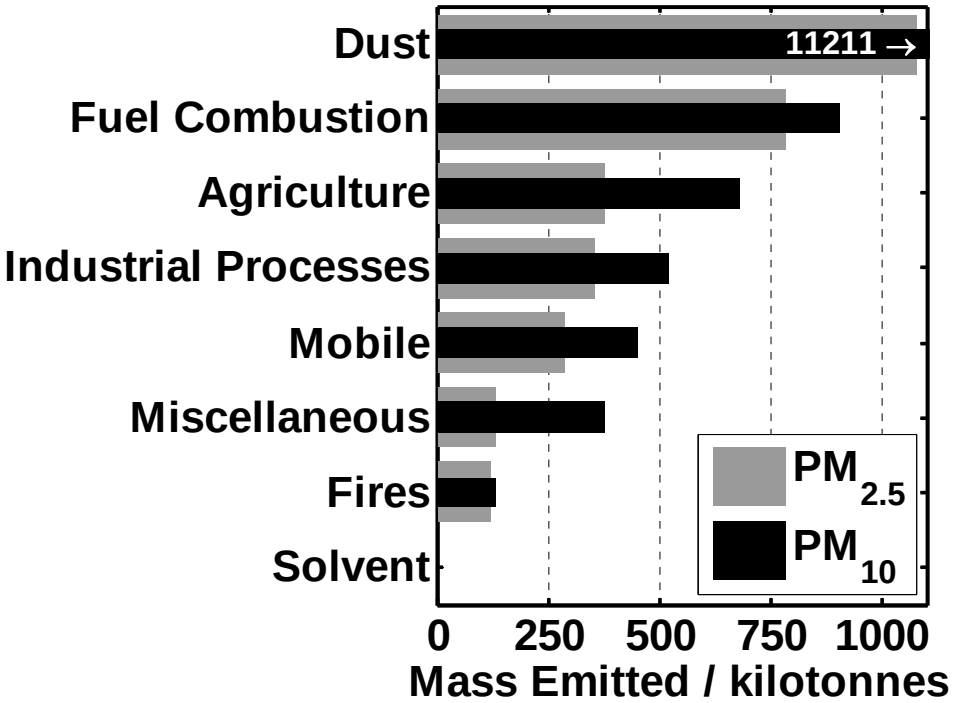

Figure 2-5: 2008 emissions of PM2.5 and PM10 in the United States (data from [46])

Fuel combustion is comprised of the following categories: residential; electricity generation; coal and biomass-fired industrial boilers; oil, gas, and other industrial boilers and stationary internal combustion engines; and commercial / institutional. Mobile sources include: non-

road, on-road, commercial marine vessels, locomotives, and aircraft. The contributions of oil, gas and other industrial boilers and stationary internal combustion engines, plus all mobile sources excluding aircraft account for nearly 14% of all $PM_{2.5}$ and less than 4% of all PM_{10} [46].

Ultrafine particles represent the biggest threat to human health, not just because of their large surface area and very high content of potentially toxic hydrocarbons, but also because their small size allows them to penetrate deeply into lung tissue [47]. The large surface area allows the particles to absorb metals, organic compounds, or biological material [48]. This causes inflammation in lung tissue and ultrafine particles have been observed to cross the blood-brain barrier. It is questioned if inhaled ultrafine particles may also have an affect on the central nervous system [49]. Fine particulates have been linked to a variety of cardiovascular problems [50].

2.2.1. Unburned Hydrocarbons and Carbon Monoxide

Unburned hydrocarbon emissions from Diesel engines are a product of incomplete combustion. When local conditions in the combustion chamber are too lean due to overmixing, the combustion reactions may be too slow to completely oxidize the fuel. Locally overrich conditions can also lead to poor combustion characteristics and unburned hydrocarbon emissions. Quenching at the combustion chamber walls can stop combustion reactions before they complete and also contribute to unburned hydrocarbon emissions. Finally, liquid fuel in the sac volume and nozzle holes of the injector is often released into the cylinder late during the expansion stroke when temperatures are not high enough to completely oxidize the fuel, which also contributes to unburned hydrocarbon emissions. [51]. Carbon monoxide (CO) emissions from Diesel engines have been traditionally considered insignificant [51], but the utilization of low temperature combustion systems can indeed lead to CO emissions, particularly in the regions of the cylinder with leaner mixtures [52]. The oxidation of both CO and hydrocarbons is strongly dependent on reactions with the OH radical [53]. The existence of OH radicals during combustion is known to be very strongly temperature dependent. The oxidation of CO to CO_2 requires the OH radical to be present, but the reaction has a very low activation energy [51, 54]. Hydrocarbons are also susceptible to oxidation by OH radical attack, and OH reacts much more readily with hydrocarbons than it does with CO (by nearly a factor of 10) [54]. Thus, as combustion temperatures become cooler with increasing charge dilution, leaner mixtures, and later crank angles, it is expected to see first an increase in CO emissions, followed by increases in unburned hydrocarbon emissions [54]. An example of this behavior is observed in the results of the homogeneous reactor simulations performed by Miles et al. for an early fuel injection case [52]. Because Diesel engines operate under globally lean air-fuel ratios, the exhaust gas is an oxidative environment, so engine-out unburned hydrocarbons and CO can be oxidized with an oxidation catalyst, provided the exhaust temperatures are adequately high.

2.2.2. Soot

Determining the mechanisms of soot formation and oxidation directly in a Diesel engine with Diesel or Diesel-like fuels is difficult. Instead, much of what is experimentally determined about these mechanisms comes from carefully controlled experiments performed on laboratory flames, be they premixed, partially premixed, or diffusion flames, both laminar and turbulent, counterflow and co-flow. Much research work is do be done if a full understanding of soot formation mechanisms for larger hydrocarbons that are more representative of real fuels used in practical combustion devices [55].

It is known that soot forms during high temperature combustion or pyrolysis of hydrocarbon fuel and is comprised of small particles. Formation begins at temperatures above approximately 1300 K and increases with decreasing air-fuel equivalence ratio. The particles are comprised primarily of carbon but contain small amounts of hydrogen, oxygen, and traces of other elements (nitrogen, sulfur). Ebert presented strong evidence that soot particles are made up of stacks of flat polyaromatic hydrocarbons (PAHs) that contain larger numbers of benzene rings (> 4) [56]. Tunneling electron microscope images have claimed that the structure of some soot agglomerates contains crystallite planes [57]. Zhu et al. show that the structure of the primary soot particles formed at high loads and thus high temperatures is more graphitic and ordered than for particles formed at lower loads [58]. Thus, primary soot particles are three-dimensional conglomerates of two-dimensionally-formed PAHs, and the structure of these particles depends on the thermochemical environment in which they were formed. Understanding the mechanisms of soot formation and oxidation therefore requires an understanding of fuel decomposition, the gas phase chemistry leading up to the formation of the first small aromatic molecules, the growth of aromatic molecules into PAHs, the combination of these PAHs into soot particles, the interactions that may occur between soot particles, any aging processes to which these soot particles may be subjected, and particle oxidation mechanisms. Multiple rate limiting steps are involved in the soot formation process, and the mechanisms involved are highly dependent on fuel composition, local temperatures, and flame chemistry.

The first step in the soot formation process is the high temperature chemical decomposition of the fuel, which is often referred to as pyrolysis. These complex reaction pathways are strongly dependent on the structure of the fuel components, as well as on stoichiometry and the thermodynamic state of the fuel. Because the fuel in a Diesel engine is heated and vaporized by mixing with hot air, and because the fuel itself may contain some oxygen, the decomposition takes place in an oxygen poor, but not necessarily oxygen-free, environment. Diesel fuel is comprised primarily of alkanes with 5-20 carbon atoms, but generally contains alkenes and aromatics as well [55]. The premium quality Diesel fuel used in this work contains approximately 16% aromatics by weight, and the vast majority of those are monoaromatics.

McEnally et al. identify two decomposition mechanisms for larger, non-cyclic alkanes: H abstraction and C-C fission [55]. Abstraction of H atoms from these alkanes occurs primarily via reactions with other H atoms, but OH radicals can extract H atoms under premixed conditions. C-C fission occurs when the carbon backbone of the fuel molecule is broken between two neighboring carbon atoms. The H-abstraction mechanism is often dominant, but the ratio of these two decomposition pathways depends on the temperature and the chemical environment [55]. The products of these first decomposition steps are alkyl radicals of many different sizes and depend on the original fuel components. These radicals can isomerize or decompose into alkenes via further high-temperature, endothermic decomposition reactions.

So, upon high temperature decomposition, a large alkane will produce a wide variety of radicals and alkenes with smaller carbon numbers. These molecules can decompose further or combine with other molecules to produce precursors to benzene molecules, the simplest aromatic ring structures. A particularly important radical is the propargyl radical ($HC{\equiv}C\text{-}CH_2\text{-}$), which forms through a wide array of mechanisms that depend on the chemical environment and the thermodynamic state. The C3 and larger alkenes make up a small fraction of the total alkene concentration, but they play an important role in the formation of aromatics.

There are many reaction mechanisms that produce benzene (the simplest aromatic molecule) in a flame, and the global combination reactions include every possible size combination: C3-C3, C4-C2, C5-C1, and C6 [55]. Their relative importance depends on the fuel composition and the decomposition mechanisms of the individual fuel components. The same can be said for napthalene, the simplest two-ring aromatic molecule. It is believed that the addition of the first ring to an aromatic molecule is a rate-controlling step in flames, and this process is very sensitive to fuel structure.

McEnally et al. also discuss the role of fuel-borne aromatics in the aromatic formation process [55]. Even low concentrations of aromatics in a fuel can have a dramatic effect on the sooting characteristics of the fuel. They cite studies that suggest that the benzene rings in the fuel are not broken down, but form the initial structure for aromatic molecule growth. In this way, the rate-limiting processes otherwise involved in the formation of the first aromatics are bypassed, so soot formation rates are significantly higher.

Once the small aromatic molecules, or PAHs, have reached a considerable size (this is typically taken to be three aromatic rings), the further PAH growth process is often modeled as a fuel-independent polymerization process [59]. Polymerization of PAHs can be assumed to take place faster than convection and diffusion of PAHs, so the growth of smaller PAHs into larger ones is said to be a fast polymerization process [60]. Here, temperature plays an important role in the growth and fragmentation of PAH molecules, and the formation is highly kinetically controlled [61]. Models exist that take convection and diffusion of PAHs into account as means of increasing PAH molecule size, but they are not discussed here [59]. Mauss et al. model the polymerization process with the hydrogen abstraction carbon addition ring closure (HACARC) reaction mechanism shown in Figure 2-6 [60]. Such mechanisms form the backbone of PAH formation models, but other reaction pathways and their fuel dependencies complicate the process. It is not known if the number of PAH formation pathways and thus of soot formation pathways is finite for real combustion systems [61].

$$
\begin{aligned}
&1.a \quad P_{i,1} + H \leftrightarrow P_{i,2} + H_2 \\
&1.b \quad P_{i,1} + OH \leftrightarrow P_{i,2} + H_2O \\
&1.c \quad P_{i,1} + O \leftrightarrow P_{i,2} + OH \\
&2. \quad P_{i,2} + H \rightarrow P_{i,1} \\
&3. \quad P_{i,2} + C_2H_2 \leftrightarrow P_{i,3} + H \\
&4.a \quad P_{i,3} + H \leftrightarrow P_{i,4} + H_2 \\
&5. \quad P_{i,4} + H \rightarrow P_{i,3} \\
&6. \quad P_{i,4} + C_2H_2 \leftrightarrow P_{i,5} \\
&7. \quad P_{i,5} + C_2H_2 \leftrightarrow P_{i+1,1} + H \\
&8.a \quad P_{i,6} + H \leftrightarrow P_{i,5} + H_2 \\
&9. \quad P_{i,5} + H \rightarrow P_{i,6} \\
&10.a \quad P_{i,6} + OH \rightarrow P_{i,3} + CHO + CH_2 \\
&10.b \quad P_{i,3} + OH \rightarrow P_{i,1} + CHCO \\
&10.c \quad P_{i,1} + OH \rightarrow P_{i-1,6} + CHCO \\
&11.a \quad P_{i,5} + O_2 \rightarrow P_{i,3} + 2CO \\
&11.b \quad P_{i,4} + O_2 \rightarrow P_{i,2} + 2CO \\
&11.c \quad P_{i,2} + O_2 \rightarrow P_{i-1,5} + 2CO
\end{aligned}
$$

Figure 2-6: HACARC reaction mechanism

Here, $P_{i,1}$ represents a PAH that grows via hydrogen abstraction and carbon addition. Following Mauss et al., the reaction mechanism is shown in Figure 2-7 with pyrene as $P_{i,1}$ [60].

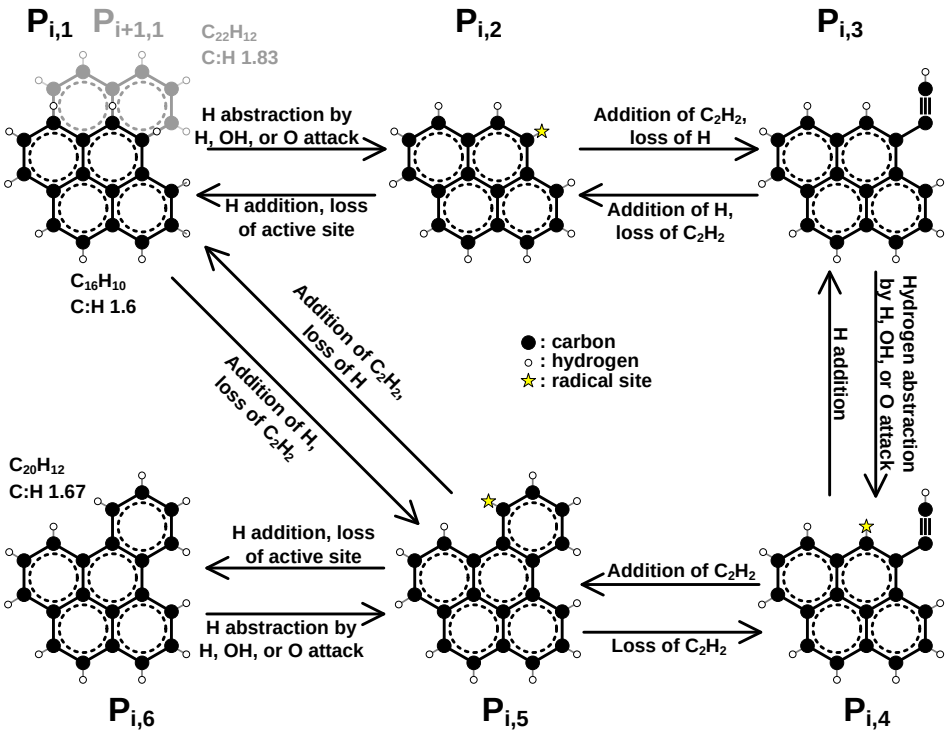

Figure 2-7: Particle growth with the HACARC mechanism

Reactions 1.a, 1.b, and 1.c involve the abstraction of an H atom from an edge site of the PAH by either an H, an OH, or an O radical, with H_2, H_2O, or OH as a byproduct, respectively. This leaves the PAH, $P_{i,2}$, with a radical site that can be deactivated via the reverse of reactions 1.a-1.c or through the addition of an H atom (reaction 2). The H atom is considered to be one of the most important abstracting radicals because its concentration is higher than that of other radicals and because its small mass leads to a collision frequency per unit concentration that is higher than for other radicals [62]. Radical site deactivation by hydrogen addition plays an important roll at high pressures [59]. In reaction 3, carbon is added to the PAH in the form of acetylene (C_2H_2), and an H radical is given off; this reaction produces the molecule $P_{i,3}$ and is reversible. Reactions 4.a-4.c are very similar to reactions 1.a-1.c and create a second radical site on the molecule, which now takes the form of $P_{i,4}$. As was the case with reactions 1.a-1.c, this radical site can be deactivated either by the reverse of reactions 4.a-4.c or by the addition of an H atom (reaction 5). An acetylene molecule can be added to this reactive site, thus closing a new ring and creating a larger PAH ($P_{i,5}$, reaction 6) with a single active site. Reaction steps involving the addition of acetylene are highly reversible and considered to limit PAH growth, and PAHs nearly always take on the stablest, most condensed forms with the rings being as fused together as possible [59]. Reaction with a further acetylene molecule at this active site closes a second ring and creates the PAH $P_{i+1,1}$ (reaction 7). Alternatively, this radical site can be deactivated by the reverse of reactions 8.a-8.c or through H addition (reaction 9), thus forming $P_{i,6}$. An important feature of this reaction mechanism is the role of water. Its presence in the chemical environment shifts the equilibrium of the H abstraction reactions 1.b, 4.b, and 8.b, thus decreasing the formation rate of radical sites and therefore PAH growth rates. Reactions 10.a-10.c and 11.a-11.c describe oxidation of the PAH molecules by OH or O_2, which involves breaking the molecules down into smaller PAHs. It has been determined that oxidation with O_2 is the primary means of oxidizing PAHs [59]. As the PAHs grow by this mechanism, the C:H ratio of the molecules increases; this is shown in Figure 2-7.

At the same time that PAH growth occurs, coagulation of PAHs also takes place. Although the process and the underlying bonding mechanisms are not well understood, it is believed that when two PAH monomers collide, they stick together in an irreversible reaction and form a dimer. The formation of such dimers is representative of the transition between the gas phase and the solid phase in the soot formation process. Further coalescence reactions involving dimers lead to the formation of trimers, tetramers, and larger particles [59]. The frequency of these collisions is dependent on the temperature, the masses of the two species, and the collision diameters of the species [63]. The collision frequency is increased by van der Waals forces, temporary dipole moments that form as a result of fluctuations in the electronic structure of the molecules. These polymers are considered to be the first soot particles and are called nuclei, so the process of PAH coalescence is called nucleation. The activation energy for particle nucleation is relatively high [64], and the process occurs at temperatures ranging from 1300 K to 1600 K [65]. Particle nuclei are approximately 2 nm in size and approximately spherical; they do not contribute directly to the total mass of particles formed to a significant extent. However, the number of particle nuclei formed has a substantial influence on the amount of soot formed, because particle nuclei provide the surface area required for growth through mass addition to occur. This has been identified as the reason why richer flames produce more soot than leaner flames [64].

Soot particle growth from the nuclei stage takes place via three mechanisms: coagulation, surface growth, and agglomeration. Coagulation occurs when two particles collide and coalesce to form a larger particle. Mass is not added to the particle, nor is the particle volume fraction in a flame affected by coagulation. This process decreases the number of particles, but broadens the particle size distribution as sizes increase. The ultimate size of particles formed during the combustion process is determined largely by the coagulation process [59]. The collision frequency of particles is enhanced by van der Waals forces, which depend on the sizes of both particles involved in a collision. Models that take the size distribution of particles into account typically assume a size-independent collision enhancement factor of 2.2 [66]. The shape of particles formed as a result of coagulation is nearly spherical. Coagulation alone acts to decreases the surface area of the particle available to take part in growth and oxidation reactions [64, 66].

The mechanism responsible for the majority of soot mass addition is surface growth, which occurs simultaneously with coagulation [65, 64]. Surface growth is determined primarily by two processes: PAH condensation on the particle surface and acetylene addition. The relative importance of these processes depends on the experimental conditions [59], and residence time of a particle in a growth-promoting environment determines to a large extent its final mass. Surface growth increases particle size and mass without changing the number of particles. Smaller particles have more reactive radical sites than larger ones and thus exhibit higher surface growth rates [65]. Analyses of TEM images of the soot particles collected in the exhaust of Diesel engines suggest that the primary particles are of between 20 and 35 nm diameter, depending on the engine operating conditions [67]. High temperatures, locally leaner air-fuel ratios, and shorter residence times tend to result in smaller primary particle sizes, whereas lower temperatures and longer residence times with locally rich air fuel ratios yield larger primary particles [57, 58].

Agglomeration occurs when primary particles, or groups of primary particles, collide and stick together. The shape of the primary particles remains essentially unchanged by this process. Depending on the operating conditions, the agglomerate that is formed can be chainlike, with distinctly visible primary particles, or clustered, whereby it becomes more difficult to identify the individual spherules. The structure of the agglomerates has been observed to be more chainlike at higher engine loads. At lower loads, the primary particles are

fused together to make a more compact structure [57]. Here, too, the dynamic and inhomogeneous thermochemical environment inside the combustion chamber plays a decisive role in the final form of soot agglomerates.

Oxidation of soot particles occurs during all stages of the formation process [65]. During this process, carbon atoms are oxidized first to CO and finally to CO_2. Once a carbon atom has been oxidized to CO, it will not participate in soot formation, regardless of the thermochemical environment to which it is exposed [65]. The oxidation of soot is a temperature dependent process that begins at a lower temperature limit of approximately 1300 K, and increases with increasing temperature [68]. Glassman et al. argue that if soot particles remain in an oxidizing environment at a temperature of 1300 K or more, the particles can be oxidized [69]. Oxidation by OH radical attack is the dominant source of soot oxidation in flames, but for lean, low-temperature combustion conditions under which OH concentrations are low, oxidation with O_2 becomes more important [70].

Some examples of the effects of EGR and the use of biofuels on the oxidation mechanism of soot particles, are given in [71] and [72]. These findings indicate that the thermochemical environment in which soot particles are formed, as well as the fuel composition, have a significant effect on the way in which the soot particles are oxidized after they leave the engine. This is a result of the differences in the soot formation processes caused by the variations in fuel or in oxygen concentration.

2.2.3. NO_x

Three kinds of mechanisms are responsible for the formation of NO during combustion of fuels with low amounts of fuel-bound nitrogen [73, 74, 75]:

1. Thermal NO
2. Prompt NO
3. NNH Mechanism

The third mechanism is not considered to be significant and is not discussed here. The discovery of the first mechanism is attributed to Zeldovich [76] and thus is often called the Zeldovich mechanism. It is the dominant NO formation mechanism for high temperature combustion for a wide range of fuel-air ratios [75]. The basic mechanism is comprised of two reactions:

$$O + N_2 \leftrightarrow NO + N \quad (2.1)$$

$$N + O_2 \leftrightarrow NO + O \quad (2.2)$$

The first reaction involves the combination of atomic oxygen with nitrogen from the air. This endothermic, rate-limiting reaction has a high activation energy due to the very stable triple bond in the N_2 molecule. It is typically considered to be active at temperatures above 1800 K [75]. The N radical formed by the progression of the first reaction reacts almost immediately with oxygen to form another NO molecule and an O atom, which is shown by the second reaction [77]. The mechanism was extended (for example by Lavoie et al.) to include the following reaction, which also proceeds very rapidly [77, 78]:

$$N + OH \leftrightarrow NO + H \quad (2.3)$$

This reaction is believed to be significant [51] and the combination of the three reactions is referred to as the extended Zeldovich mechanism. It is relatively slow compared to the fuel oxidation reactions [75]. NO formation rates are very strongly dependent on temperature [51], so the formation of NO is affected by changes in flame temperature, but also on mixing with cooler air or burned gases, which occurs in a Diesel engine. Expansion of the cylinder

contents is also responsible for cooling. NO decomposition is also temperature dependent, and below a certain temperature, the decomposition is very slow and the NO concentration is said to be “frozen” [51].

Prompt NO can be used to describe a number of mechanisms that are responsible for NO formation rates faster than those estimated with the Zeldovich mechanism [73]. One possibility for the formation of prompt NO is the existence of non-equilibrium concentrations of O and OH in the reaction and burned zones, which accelerates the thermal NO mechanism. Another formation mechanism was proposed by Fenimore [79] in 1971. Its chemical kinetics are involved with the combustion chemistry of hydrocarbon fuels and much more complicated than those involved with the thermal NO mechanism. It is still not well understood, but it is believed that Fenimore NO plays an important role in fuel-rich combustion [79]. The initiation reactions, which are rate limiting, take place between small species that contain hydrocarbons and molecular nitrogen , for example [74, 80]:

$$CH + N_2 \rightarrow NCN + H \qquad (2.4)$$

More information about this mechanism can be found in [73, 74, 80] and the references therein.

Another prompt mechanism is called the N_2O-intermediate mechanism and involves the following three reactions [75]:

$$O + N_2 + M \leftrightarrow N_2O + M \qquad (2.5)$$

$$H + N_2O \leftrightarrow NO + NH \qquad (2.6)$$

$$O + N_2O \leftrightarrow NO + NO \qquad (2.7)$$

This mechanism is most important when NO formation rates are relatively low [73], for instance in lean, low-temperature conditions [75].

Burned gases under equilibrium conditions at combustion temperatures do not contain significant amounts of NO_2, but under some operating conditions, Diesel engines are known to emit NO_2. It is believed that NO_2 forms by the following reaction [51]:

$$NO + HO_2 \rightarrow NO_2 + OH \qquad (2.8)$$

NO_2 can react with atomic oxygen to form NO:

$$NO_2 + O \rightarrow NO + O_2 \qquad (2.9)$$

This second reaction can be hindered if NO_2 is mixed with cooler gases, as may occur in a Diesel engine.

2.3. State of the Art for Heavy Duty Diesel Engines

One of the most significant challenges for Diesel engine developers is presented by ever-tightening emission regulations, particularly for NO_x and particulate matter (PM). Shown in Figure 2-8 are the legislated NO_x and PM emission limits for heavy duty Diesel engines in the US and in Europe since 1990.

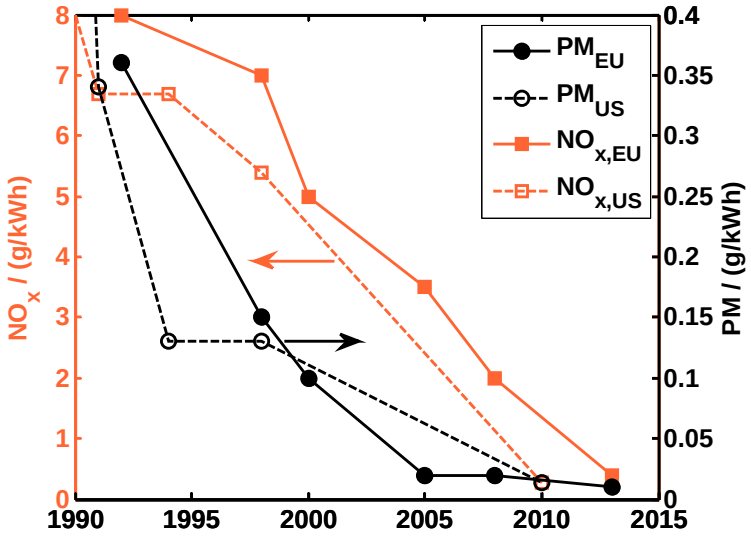

Figure 2-8: NO_x and PM regulations for heavy duty Diesel engines since 1990 [81]

The newest generation of heavy duty Diesel engines has been successfully designed to meet the most modern emissions regulations. A variety of modern technologies and continuous improvements in exhaust aftertreatment systems have made these advances possible. Table 2-1 shows some examples of heavy duty Diesel engines that meet the Euro-VI regulations and some of the enabling technologies.

Table 2-1: Survey of heavy duty engines that are Euro-VI compliant. DPF: Diesel particulate filter; SCR: selective catalytic reduction; ASC: ammonia slip catalyst; n.A.: not available [82,83,84,85,86,87]

		Daimler Series 93x	Yuchai 6L-60	Daimler OM470	Scania DC13	Volvo D13
Displacement volume	L	5.1-7.7	8.4	10.7	12.7	13.0
Rated power	kW	110-260	n.A.	240-315	324-353	338
Compression ratio	-	17.6	n.A.	17.6	17.3	n.A.
Turbocharging	-	Single or 2-stage	2-stage	Single stage, asymmetric turbine housing	VGT	VGT
Injection system	-	Common rail	Common rail	Pressure Amplified Common Rail	Common rail	Unit injectors
Cooled EGR	-	✓	✓	✓	✓	✓
Oxidation Catalyst(s)	-	✓	n.A.	✓	✓	✓
DPF(s)	-	✓	✓	✓	✓	✓
SCR Catalyst(s)	-	✓	✓	✓	✓	✓
ASC(s)	-	✓	n.A.	✓	✓	✓

All of the engines listed in the table are equipped with cooled EGR, but it is used for different purposes. For instance, with the Daimler series 93x, EGR is used even at high loads [82], whereas the Volvo D13 uses EGR to manage exhaust temperatures for the SCR system and not at all under highway cruising conditions [87]. Maximum injection pressures are between 2100 and 2400 bar, and maximum cylinder pressures, when provided by the manufacturer, are on the order of 200 bar. The number of injector holes, when given, ranges from 7 to 10. The engine control system of each engine has been developed in conjunction with the exhaust aftertreatment system. The typical arrangement of components in such a system is shown in Figure 2-9.

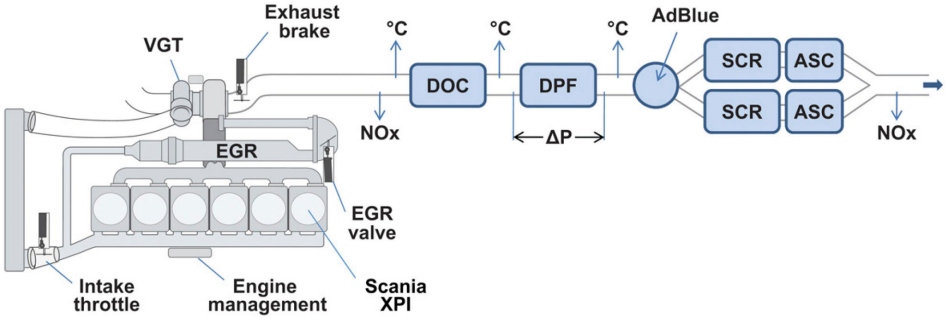

Figure 2-9: Example of an exhaust aftertreatment system to meet Euro VI regulations (taken from [85])

Exhaust backpressure for EGR is provided in this case by the variable geometry turbine in the exhaust. The first aftertreatment component in the exhaust is the oxidation catalyst. This oxidizes unburned hydrocarbons and CO, and produces NO_2 that is used for the passive regeneration of the particulate filter. The filter is placed closely behind the DOC and, in most cases, is passively regenerated. When active filter regeneration is necessary, exhaust temperatures are increased either with a post injection late in the expansion stroke or with an extra fuel injector upstream of the DOC in the exhaust. The Daimler 93x series makes use of a cam phaser on the exhaust cam to help increase exhaust temperatures for the aftertreatment system [82]. The urea/AdBlue injector injects a urea solution into the exhaust stream. This quickly breaks down into ammonia, which is utilized by the SCR catalyst to selectively reduce NO_x. To prevent ammonia emissions, particularly during transient operation, ammonia slip catalysts are positioned directly downstream of the SCR catalysts. NO_x is measured before the DOC and after the ASCs; temperatures are measured before and after the DOC and the DPF; the pressure drop across the DPF is also monitored. The added complexity for the application of such a system is considerable.

Many of the measures taken to meet emissions regulations have a negative influence on the fuel economy of the engine. These can include [88]:

- Retarded combustion phasing to provide adequately high exhaust gas temperatures for the aftertreatment system
- Increased exhaust backpressure due to the exhaust aftertreatment system
- Increased flow losses through the cylinder head as the amount of charge increases with high EGR rates and high engine loads
- Increased gas exchange losses resulting from two stage turbocharging
- The increase in coolant flow rates required by the cooling system to provide cooling for EGR and the intercooler

The use of exhaust gas aftertreatment means higher system costs and complexity. In addition, it creates packaging problems and adds weight. As expected, these problems lead researchers to search for ways to reduce engine out emissions with the intent of eliminating exhaust aftertreatment. Wirths et al. examined the limits of low-NO_x, low-soot operation with a combination of thermodynamic measurements, optical diagnostics, and three dimensional simulations [89]. Very low in-cylinder oxygen concentrations are achieved through the use of very high EGR rates, and high boost pressures are used to provide enough total oxygen so that mid-load operating points can be investigated. Combustion phasing is often earlier than with traditional Diesel combustion, so peak cylinder pressures are near 200 bar, even for mid-load operation. The authors conclude that such an operating strategy exhibits poorer fuel economy than a contemporary strategy with an SCR system. Polonowski et al. developed a leaner

lifted-flame combustion (termed LLFC) strategy with the purpose of eliminating one or more aftertreatment devices [33]. Their aim was to eliminate soot emissions to the furthest extent possible by maintaining fuel-air equivalence ratios lower than two at the lift-off length. Difficulties with re-entrainment of burned gases and decreasing lift-off lengths due to interactions between jets create richer conditions and thus lead to soot emissions. They explain that not only must the conditions at the beginning of the injection allow for longer lift-off lengths (temperatures must not get too high and the gas mixture must not react too quickly), but the effects of the combustion on the ongoing mixture formation process must also be considered. EGR can be used to effectively reduce NO_x emissions, but only to the extent that the effects mentioned above can be avoided so that soot is not produced.

3. Experimental Setup and Measurement Techniques

3.1. Optically Accessible Engine

The optically accessible single cylinder Diesel engine employed in this work has been purpose built to facilitate optical and laser optical measurements. It is based on the Mercedes Benz OM450 heavy duty Diesel engine. The crankcase, crank train, and valvetrain have not been changed from their original design. The production cylinder head, cylinder liner, and piston have been modified to provide optical access into the combustion chamber near top dead center. A custom cylinder housing has been designed to house the production cylinder liner and support the cylinder head and valvetrain. Pertinent geometrical data for the engine are shown in Table 3-1, and a cross sectional view of the engine is shown in Figure 3-1.

Table 3-1: Optically accessible engine data

Valves	4	-
Optical accesses	3	-
Bore	128	mm
Stroke	142	mm
Connecting rod length	256	mm
Compression ratio	16.1:1	-
Maximum engine speed	2000	rpm
Intake valve opening*	1°	ATDCe
Intake valve closing*	185°	ATDCe
Exhaust valve opening*	125°	ATDCf
Exhaust valve closing*	5°	BTDCe

*Valve events defined as the point of 0.15 mm valve lift

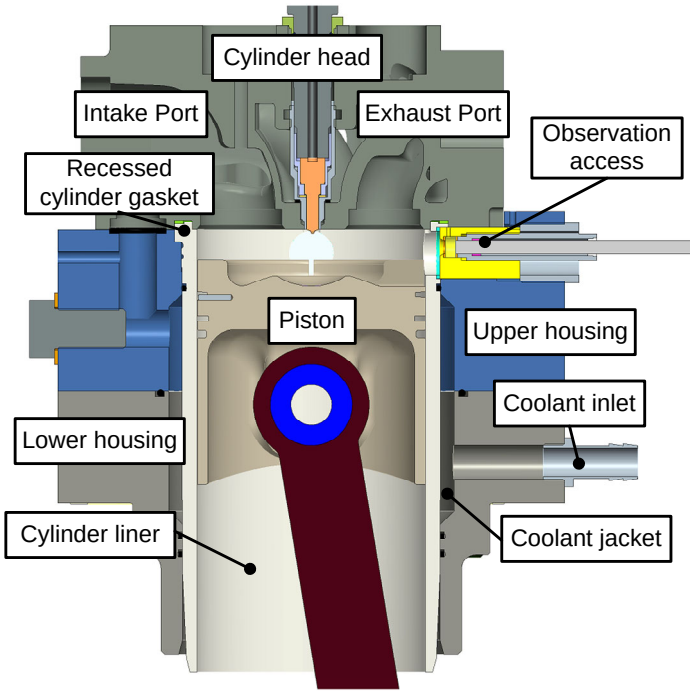

Figure 3-1: Cross sectional view of the optically accessible engine

The cylinder housing is comprised of an upper and a lower housing. It houses and cools the cylinder liner, provides oil and coolant to the cylinder head through the corresponding inlets in the cylinder head, and is integral to the optical accessibility of the combustion chamber. Both parts of the housing have been CNC machined from a large piece of 42CrMoS4 round stock. The high strength of this material is well suited for applications involving threaded bores that are cyclically loaded, and the sulfur content improves its machinability.

The production cylinder head has been modified to enable optical access even at top dead center. For this purpose, a precisely milled groove has been machined into the lower surface of the head. This raises the position of the cylinder liner and enables the three optical accesses to be placed directly below the cylinder head.

Some optically accessible Diesel engines are built so that part or all of the cylinder liner is made of quartz glass [90, 91, 92, 93]. However, there are drawbacks associated with the use of a quartz glass cylinder. Such an engine is often limited in terms of both the loads and temperatures that the materials can withstand, although this problem can be avoided with a pressurized double-ring system [94]. The compressive strength of typical technical fused quartz glass is more than 20 times greater than its tensile strength [95]. Therefore, a design that utilizes compressive loading of quartz elements will be inherently stronger than one in which quartz is loaded in tension, i.e. an internally-pressurized quartz cylinder. Sealing a quartz glass cylinder liner is challenging as the thermal coefficient of expansion of steel is approximately 20 times that of quartz glass. The thermal conductivity of quartz glass is less than $1/20^{th}$ that of steel, so heat transfer and cylinder wall temperatures would be significantly different with a quartz glass cylinder liner. Consequently, the combustion characteristics in a Diesel engine with a quartz glass cylinder liner would likely be much different than those found in a metal engine. Hence, it is desirable to decrease the size of the optical accesses to minimize these effects on the in-cylinder processes. Passing a vertically-oriented light sheet through a transparent cylinder liner results in portions of the light sheet being internally reflected; this phenomenon manifests itself in the form of bright lines on the resulting images and makes processing of data in these regions very difficult.

If the cylinder liner is an extension of the existing liner or if images are taken through the piston from below, then an extended piston is also necessary. While this design allows for a wide variety of measurements, it has disadvantages at higher engine speeds and often requires a special compression ring design. Often, these pistons are built with a flat quartz window through which the optical measurements are taken. A quartz glass piston top with a steep-sided piston bowl would be prohibitively expensive and optically complex [96].

For these reasons, an engine design was chosen with three large, flat optical accesses, two located diametrically opposed from one another and the remaining one oriented perpendicularly to the first two. Similar concepts have previously been developed and successfully implemented elsewhere [97, 98]. This design enables a vertically-oriented light sheet to be passed through the cylinder, where it can be observed from the remaining optical access via an endoscope or a far field microscope. As explained in [99], this configuration is advantageous because the light sheet can intersect with the axis of an injected fuel jet, rather than crossing it horizontally. This configuration makes RAYLIX measurements (see 3.3.3: RAYLIX) inside the combustion chamber possible. A further advantage is realized in that the optical accesses can rather quickly be removed, cleaned and replaced without having to remove the cylinder head. Figure 3-2 depicts the combustion chamber of the engine, including the optical accesses.

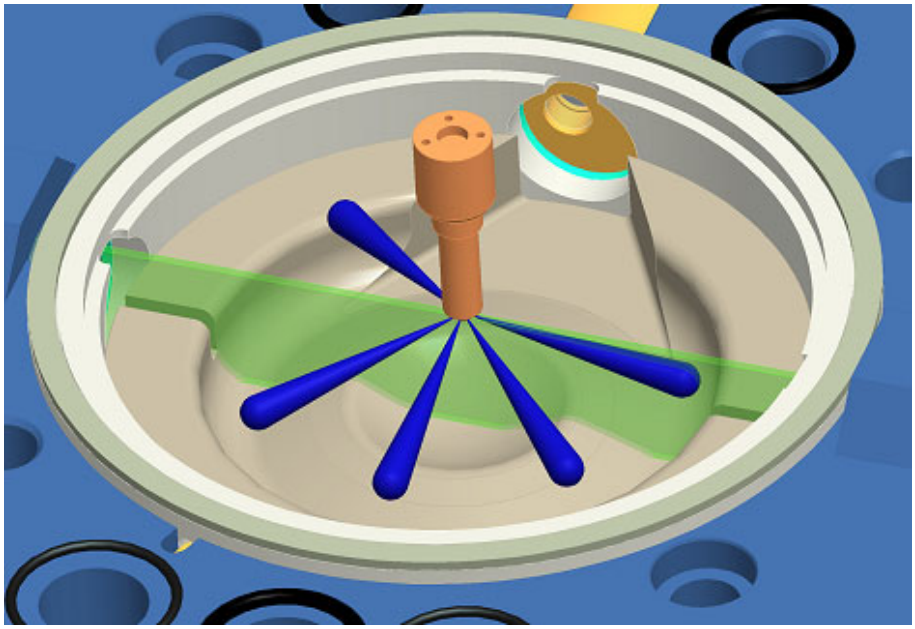

Figure 3-2: Combustion chamber with endoscopic access, slotted piston and laser sheet

Two round quartz glass accesses allow the passage of a laser light sheet (also shown in the figure) into and out of the combustion chamber. The third access, seen at the back of the cylinder allows perpendicular or near-perpendicular observation of the combustion chamber.

Two piston designs are employed in this work, both of which have been modified with an observation cutout. They differ in that one design has additional slots cut into the piston crown for the laser light sheet and the other has none. The observation cutout of the piston without slots is widened slightly to match the compression volume of the slotted piston. CAD images of both pistons are shown in Figure 3-3.

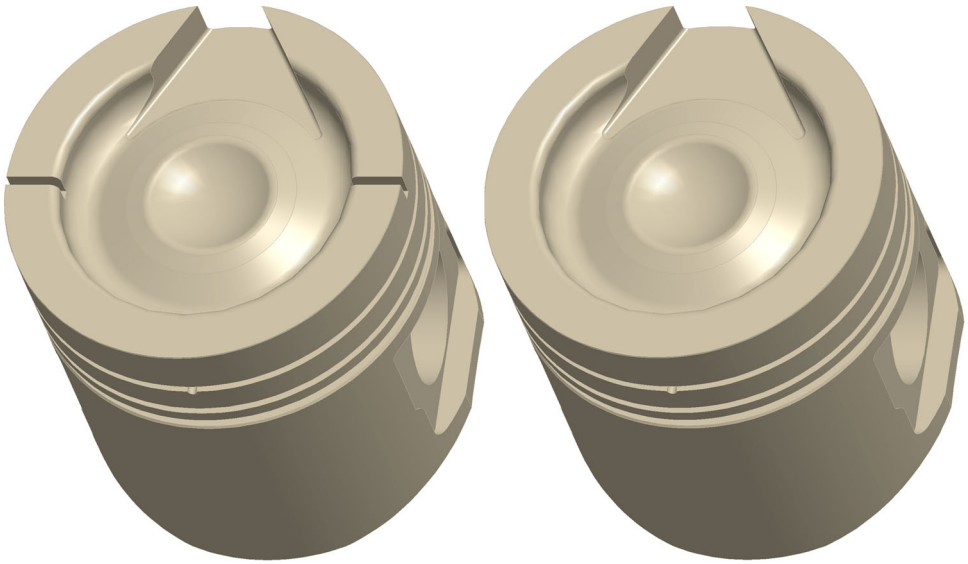

Figure 3-3: Piston designs. Left: observation cutout and slot for laser sheet; right: modified observation cutout and no laser sheet slot

The effects of these modifications on the in-cylinder flow has been examined via 3D-CFD simulations in [6] for the piston design shown on the left. The flow is characterized by a weak swirl motion, which is affected by the presence of the observation cutout in that a

recirculation zone builds there. Because there are no spray jets directed into this portion of the cylinder, it is not assumed that the observation cutout has a significant impact on the combustion. The squish flow induced between the piston bowl rim and the cylinder head is impacted by the laser sheet slots, so the second piston is used when a laser sheet is not used to minimize the effects of the piston modifications on the in-cylinder flow when possible.

The fuel injector is a Bosch CRIN3-18 solenoid injector with five holes, each with a hole diameter of 139 μm. The spray pattern is based on a seven-hole injector design and is also shown in Figure 3-2. One jet has been removed so that the laser sheet interacts with only one jet. A second jet was removed to provide an unobstructed view of the imaging plane and the fuel jet of interest. More detailed geometric information about the injector nozzle geometry is shown in Table 3-2.

Table 3-2: Injector nozzle data

Number of holes	5	-
Included angle	162.5	°
Hole diameter	139	μm
Nozzle hole L/D	6.8	-
Nozzle hole conicity (ks)	1.5	-

3.2. Test Bench

Because the single cylinder engine used in this work is inherently unbalanced, it is rigidly mounted to its test bench, which has been weighted with several tons of steel to decrease the severity of the vibrations resulting from the engine's operation. The temperature and pressure of the lubricating oil and cooling water are maintained by an external conditioning system. Fuel pressure is supplied to a fuel rail mounted on the engine by an electrically driven Bosch CP3 high pressure fuel pump; injection pressure and timing are controlled with a Genotec control system. External boosting of the intake pressure is provided by a mechanical supercharger driven by a variable-speed electric motor, whereas exhaust backpressure is controlled by the position of an exhaust throttle valve. At the beginning of each experiment, the engine is motored by a DC electric motor. When the fuel injection is switched on and the engine begins producing power, the energy is absorbed by an eddy current brake, which is coupled to the electric motor and the engine via a freewheel clutch and a driveshaft, respectively.

Cylinder pressure is measured with either a piezoelectric transducer; either a Kistler 6061B or an AVL GH11C. Intake and exhaust port pressures are measured with a Kistler 4045A and a 4075A piezoresistive sensor, respectively. The measured voltages, along with the injector control current and various camera and laser control signals, are measured with an indicating system with a digitizing resolution of 12 bits and a crank angle resolution of 0.1°. Other measurements of temperature, pressure, and engine speed are recorded by a data acquisition system at a sampling rate of approximately 1 Hz. Exhaust gas components are measured with a standard exhaust gas analyzer and engine-out smoke is measured with an AVL 415S smoke meter.

A typical measurement procedure is as follows: first, the water and lubricating oil are brought up to temperature. Then, the optical accesses are tightened to their proper tightening torques of between 50 and 60 Nm, depending on the design. The high pressure fuel pump is switched on and the desired fuel rail pressure set point is dialed in. The engine is motored at near its desired speed, and the intake pressure is set by adjusting the supercharger's speed. The injection control signals are checked for proper phasing using the indicating system. Upon

recognition of proper signals, the fuel injection is switched on, and fuel is injected in each working cycle. The engine speed in fired operation is controlled by the eddy current brake. Once the engine is running, the exhaust backpressure is adjusted by changing the position of a throttle in the exhaust system. When all operating parameters have stabilized, the measuring process is started. After approximately five to 10 minutes of operation and depending on the operating point, the engine is stopped, the window or windows are removed, cleaned, and replaced, and the process is repeated.

3.3. Optical Measurement Techniques

3.3.1. Elastic Scattering

Many of the measurement techniques employed in this work make use of the elastic scattering and absorption that occurs when electromagnetic radiation in the form of light interacts with small particles or liquid droplets. Elastic scattering means that the wavelength of the scattered light is the same as that of the incident light. It is assumed that the scattering particles are spherical and isotropic, so these phenomena are described using Mie theory [100]. This theory, as any electromagnetic scattering theory, is based on the solution to Maxwell's equations; it can be extended to an ensemble of particles under the following assumptions [101]:

1. Each particle scatters light as a separate entity
2. There are no optical interferences between the waves of light scattered by various particles
3. Multiple scattering does not occur

The effectiveness with which a particle scatters light is typically expressed in terms of its scattering efficiency, which is defined as the ratio of the scattering cross section to the geometric cross section: $Q_{sca} = C_{sca} / \pi a^2$, where C_{sca} is the particle's scattering cross section and a is the particle radius. The intensity of scattered light is a function of the scattering angle, the particle size, the wavelength of the light, and the particle's index of refraction, which in the absence of absorption is a real number.

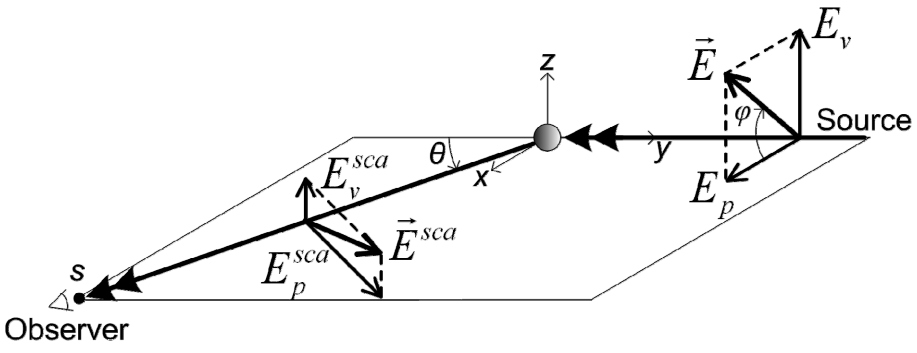

Figure 3-4: Elastic scattering

Figure 3-4 shows an incident light wave, a scattering particle, and an observer. The light waves are represented by their electric field vectors, which are in turn resolved into components perpendicular and parallel (E_v and E_p, respectively) to the plane formed by the source, the scattering particle, and the observer. The intensity of light is proportional to the square of its corresponding electric field. θ is the scattering angle and φ is the polarization angle of the incident light.

In general, the scattering by a particle is given by [102]:

$$\begin{pmatrix} E_p \\ E_v \end{pmatrix} = \begin{pmatrix} S_2 & S_3 \\ S_4 & S_1 \end{pmatrix} \frac{e^{-ikr+ikz}}{ikr} \begin{pmatrix} E_{p0} \\ E_{v0} \end{pmatrix} \tag{3.1}$$

where k is $2\pi/\lambda$, and s and z depend on the distance between the particle and the observer, as well as the scattering angle. The amplitude functions S_1-S_4 are in general functions of the scattering angle and the polarization angle of the incident light, but for spherical particles, both S_4 and S_3 are equal to zero. Moreover, S_1 and S_2 do not depend on the polarization angle of the incident light. They are expressed as infinite series:

$$S_1(\theta) = \sum_{j=1}^{\infty} \frac{2j+1}{j(j+1)} \left\{ a_j \pi_j(\theta) + b_j \tau_j(\theta) \right\} \tag{3.2}$$

$$S_2(\theta) = \sum_{j=1}^{\infty} \frac{2j+1}{j(j+1)} \left\{ b_j \pi_j(\theta) + a_j \tau_j(\theta) \right\} \tag{3.3}$$

For real values of the index of refraction n (pure scattering with no absorption), the complex coefficients a_j and b_j can be determined using the method of phase angles, which involves spherical Bessel functions and their derivatives. Π_j and τ_j are functions that depend on the scattering angle and make use of associated Legendre polynomials and their derivatives. These equations are used to create the logarithmic scattering diagram shown in Figure 3-5 for particle diameters of 10, 100, 500, and 1000 nm. The infinite series in equations 3.2 and 3.3 are approximated by the first 60 terms, and the vertically polarized component of the scattering intensity is calculated for spherical, non-absorbing particles (n = 1.5) in air for a wavelength of 532 nm.

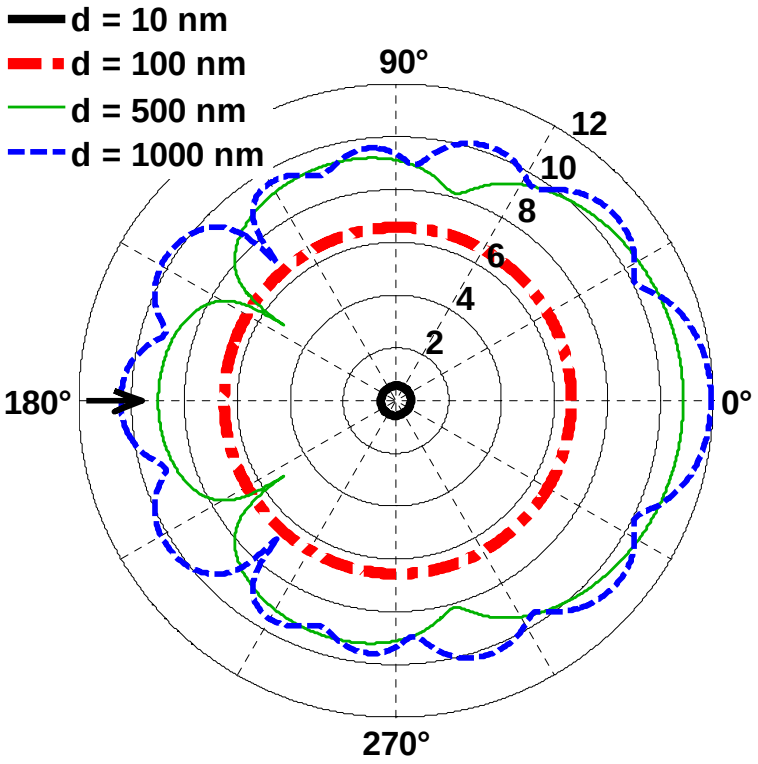

Figure 3-5: Vertically polarized component of scattering intensity for four different particle diameters; logarithmic scaling.

It is apparent that the vertically polarized component is a strong function of particle size, and for larger particles, it can depend very strongly on the scattering angle (the scaling is logarithmic). For particles much smaller than the wavelength of the incident light, the scattering is essentially independent of the scattering angle, as is exemplified by the particle with a diameter of 10 nm. A simpler approach can be taken to approximate the scattering behavior of such small particles.

3.3.1.1. Rayleigh Scattering

When the particle radius is less than approximately 5% of the wavelength of the incident light [103], then the Mie theory can be simplified and is referred to as Rayleigh scattering. Optical measurement of the Rayleigh scattering from soot particles can be used to determine particle sizes in a combustion system.

The alternating electric field surrounding the particle is nearly homogeneous and induces electric dipoles in the particle that vibrate in phase with one another. These create spherical electromagnetic waves; the angular dependence of the scattered light is not dependent on the particle size [104].

The vertically and horizontally polarized scattering intensities are given by [101]:

$$I_{VV}(\theta) = \frac{I_0 \cdot C_{VV}(\theta)}{s^2} \cdot sin^2\varphi \tag{3.4}$$

$$I_{HH}(\theta) = \frac{I_0 \cdot C_{HH}(\theta)}{s^2} \cdot cos^2\varphi \tag{3.5}$$

Where I_0 is the intensity of the incident light and s is the distance between the scattering particle and the observer. C_{VV} and C_{HH} are the vertical and horizontal differential cross sections and in the case of Rayleigh scattering, they are defined as [101]:

$$C_{VV} = \frac{16\pi^4}{\lambda^4} \cdot \left|\frac{m^2-1}{m^2+2}\right|^2 \cdot r^6 \tag{3.6}$$

$$C_{HH}(\theta) = \frac{16\pi^4}{\lambda^4} \cdot \left|\frac{m^2-1}{m^2+2}\right|^2 \cdot r^6 \cdot cos^2\theta \tag{3.7}$$

m is the complex index of refraction of the particle, λ is the wavelength of the incident light in a vacuum, and r is the radius of the particle. These cross sections represent the first term in the series expansion of the full solution defined by Mie theory.

For an ensemble of particles with particle size distribution $p(r)$, the average scattering cross section can be defined as:

$$\overline{C}_{sca} = \int_0^\infty C_{sca} \cdot p(r) dr \tag{3.8}$$

The soot particles studied in this work are assumed to be dominated by coagulation; it can be assumed that the particle size distribution is self-preserving and polydisperse [101]. This is approximated by a lognormal distribution with a median particle radius $\bar{r}_m$ and a standard deviation σ. Now, a scattering coefficient can be defined as the product of the average scattering cross section and the particle number density N_V:

$$K_{sca} = N_V \cdot \overline{C}_{sca} \tag{3.9}$$

Simulation results suggest that the Rayleigh theory begins to underpredict the particle size for particles larger than 10% of the laser wavelength [105], so it is advisable to use the longest laser wavelength possible to enable accurate measurement of a large range of particle sizes. The laser light used for the Rayleigh scattering experiments in this work is vertically polarized ($\varphi = 90°$), and the observer is ideally positioned perpendicular to the incident light ($\theta = 90°$). For these reasons, the detected Rayleigh scattering signal is vertically polarized. The scattering coefficient, which is directly proportional to the measured scattering intensity, is given by:

$$K_{sca} = \frac{16\pi^4}{\lambda^4} \cdot \left| \frac{m^2 - 1}{m^2 + 2} \right|^2 \cdot \bar{r}_m^6 \cdot \mathbf{exp}\left(18\sigma^2\right) \cdot N_V \tag{3.10}$$

Rayleigh scattering measurements suffer from several drawbacks. Mie scattering from liquid fuel droplets or reflected laser light can very easily overwhelm any Rayleigh scattering, thus limiting the maximum possible camera gain and ultimately the measured signal [24, 103]. One possibility to reduce the intensity of the Mie scattering without negatively affecting the Rayleigh scattering signal is to make use of the fact that light scattered in the Rayleigh regime is highly polarized. The ratio of the vertically polarized to the horizontally polarized scattering intensities is shown in Figure 3-6 for a scattering angle of 90°, an incident light wavelength of 532 nm, and an index of refraction of 1.5 (scattering in air). Beamsteering effects introduced by gradients in optical properties of the in cylinder gases, or photoelastic changes of the quartz glass windows as a result of the cylinder pressure, can affect the shape and polarization of the laser light, thus degrading the reliability of the measurement results [106].

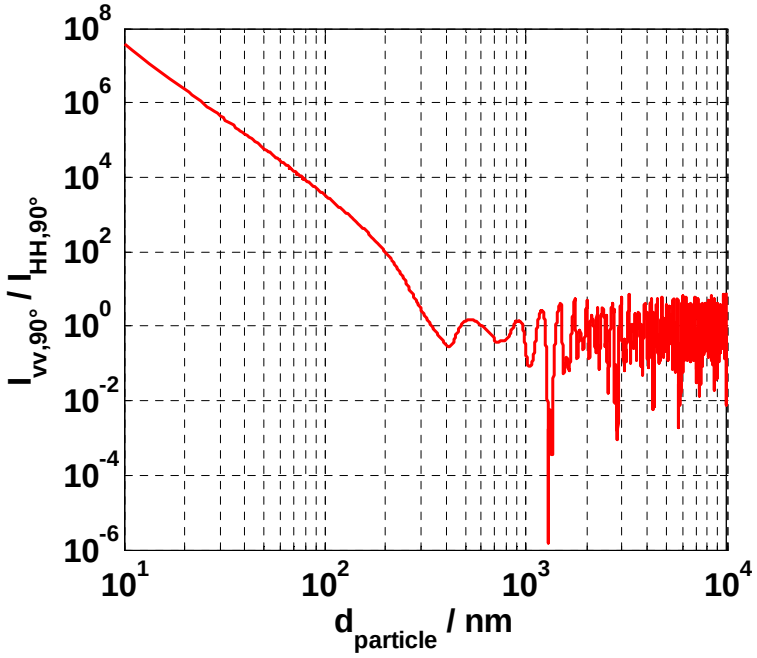

Figure 3-6: Polarization ratio for scattering in air at a scattering angle of 90°; wavelength of incident light: 532 nm

Clearly, unpolarized light that scatters from fuel droplets is much less polarized than a Rayleigh scattering signal. The incident laser light is vertically polarized, so the scattered light likely has a very small horizontal scattering intensity. However, the possibility exists

through multiple scattering and reflections that horizontal components could be present, so in this work, a polarization filter is placed in front of the Rayleigh camera in order to block out any horizontally polarized light. The vertically polarized Rayleigh signal is unaffected. Soot radiation can also interfere with the Rayleigh signal and for this reason, the Rayleigh images are observed through a relatively narrow bandpass filter with a center wavelength of 532 nm. Fluorescence from polyaromatic hydrocarbons (PAH) can also interfere with the Rayleigh signal, but this phenomenon seems to be significantly weaker than Rayleigh scattering for conventional Diesel combustion [105, 107].

The Beer-Lambert law for the absorption of light in a given medium can be expressed as [104]:

$$-dI = K_{ext} \cdot I \cdot dx \tag{3.11}$$

where I is the intensity of light, K_{ext} is the extinction coefficient and a function of position x. This can be integrated over x to obtain the equation:

$$\ln\left(I_0 / I_L\right) = \int_0^L K_{ext}(x) \cdot dx \tag{3.12}$$

Knowledge of the laser intensity before and after the flame can be obtained by an extinction measurement, which is described in the section 3.3.3: RAYLIX.

3.3.2. Laser-Induced Incandescence

Laser-induced incandescence (LII) describes the heating of soot particles via intense laser light to the point of vaporization, at which point the radiation given off by the particles is much more intense than the combustion luminosity. The first experiments involving laser heating of aerosols were published in 1974 [108], and Eckbreth identified LII as a significant interference source for laser Raman scattering diagnostics [109]. Melton and Dasch performed numerical analyses of LII and Melton identified its utility in providing soot volume fraction information [110, 111]. Their work provides detailed information regarding the physics governing the heating of such a particle; the physics are presented here in a simplified form. A first-law energy balance for a particle being heated by a laser is given by:

$$m_p c_p \frac{dT_p}{dt} = \dot{q}_{laser} - \dot{q}_{rad} - \dot{q}_{cond} + \dot{q}_{vap}\,, \tag{3.13}$$

where:

m_p is the soot particle mass

c_p is the specific heat of the soot

T_p is the temperature of the soot particle, which is assumed to be spatially uniform [111]

$\dot{q}_{laser}$ represents the absorbed laser power

$\dot{q}_{rad}$ is the rate of radiative energy loss from the particle

$\dot{q}_{cond}$ is the rate of energy conducted into the gas surrounding the particle

$\dot{q}_{vap}$ is the rate of energy loss due to particle vaporization

The radiative heat loss is proportional to the particle volume since the thermal radiation has wavelengths much longer than the Rayleigh limit [111]. However, this term is expected to be significant at temperatures above 10000 K and is therefore negligible [110]. Energy conduction is the primary means of energy dissipation for particle temperatures of less than approximately 3300 K, and above 3700 K the vaporization of the particle dissipates large amounts of energy [110]. The absorption of laser light scales with the absorption coefficient, which for a particle in the Rayleigh regime is proportional to the particle volume. A particle with a radius of 20 nm and an initial temperature of approximately 2000 K is calculated to heat up to nearly 4300 K within approximately 10 ns for a triangular laser pulse with a maximum power density of $1x10^8$ W/cm² and a pulse duration of 20 ns [110]. As a result of the vaporization, the particle does decrease in size, and it has been theorized that a physical or chemical change takes place in the particle as a result of the heating [112]. The intensity of the LII signal has been observed to correlate well with the particle volume fraction [110], although some researchers suggest that it is proportional to $d^{3.22-3.38}$, but still consider this approximately proportional to the volume fraction [113].

Of importance when performing LII measurements is the wavelength of light that is to be imaged. At shorter wavelengths, the LII signal is not very strong, but it is much stronger than the conventional soot radiation that is emitted from surrounding soot particles during the combustion. This is because the wavelength of peak radiation emission shifts towards shorter wavelengths at higher temperatures; this phenomenon is known as Wien's displacement law [114]. The ratio of LII intensity to soot radiation at a temperature of 2000 K is shown in Figure 3-7.

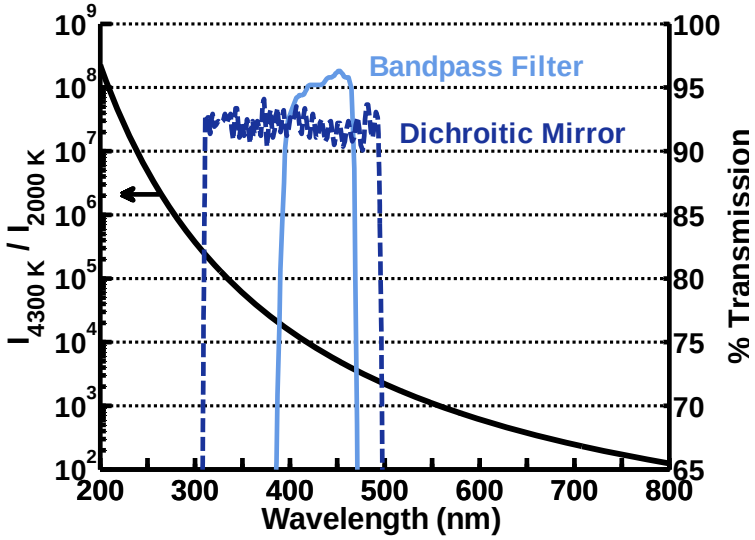

Figure 3-7: Ratio of LII intensity to soot radiation at 2000 K; filter transmission curves for LII measurements

At longer wavelengths, the LII signal becomes stronger, but the combustion radiation does so to a larger extent, so the signal to noise ratio and thus the quality of the measurement is degraded. A commonly used wavelength range is between approximately 400 and 470 nm; it is also selected for this work. Also shown in Figure 3-7 are the transmission curves for the bandpass filter and the dichroitic mirror that are placed in front of the camera. The image-splitting optical relay exhibits poor transmission characteristics below 400 nm, so it is expected that the most significant components of the measured signal have wavelengths

longer than 400 nm. This combination of mirrors and filters effectively blocks reflected laser light, so the setup is not susceptible to the same complications as the elastic scattering measurements.

The excitation wavelength is often chosen to be 532 nm, which is the second harmonic of an Nd:YAG laser. Shorter wavelengths (such as 266 nm) are more effective at heating particles, but also excite polyaromatic hydrocarbon (PAH) molecules, which can fluoresce and interfere with the measurement signal [113]. Recent research indicates that larger PAH molecules that may form during low temperature combustion may fluoresce even with an excitation wavelength of 532 nm; in this case a laser wavelength of 1064 nm may be advisable [107].

During the laser heating process, the particles reach the same temperature regardless of their sizes [110], as long as the laser energy is high enough [113]. It is customary to use laser energy density to describe the amount of energy used to heat the particles, as power density numbers can be deceptive in terms of the total amount of energy delivered to the particles. The typical minimum threshold is on the order of 100-300 mJ/cm². However, the rate of cooling of the particles is size dependent: smaller particles cool faster than larger ones. To avoid biasing the measurement results towards larger particles, Ni et al. recommend using the smallest possible detector gate width (on the order of 10 ns) that begins several nanoseconds after the laser pulse [112]. In practical combustion systems such as Diesel engines, such a short gate width may not give a strong enough signal, so longer gate widths are used and the associated errors due to varying cooling rates are neglected.

3.3.3. RAYLIX

The RAYLIX measurement technique is a 2D laser-based technique used to obtain spatially-resolved information about soot particles such as mean particle radii, particle volume fractions, and particle number densities. It has been applied in laboratory flames [115], in the combustion chamber of a spark ignition engine [116], and in particulate-laden exhaust gases [117, 118]. In this work, it has been applied in the combustion chamber of a Diesel engine. The condensed theoretical description that is included in this section is taken largely from the professorial dissertation from Professor Suntz, who originally developed this technique [101].

In order to perform the RAYLIX measurements in this research engine and view the relevant portions of the combustion chamber, an endoscope with a wide viewing angle is employed. The resulting image must be split and captured by two cameras without loss of observation angle or light, which is not possible with a simple beamsplitter and increased distances between the cameras and the endoscope. For this, a custom image-splitting optical relay comprised of three identical achromatic lenses, each with a focal length of 60 mm, and a dichroitic mirror was designed and built; its functional principle is shown in Figure 3-8. The optical components are housed in a custom-built lens tube system.

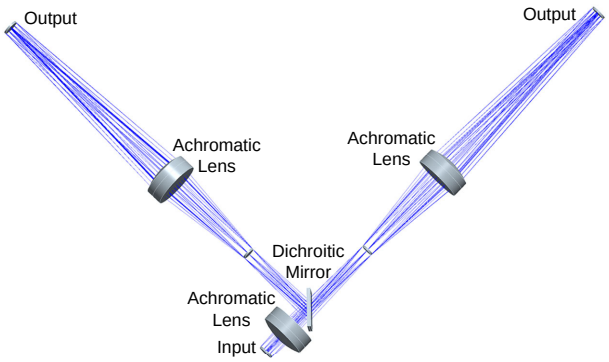

Figure 3-8: Working principle of the image-splitting relay optics used for RAYLIX measurements

The illumination source used for the RAYLIX experiments performed in this work is a double pulsed, Q-switched Nd:YAG laser. For each measurement, two laser pulses are each formed into a thin sheet and passed through the engine at a desired crank angle. The timing of these pulses is shown Figure 3-9, and a model of the experimental setup in the test bench is depicted in Figure 3-10.

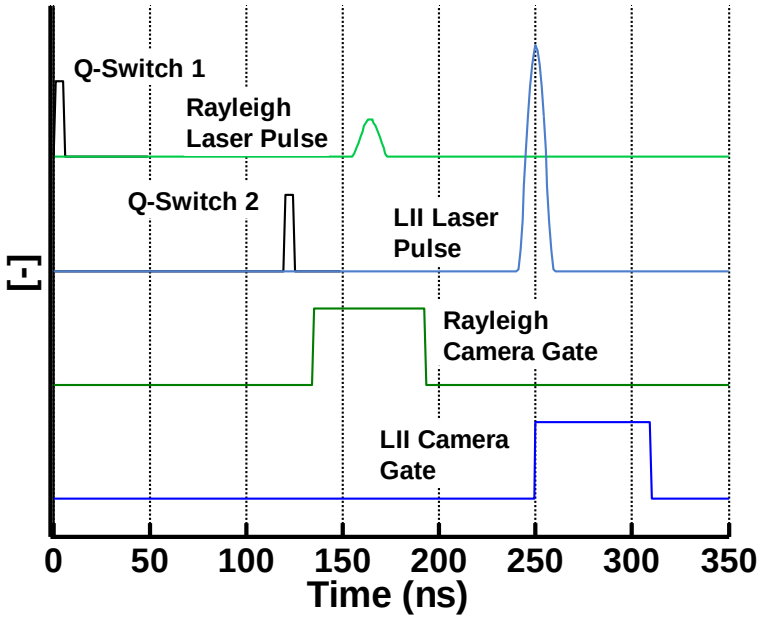

Figure 3-9: Laser and camera timing for RAYLIX measurements

The first pulse is relatively weak; this light is scattered by the very small nascent soot particles and so the scattering is takes place within the Rayleigh regime. The Rayleigh signal is observed with an endoscope passed into the image splitter optics, where it is reflected on a dichroitic mirror at an angle of 90°. It is then passed through a bandpass filter with a center wavelength of 532 nm and a FWHM of 10 nm, followed by a vertically-oriented polarizing filter (see 3.3.1.1: Rayleigh Scattering), before being captured by an ICCD camera with a Samyang 35 mm f/1.4 lens. The Rayleigh camera gate is active for approximately the entire duration of the Rayleigh laser pulse.

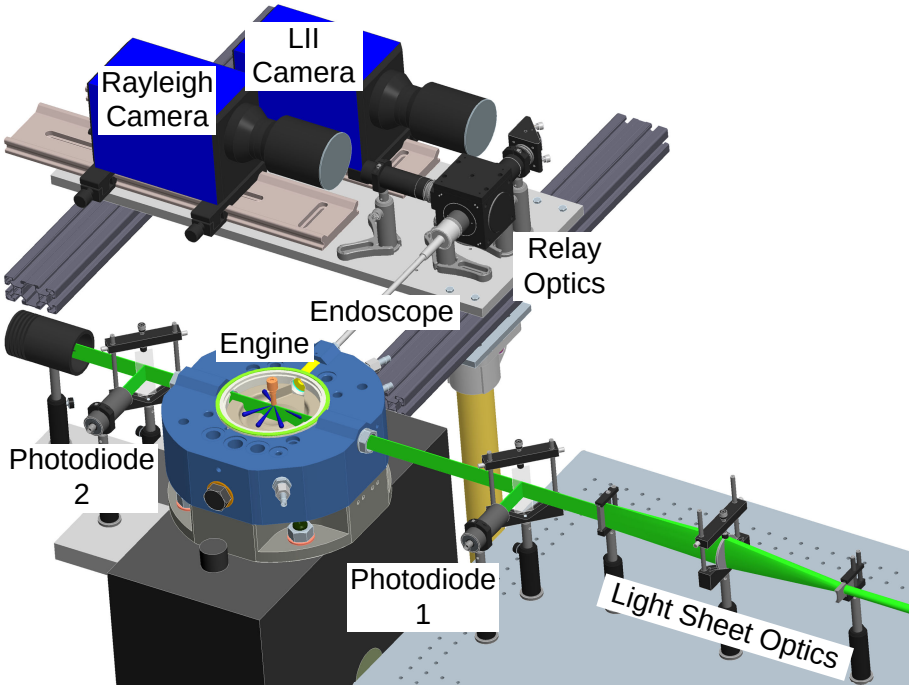

Figure 3-10: Experimental setup for RAYLIX investigations

Approximately 50 ns after the first laser pulse, a second laser pulse is passed through the light sheet optics and into the engine. This one is much stronger than the first pulse with a measured energy density of approximately 210 mJ/cm², this ensures the proper laser heating of the particles required for LII (see 3.3.2: Laser-Induced Incandescence). The LII camera gate is active for 60 ns immediately following the peak of the laser pulse; this ensures an adequate signal at the expense of some measurement accuracy due to the different cooling rates for particles of different sizes.

As shown in Figure 3-10, a portion (approximately 8%) of the laser sheet is split off with a simple glass plate and directed into a photodiode module before the laser sheet enters the engine, where it is converted to a voltage that is measured with a digital oscilloscope. The same is performed after the laser sheet exits the engine. These measurements are taken in both fired and motored operation for every measurement crank angle so that the extinction of the laser sheet due to soot can be evaluated. For this, the integral voltage values of the Rayleigh pulses are compared before and after the engine and between motored and fired operation.

Each RAYLIX measurement consists of two images and one total extinction measurement. The pixel-resolved intensities of the images are referred to as H_{sca} and H_{LII}.

The Rayleigh laser pulse is used for its corresponding scattering image, but is also useful in terms of its extinction caused by the soot particles in the cylinder. It is assumed that absorption contributes to extinction, but scattering only to a negligible extent. The extinction coefficient given by the Rayleigh approximation for a collection of particles is given by [101,102]:

$$K_{ext} = -\frac{8\pi^2}{\lambda} \cdot \mathbf{Im}\left(\frac{m^2-1}{m^2+2}\right) \cdot N_V \cdot \int_0^\infty r^3 \cdot p(r) \cdot dr\,, \tag{3.14}$$

where:

m is the complex index of refraction

N_V is the particle number density [m^{-3}]

λ is the wavelength of the light

r is the particle radius

A lognormal particle size distribution with standard deviation σ and median particle radius $\bar{r}_m$ is assumed, so the extinction coefficient becomes [101]:

$$K_{ext} = -\frac{8\pi^2}{\lambda} \cdot \mathbf{Im}\left(\frac{m^2-1}{m^2+2}\right) \cdot N_V \cdot \bar{r}_m^3 \cdot \mathbf{exp}\left(4.5\sigma^2\right) \tag{3.15}$$

The complex index of refraction *m* is calculated according to Chang and Charalampopoulos [119] to be 1.73-0.6i. The particle size distribution *p(r)* is assumed to have a standard deviation σ of 0.34 [120]. A soot volume fraction based on a spherical volume $V = 4/3\pi\, r^3$ can be defined for an observed volume element with N_V particles in it:

$$f_V = {}^{4}\!/_{3}\,\pi \cdot N_V \cdot \int_0^\infty r^3 \cdot p(r) \cdot dr \tag{3.16}$$

Now, the volume fraction can be expressed in terms of the extinction coefficient:

$$f_V = -\frac{K_{ext}}{\frac{6\pi}{\lambda} \cdot \mathbf{Im}\left(\frac{m^2-1}{m^2+2}\right)} \tag{3.17}$$

However, the local soot volume fractions in a diffusion flame are different according to their position. A total extinction measurement made before and after the flame only provides an integrated soot volume. For this reason, LII is used to determine local volume fractions, not Rayleigh scattering. H_{LII} is assumed to be directly proportional to the soot volume fraction f_V (see 3.3.2: Laser-Induced Incandescence), but the raw signal only provides relative values, not absolute volume fractions. So, the extinction measurement is used to calibrate the LII signal. H_{LII} is averaged over the measurement volume and is assumed to be proportional to the soot volume fraction shown above:

$$\bar{H}_{LII} = {}^{f_V}\!/_{\alpha_{LII}} \tag{3.18}$$

The extinction measurements are used with equation 3.12 and the integral value of the soot volume fraction to determine the calibration factor α_{LII}. Once this factor has been determined, it can be used to directly infer the local volume fractions from the measured LII signal.

To determine radius and particle number density, the ratio of scattering coefficient to extinction coefficient is calculated:

$$K_{sca} = \frac{16\pi^4}{\lambda^4} \cdot \left| \frac{m^2 - 1}{m^2 + 2} \right|^2 \cdot \bar{r}_m^6 \cdot \mathbf{exp}\left(18\sigma^2\right) \cdot N_V \tag{3.19}$$

$$\bar{r}_m = \sqrt[3]{\frac{-\lambda^3 \cdot \mathbf{Im}\left(\frac{m^2 - 1}{m^2 + 2} \right) \cdot K_{sca}}{2\pi^2 \cdot \left| \frac{m^2 - 1}{m^2 + 2} \right|^2 \cdot \mathbf{exp}\left(13.5\sigma^2\right) \cdot K_{ext}}} \tag{3.20}$$

Particle number density is calculated from this expression for median particle radius and the definition of the extinction coefficient:

$$N_V = \frac{{K_{ext}}^2 \cdot exp\left(9\sigma^2\right) \cdot \left| \frac{m^2 - 1}{m^2 + 2} \right|^2}{4\lambda^2 \cdot K_{sca} \cdot \left[Im\left(\frac{m^2 - 1}{m^2 + 2} \right) \right]^2} \tag{3.21}$$

In order to determine K_{sca} from I_{sca}, the measured Rayleigh signal must be calibrated. This calibration takes into account the transmission efficiencies of the various components of the optical setup and the incident laser intensity. Gas is used as the scattering calibration source, because its scattering cross section is known for single molecules at a scattering angle of 90°.

$$K_{sca,ref} = C_{VV}^{Gas} \cdot N_V^{Gas} \approx \frac{4\pi^2 \cdot (n-1)^2}{N_V^{Gas} \cdot \lambda^4}, \tag{3.22}$$

where:

C_{VV}^{Gas} is the differential scattering cross section of the gas

N_V^{Gas} is the particle number density of the gas ($N_V^{Gas} = p/(k_B \cdot T)$)

k_B is the Stefan-Boltzmann constant ($k_B \approx 1.38065 \cdot 10^{-23} J/K$)

T is the absolute temperature in Kelvin

p is the pressure in Pa

n is the index of refraction of the gas

The quotient of $K_{sca,ref}$ and $I_{sca,ref}$ is the calibration factor used to determine K_{sca} from I_{sca}

Finally, K_{ext} can be replaced by the expression for f_V in the expressions for particle size and number density:

$$\bar{r}_m = \sqrt[3]{\frac{\lambda^4 \cdot \frac{I_{sca} \cdot K_{sca,ref}}{I_{sca,ref}}}{12\pi^3 \cdot \left| \frac{m^2 - 1}{m^2 + 2} \right|^2 \cdot \mathbf{exp}\left(13.5\sigma^2\right) \cdot f_V}} \tag{3.23}$$

$$N_V = \frac{f_V{}^2 \cdot exp\left(9\sigma^2\right) \cdot \left|\frac{m^2-1}{m^2+2}\right|^2 \frac{9\pi^2}{\lambda^4}}{\frac{I_{sca} \cdot K_{sca,ref}}{I_{sca,ref}}} \tag{3.24}$$

3.3.4. Two Color Method

3.3.4.1. Theory

Two color pyrometry has long been used to provide information about soot temperatures and concentrations in sooting flames. It is a line of sight method that makes use of soot radiation intensity at two or more wavelengths. For example, Reissing et al. developed the extended two color method that employs measurements at three wavelengths [121]. A very common approach to measuring temperatures and concentrations was developed by Hottel and Broughton in 1932 [122]. This method remains very common in the literature [123, 124, 125, 126, 127, 128, 129], and so it is used in this work to calculate flame temperatures and KL factors.

The spectral emissive power of blackbody radiation depends on the body's temperature and wavelength of emitted light. Planck determined this relationship to be [114]:

$$E_{\lambda,b}(\lambda,T) = \frac{C_1}{\lambda^5\left[exp\left(C_2/(\lambda T)\right)-1\right]} \left[\frac{W}{m^2 \mu m}\right] \tag{3.25}$$

where:

$E_{\lambda,b}(\lambda,T)$ is the spectral emissive power

C_1 is the first radiation constant, equal to $2\pi hc_o$, where h is the Planck constant and c_o is the speed of light in a vacuum

C_2 is the second radiation constant, equal to hc_o/k_b, where k is the Boltzmann constant

λ is the wavelength in μm

T is the blackbody's absolute temperature in K

Blackbody spectral emissive powers are plotted in Figure 3-11 as a function of wavelength for several temperatures.

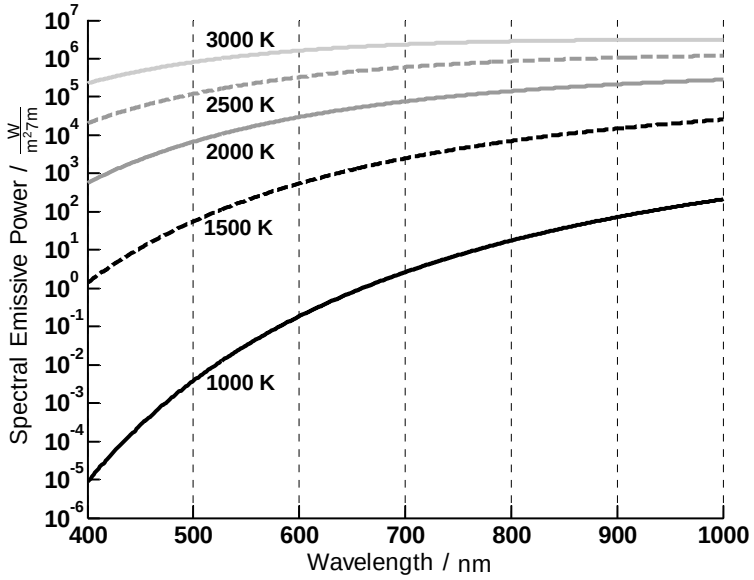

Figure 3-11: Blackbody spectral emissive powers as a function of wavelength with temperature as a parameter

It is clear that for a given wavelength, the emissive power increases strongly with an increase in temperature. The spacing between the curves is larger for the visible part of the spectrum (between approximately 380 nm and 740 nm), which suggests that emissive powers measured at visible wavelengths will react more sensitively to changes in temperature than ones measured in the infrared portion of the spectrum, where the curves are closer together.

Individual soot particles and thick, uniform soot clouds behave as blackbodies, but the radiative behavior of soot clouds that are less thick deviates from that of a blackbody [125]. The emissivity of the soot cloud describes this deviation:

$$E_\lambda(\lambda,T) = \varepsilon_\lambda E_{\lambda,b}(\lambda,T), \tag{3.26}$$

where:

$E_\lambda(\lambda,T)$ is the spectral emissive power of a gray body

ε_λ is the monochromatic emissivity

Alternatively, the apparent temperature T_a can be used to describe the behavior of a non-blackbody radiator. The apparent temperature is the temperature of a blackbody that emits the same amount of radiation as the body at its real temperature T:

$$E_{\lambda,b}(\lambda,T_a) = E_\lambda(\lambda,T) \tag{3.27}$$

The apparent temperature can be expressed as:

$$T_a = \frac{C_2}{\lambda \ln\left(\frac{C_1}{E_{\lambda,b}\lambda^5}+1\right)} \tag{3.28}$$

There are many approaches to modeling the monochromatic emissivity; Hottel and Broughton have developed the following correlation [122]:

$$\varepsilon_\lambda = 1 - exp\left(- KL \Big/ \lambda^\alpha \right), \tag{3.29}$$

where:

K is an absorption coefficient and proportional to the particle number density [113] or the volume fraction [129]

L is the thickness of the flame along the observation axis

α is an empirical parameter

Li and Wallace review a body of research that involves the calculation of absorption coefficients of soot clouds by solving the wave equation. They demonstrate that the dependence of monochromatic emissivity on $1/\lambda^\alpha$ is a very good approximation to the more complex solution, with a value of α of 1.38 [129]. Zhao and Ladommatos point out that for visible wavelengths, the choice of α is relatively unimportant, as the calculated temperature is not particularly sensitive to the value of α. They recommend a value of 1.39 for visible wavelengths, which is the value used in this work [113].

The combination of equations 3.25, 3.26, 3.27, 3.28, and 3.29 leads to the following equation for KL:

$$KL = -\lambda^\alpha \, ln\left(1 - \frac{exp\left(C_2 \,/\left(\lambda T\right)\right) - 1}{exp\left(C_2 \,/\left(\lambda T_a\right)\right) - 1} \right) \tag{3.30}$$

Assuming the apparent temperature can be measured and λ is known, KL and T are the only remaining unknowns in this equation. If the apparent temperature is measured at two different wavelengths, λ_1 and λ_2, and it is assumed that KL is the same for both wavelengths, then the following equation can be used to solve for the actual flame temperature:

$$residual = \left| (KL)_1 - (KL)_2 \right| = \left| \begin{array}{r} -\lambda^{\alpha_1} \, ln\left(1 - \dfrac{exp\left(C_2 \,/\left(\lambda_1 T\right)\right) - 1}{exp\left(C_2 \,/\left(\lambda_1 T_{a,1}\right)\right) - 1} \right) + \\ \lambda^{\alpha_2} \, ln\left(1 - \dfrac{exp\left(C_2 \,/\left(\lambda_2 T\right)\right) - 1}{exp\left(C_2 \,/\left(\lambda_2 T_{a,2}\right)\right) - 1} \right) \end{array} \right| \tag{3.31}$$

By finding the temperature at which the value of *residual* is zero or at its local minimum, the equation is solved for the flame temperature. Put simply, this is performed in MATLAB using a two step procedure. The first step involves a simple numerical evaluation of the minimum value of *residual* to localize the correct temperature. The second step invokes the *fminbnd* function, which employs a golden section search and parabolic interpolation. Inserting the calculated temperature into equation 3.30 provides the KL value.

3.3.4.2. Data processing routine

A comprehensive array of highly integrated programs has been developed in MATLAB to transform the raw images taken with the high speed camera into two dimensional arrays of temperature and KL values. An overview of the program is given in Figure 3-12. The first module of the program is used to extract the two images produced by the relay optics and overlay them with one another. The extraction and image transformation are calculated for images of a calibration target and saved in a data file for use with measured images. In a second module, the intensity calibration is performed. This routine makes use of images of the

tungsten ribbon lamp, dark images, calibration data for the ribbon lamp, and, if desired, transmission curves for the filters used for the measurements. The output of the calibration routine is a data file that contains the two calibration constants to be applied to the measurement data. Before the measured data is processed, the binary images are saved in a standardized format; this task is performed with the software module "Image Averaging." This standardized format clearly defines the software interface for different cameras and binary image formats that may be used in the future. This module also computes average images over any desired number of cycles and saves the averaged images in the standardized format. Once the image transformation, calibration, and image averaging are performed, the calculation of temperatures and KL values can begin. These files are the inputs for the "Calculation Routine" module. This module contains the implementation described in subchapter 3.3.4.1: Theory, and allows the user to quickly process measurement images into result files, which are automatically saved in a standardized format. The last module, "Postprocessing," reads in the result files and is used to produce a variety of spatial and temporal profiles of temperature, blackbody temperature, KL1, KL2, etc., as well as to save result images and videos.

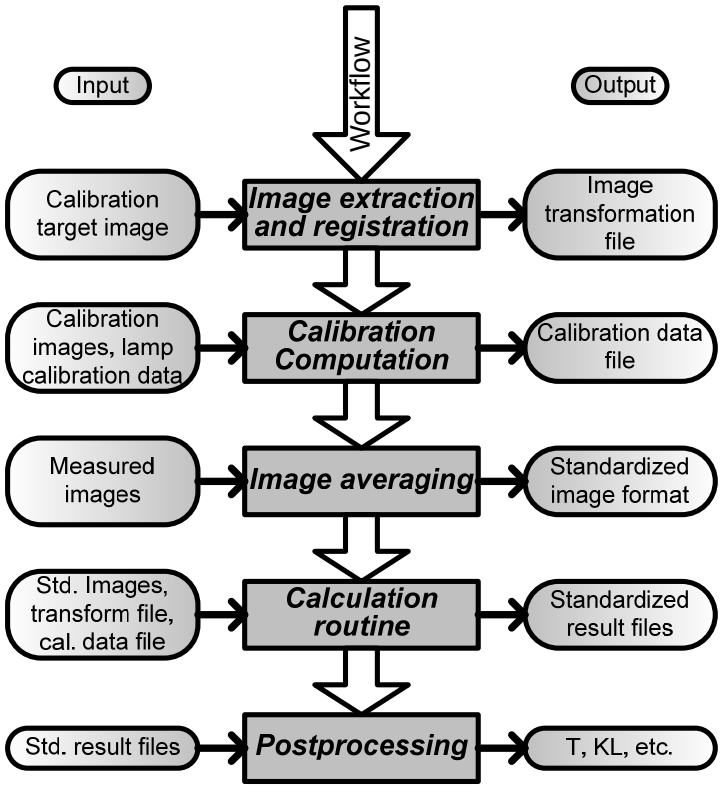

Figure 3-12: Overview of data processing software for two color method measurements

3.3.4.3. Optical system

A typical experimental setup for two color pyrometry can be implemented either with a fiber optic probe mounted in the cylinder [126] or as an imaging system. These imaging systems may make use of an RGB camera, as in [130], a double camera system as in [131], or a single camera [125]. In this work, an endoscopic imaging system is developed to enable measurements with a high speed CMOS camera. A sketch of this image-splitting optical relay is shown in Figure 3-13.

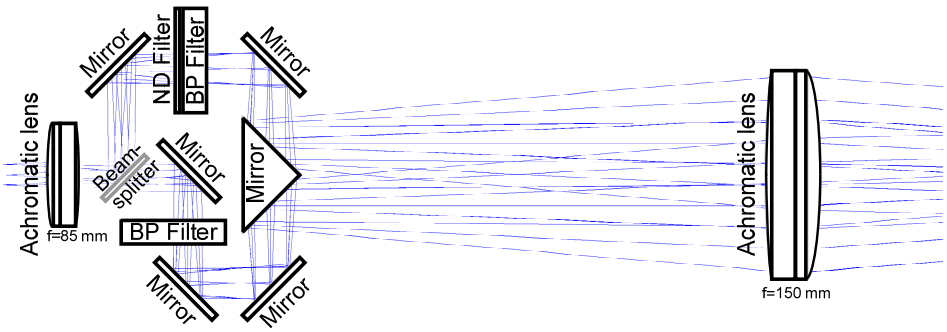

Figure 3-13: Sketch of image-splitting optical relay used for two color method experiments

The fiber optic endoscope from the manufacturer Schölly is mounted at the left side, in front of the smaller achromatic lens. It has an observation angle of 80° and a resolution of 10000 pixels. The light from the endoscope is passed through the beam splitter and through two separate optical paths, each with a different filter. The paths are then made parallel to one another and passed through a second, larger achromatic lens. The images produced by this lens are captured by a Samyang 35mm f/1.4 lens and imaged by the CMOS camera. In this way, the image ordinarily taken through the endoscope is doubled and each resulting image has been passed through its respective filter.

Center wavelengths of 550 nm and 700 nm have been chosen for the filters used here for several reasons. First, the relay optics have been optimized for visible light. At longer wavelengths, chromatic aberrations will adversely affect the image quality. Also, the sensitivity of the CMOS camera decreases at longer wavelengths, which likely decreases the signal to noise ratio. Second, the choice of α is much clearer for visible wavelengths, so temperatures can be determined with more certainty. In addition, it is desirable to have the two center wavelengths as far apart from each other as possible. Finally, the spectral emissive power is more strongly dependent on temperature in the visible wavelength range (see Figure 3-11), so the sensitivity of the system is expected to be higher for visible light than for infrared light. The selection of the filters results from the combination of these constraints and desirable qualities.

Simulations of this optical system have been performed to facilitate the selection of the filters. Spectral transmission and/or reflection curves for each optical component (where available), including the filters, along with the spectral sensitivity of the CMOS camera chip, are integrated for each optical path. The results are multiplied with the spectral emissive power at the corresponding wavelength for a blackbody at temperatures between 1750 K and 3000 K. The result of this simulation for the optimized case is shown in Figure 3-14.

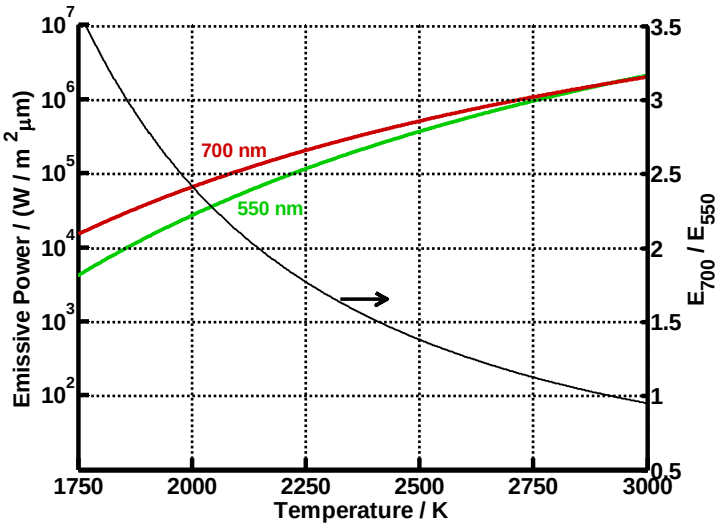

Figure 3-14: Simulated transmitted emissive powers for wavelengths of 550 and 750 nm

The filters have been chosen to keep the ratio of emissive powers, shown by the thin black curve, as close to unity as possible for the expected range of measured flame temperatures. This ensures that the dynamic range of the camera can be used to its fullest extent. Bandpass filters, each with a FWHM of 40 nm, are chosen for the simulation. In order to attenuate the 700 nm signal further (it is stronger than the 550 nm signal, see Figure 3-11), a neutral density filter with an optical density of 0.5 is included in the 700 nm path. For temperatures of 2150 K and above, the expected ratio of blackbody emissive powers is less than 2.

3.3.4.4. Calibration

Before temperatures and KL values can be measured with the two color pyrometry system, the relationship between the incident radiative power and the measured intensity must be established. This is achieved by taking images of a source of known spectral emissive power, in this case in the form of a calibrated OSRAM WI17/G tungsten ribbon lamp. The lamp is positioned in front of the tip of the endoscope at a distance that corresponds to the distance between the endoscope tip and the midplane of the cylinder. A carefully controlled current is applied to the lamp, so that its spectral emissive power is as close as possible to the calibration curve. After the lamp current has stabilized, images are taken through the image-splitting optics with all filters in place. One calibration coefficient is calculated from each of the recorded lamp images and applied to the corresponding measurements to convert image intensities to the appropriate emissive powers. The theory of this calibration method is described here.

The exchange of radiation between two differential surfaces is depicted in Figure 3-15. The differential surface at the left is the emitter (dA_i), and the one on the right is the detector (dA_j). The angles ε_i and ε_j are measured between the line connecting the midpoints of the two differential areas and the appropriate surface normals. The solid angle $d\omega$ is also defined in general terms. The projections of each differential surface with normal vectors parallel to the line connecting the midpoints are also shown. These are defined by the product of the differential areas dA_i and dA_j and the cosines of ε_i and ε_j, respectively.

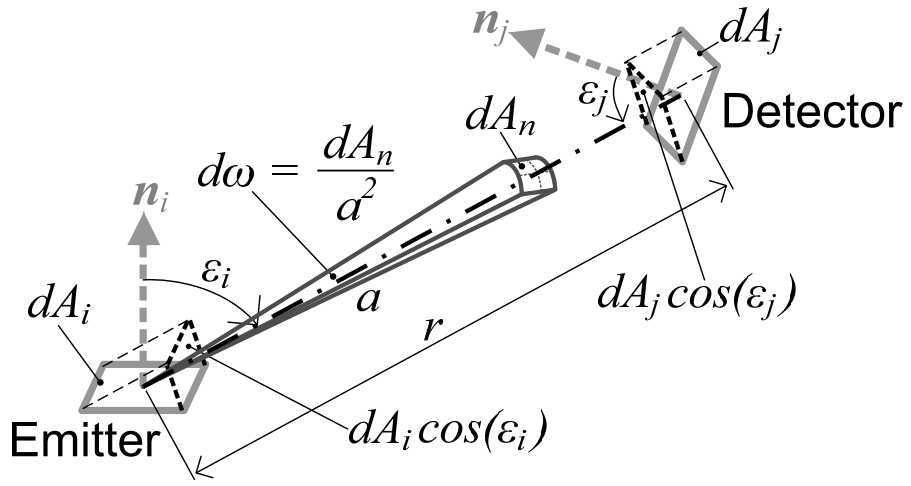

Figure 3-15: Definitions of solid angle, differential areas, and projected differential areas

The solid angle between the emitter and the detector is then given by:

$$\Omega = \frac{dA_j \cos(\varepsilon_j)}{r^2}\Omega_0 , \tag{3.32}$$

where Ω_0 is 1 sr.

For the current discussion, it is assumed that the emitter is the lamp and the detector is the front of the frontmost lens in the endoscope. The spectral power that is emitted by the lamp and received by the detector is then given by [114]:

$$\dot{Q}_{\lambda,det} = \frac{I_{\lambda,lamp} dA_{lamp} dA_{det} \cos(\varepsilon_i)\cos(\varepsilon_j)\Omega_0}{r^2}\left[\frac{W}{nm}\right], \tag{3.33}$$

where I_{lamp} is the lamp's calibrated spectral intensity in W/m^2·µm·sr, evaluated at the desired wavelength, either via a constant value or through averaging over the passband of the corresponding bandpass filter by numerical integration.

In the case that the detector measures radiation from a sooting flame, the spectral power can be computed as follows:

$$\dot{Q}_{\lambda,det,flame} = \frac{I_{\lambda,flame} dA_{flame} dA_{det} \cos(\varepsilon_{i,flame})\cos(\varepsilon_{j,flame})\Omega_0}{r_{flame}^2} , \tag{3.34}$$

It is assumed that the camera intensity is directly proportional to the incident spectral power, and that the filters used for calibration are the same as the ones used for the measurement of the flame. Under this assumption, the following relationship can be established:

$$\frac{\dot{Q}_{\lambda,det}}{H_{lamp} - H_{lamp,0}} = \frac{\dot{Q}_{\lambda,det,flame}}{H_{flame} - H_{flame,0}} , \tag{3.35}$$

where $H_{...}$ represents the measured intensity for a given pixel.

$H_{lamp,0}$ *and* $H_{flame,0}$ represent the measured background intensities, taken either as a dark image or a representative averaged value from a dark portion of the image. If the exposure duration

for the calibration is different than for that of the measurement, then the term $(H_{lamp} - H_{lamp,0})$ must be scaled so that both intensities are associated with the same effective exposure duration.

In the case of the calibration, the angles ε_i and ε_j are negligibly small, so their cosines are taken to be unity. The differential detector area dA_{det} is the same for the calibration and for the measurement. It is not possible to know the exact value of dA_{flame}, but since the calibration is performed at the position corresponding to the midplane of the cylinder, it is assumed that dA_{flame} is equal to dA_{lamp}. Similarly, the value of r_{flame} is unknown as it likely varies temporally and spatially. It is taken to be equal to r, so the measurement accuracy is expected to be best in the cylinder's midplane. Finally, it is assumed that the radiation leaving the soot cloud towards the endoscope travels parallel to the apparent surface normal of the cloud, and that the surface normal of the endoscope's frontmost lens is nearly parallel to this radiation. Under this assumption, the angles $\varepsilon_{i,flame}$ and $\varepsilon_{j,flame}$ are both taken to be zero. With these simplifications and equations 3.33, 3.34, and 3.35, the following equation is derived:

$$I_{\lambda,flame} = (H_{flame} - H_{flame,0}) \frac{I_{\lambda,lamp}}{H_{lamp} - H_{lamp,0}} = f_{cal}(H_{flame} - H_{flame,0}) \qquad (3.36)$$

f_{cal} is computed once for each of the two filtered calibration images and saved in a calibration data file, whereas H_{flame} represents the intensity of a given pixel for one of two measurement images. The calculation of measured flame temperatures takes place on a pixel-by-pixel basis.

3.3.4.5. Uncertainty analysis

Before implementing the imaging system and data processing routine, it is important to understand the errors and sources of uncertainty involved. These include:

- Uncertainties introduced by Hottel and Broughton's correlation for monochromatic emissivity and the selection of α: These have been treated in other researchers' work [132,113] and will not be addressed here.
- Uncertainties caused by spatial variations in the measured intensity of the calibration lamp and/or errors in the measured voltage. Currently available resources do not provide a possibility to quantify such errors.
- Uncertainties introduced by alignment errors between the two images. These cannot currently be quantified.
- The uncertainties introduced by real filters with finite bandwidths. These have been simulated and the results of these simulations are discussed below.
- The effects of window fouling on subsequent measurements. A procedure to correct for window fouling has been developed and is described below.
- Uncertainties introduced by the three dimensional nature of the flame. The calibration is performed at a fixed distance that represents the midplane of the cylinder, whereas the exact distance between the flame and the endoscope tip is not known. Further measurements have been performed with the calibration lamp to quantify these uncertainties; this is discussed below.

The same simulation tool that was used to aid in the filter selection has been employed to investigate the effects of varying filter bandwidths on uncertainties in temperatures and KL factors. First, a matrix of "real" flame temperatures and "real" KL values was created. For each combination of temperature and KL in the matrix, the spectral emissive power is

computed. Then, the combination of transmission / reflectance curves, along with the camera sensitivity, are multiplied with one another for each of the two optical paths. The resulting transmission curves are used to create weighted average emissive powers for each of the two center wavelengths by solving equation 3.31. These averaged emissive powers are then used to estimate the flame temperature and KL factors. This process is repeated for three different filter combinations: perfect filters in which only the emissive power at the central wavelength is passed; filters with FWHM values of 10 nm; and filters with FWHM values of 40 nm. The deviations, or errors in measured flame temperature from the true flame temperature are shown in Figure 3-16. The temperature deviations in the case of the perfect filter are less than 0.02%, so they are not shown.

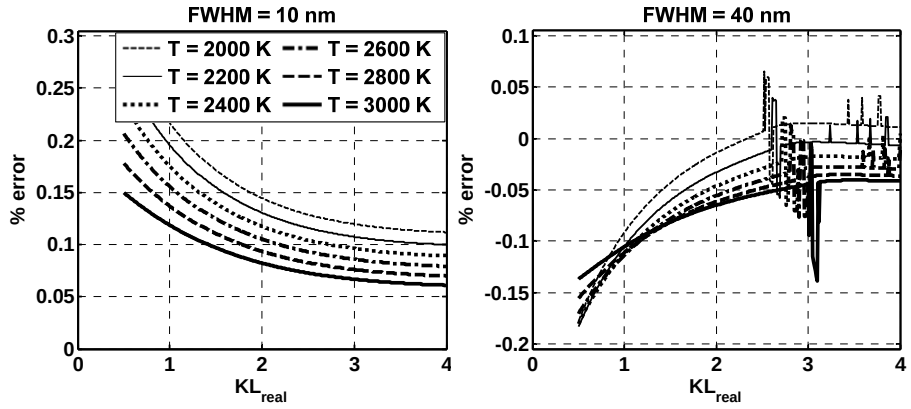

Figure 3-16: Simulated deviations in measured temperatures for two different filter combinations. Left: FWHM = 10 nm; right: FWHM = 40 nm

Contrary to what might be expected with the use of broader bandpass filters, the uncertainty in the temperature measurements is not larger than it is with the narrower filters. In fact, it may even improve slightly. The discontinuities found on the diagram on the right result from numerical instabilities for some combinations of temperature and KL, but do not represent a significant error in temperature calculation. For the filters used in this work, the uncertainty due to the passband of the filters is expected to be less than 6 K for all of the conditions that are to be measured.

An examination of the effects of filter passband width on the uncertainties in determining the KL factor reveals much different trends; this is shown in Figure 3-17. At the left, the results for the case with perfect filters is shown; in the middle are the results for the simulation with filter widths of 10 nm; and at the right are the uncertainties with filter widths of 40 nm.

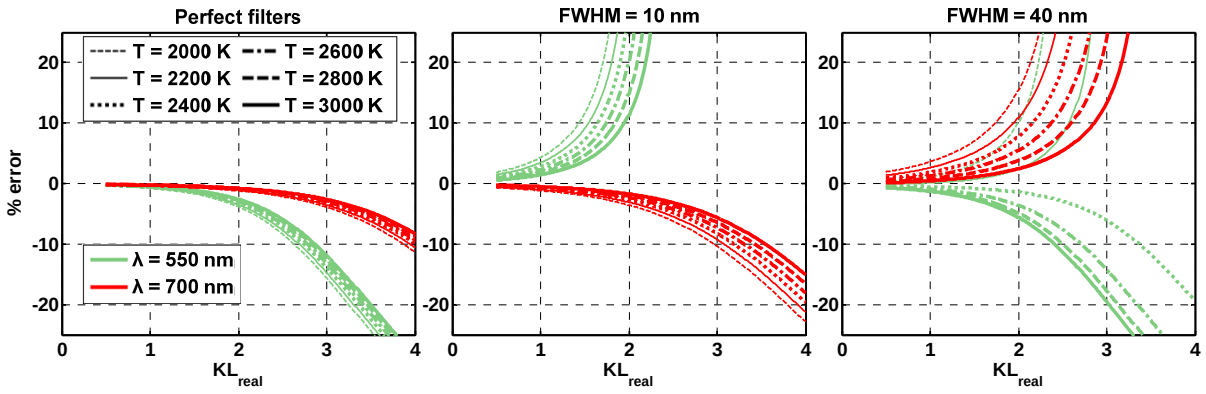

Figure 3-17: Simulated deviations in measured KL values for three different filter combinations. Left: perfect filters; middle: FWHM = 10 nm; right: FWHM = 40 nm

Even with perfect filters, the slightest deviations in system transmission at the filters' center wavelengths create uncertainty in the KL factor. The error in KL is much smaller for the longer center wavelength of 700 nm. For dense soot clouds with KL values of up to 3, these uncertainties can exceed 10%. The temperature dependence of these uncertainties is comparatively small. With a FWHM value of 10 nm, the uncertainties are much larger, particularly for a center wavelength of 550 nm. The uncertainties at a center wavelength of 700 nm have increased compared to the case with perfect filters, but much less so than for the center wavelength of 550 nm. The temperature dependence of the errors increases with the filter width; this is apparent in the rightmost diagram. With the use of wider filters, the uncertainties become much larger for the center wavelength of 700 nm. For the central wavelength of 550 nm, the deviations do not become larger when changing from 10 nm filters to 40 nm filters. However, the temperature dependence becomes much more complex as the system changes between overprediction and underprediction of the value of KL between 2200 K and 2400 K.

Upon examination of both of the simulation results for the cases with real filters, it becomes apparent that a calibration with a tungsten band lamp at a single temperature is not adequate to characterize the true uncertainties that arise from finite filter passband widths. The expected errors in temperature measurement are not significant, but the uncertainty associated with the KL factors is significant.

As shown in equation 3.31, the computational routine for calculating the temperatures attempts to minimize the difference between $(KL)_1$ and $(KL)_2$. Depending on the temperature and the KL value, this difference may not be close to zero, as is indicated by Figure 3-17. However, a minimum is still found and the resulting calculated flame temperature is correct within the uncertainty shown in Figure 3-16.

In order to evaluate the effect of the distance between the flame and the endoscope tip on the calculated temperature, further experiments were performed with the tungsten ribbon lamp. With the lamp at a constant voltage, the distance between the endoscope and the lamp is systematically varied, and 20 images are taken at each position. The calibration is performed at the position of the cylinder midplane and applied to all of the images at all of the distances. For each image, a region of the lamp is selected and the median temperature within this region is evaluated. For each position, the mean value of these median temperatures is calculated; the results are shown in Figure 3-18. A positive axial distance means that the lamp has been moved further away from the endoscope.

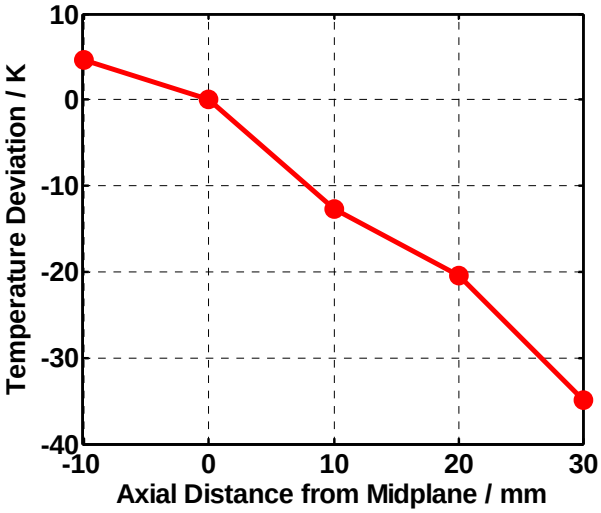

Figure 3-18: Effect of distance between flame and endoscope on the calculated flame temperature

A linear regression of this data yields a slope of approximately 1 K / mm. This relationship is clear for the tungsten ribbon lamp, but in the case of a flame in the combustion chamber, the radiation measured by a given pixel very likely originates from a range of distances from the endoscope tip, as the flame is three dimensional. For this reason, it is believed that the data shown in Figure 3-18 represent the largest possible temperature uncertainty due to the distance between the flame and the endoscope.

If the two-color analyses are restricted to the spray jet that is oriented perpendicular to the endoscope axis (this is the jet shown at the right of Figure 3-2), then the cumulative uncertainties involved with the calculation of the absolute temperature are conservatively estimated to be less than 100 K. The uncertainties with the KL factor are likely much larger and much more difficult to quantify, as they depend on temperature and soot concentration. As a result of the wide filter passbands involved with this work, the temperature dependence is more substantial than it would be with narrower passbands. For this reason, the results for KL are to be viewed critically, particularly for values of KL exceeding unity.

3.3.4.6. Experimental setup and measurement procedures

Before each measurement series, a specially designed calibration target with built-in illumination is inserted into the engine. The two 20W halogen lamps are switched on and a current-controlled power supply maintains a constant current through the lamps. Then, a clean, unused window is installed in the engine, and an image is taken of the calibration target. The unused window is removed and the window to be used for the measurements is installed. An image is taken through this second window, the lamps are switched off, and the calibration target is removed. Aluminum dummies are installed and tightened, and the measurement is carried out (see 3.2: Test Bench). After the measurement series is completed (a series consists of perhaps three or four operating points), the aluminum dummies are removed and the calibration target is reinserted. The lamps are switched on and an image is taken through the fouled window. The fouled window is removed for cleaning and the unused window is reinstalled. Finally, a fourth image is taken through the unused window. This procedure has been developed to minimize the effects of changing lamp intensities with time.

The four images are used to estimate the transmission of the fouled window. Each operating point is assigned a timestamp according to the time at which the images are taken, so that every image associated with the operating point has the same timestamp. A linear interpolation scheme is used to perform a fouling correction for each operating point. This scheme is illustrated qualitatively in Figure 3-19.

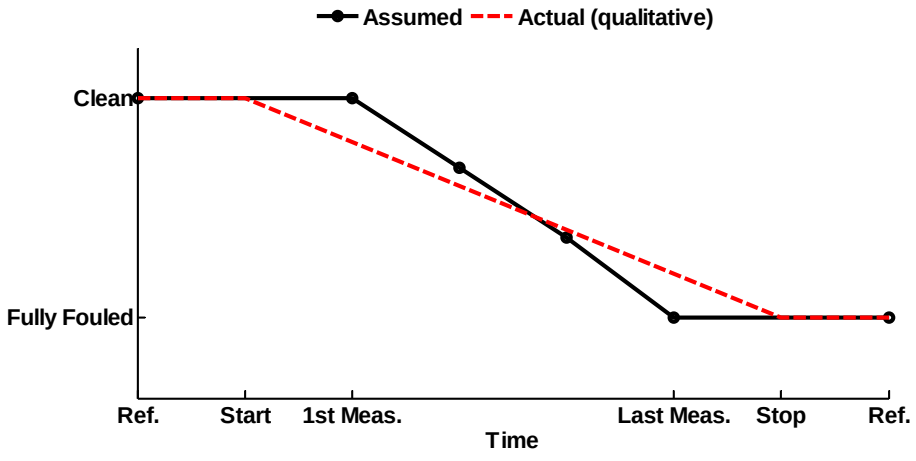

Figure 3-19: Assumed and actual window transmission (qualitative) as they are affected by fouling

Because of uncertainties in the true fouling caused by oil that collects on the window in motored operation, the fouling of the first measurement is not known. Likewise, the time between the last measurement and when the engine stops rotating leads to additional fouling. The approach taken here is integrated into the automated data processing routine and although it could be more accurate, it is used as is for the sake of convenience. In the processing routine, the images are scaled to the "Clean" level before they are used in equation 3.36.

3.3.5. OH Chemiluminescence Visualization

Excited OH radicals (sometimes referred to as OH*) form during the combustion of hydrocarbon fuels in which the mixture is nearly stoichiometric and combustion temperatures are high. These excited radicals give off energy in the form of light as they relax to their ground state. The strongest light given off by this chemiluminescence can be measured in the wavelength range between 300 nm and 310 nm [133]. This chemiluminescence signal is not detected for the early autoignition process as OH radicals do not form in the fuel-rich mixtures in which these first autoignition reactions occur [19]. However, OH chemiluminescence has been observed to occur in the high temperature reaction zone around the fuel jet in a Diesel engine [27], and in the portion of the jet nearest the injector, is the dominant source of light emissions that occurs near 310 nm. The concentration and thus the chemiluminescence intensity of OH is highly temperature dependent. Higgins and Siebers determined that upstream of this location, soot incandescence does indeed contribute to the measured signal at 310 nm [27]. They made use of this information to develop a method of measuring the lift-off length, the distance between the injector tip and the near-stoichiometric diffusion flame as indicated by the imaged OH chemiluminescence signal near 310 nm [28]. This parameter has important implications for the mixing of fuel and air upstream of the combustion zone, and therefore for the ensuing soot formation processes. The measurement technique has been used successfully by others to perform parametric studies, for example in [134, 135].

An advanced imaging technique has been developed to enable OH chemiluminescence imaging in the optically accessible engine with high temporal and spatial resolutions. For this purpose, a new optical access was designed with a large aperture. A sketch of the optical system is shown in Figure 3-20, which depicts the negative transverse magnification of less than unity that results from the given combination and arrangement of double convex lenses. For the dimensions shown in Figure 3-20, the estimated transverse magnification of this system is approximately -0.3; the additional refraction due to the quartz glass window is neglected. This means that the image is inverted and the field of view is more than three times larger than it would be without the lenses.

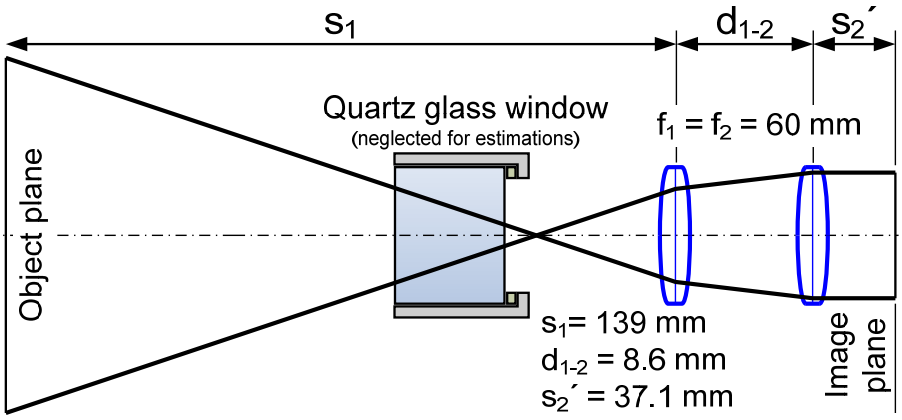

Figure 3-20: Depiction of optical system used for OH chemiluminescence imaging

A CAD image of the implementation of this optical system is shown in Figure 3-21. The quartz glass window is contained within a steel sleeve and sealed on its lateral surface with a high temperature RTV silicone. Axial forces resulting from the pressure within the cylinder are transferred via a polyether ether ketone (PEEK) ring into the back of the steel sleeve, which is in turn held in place by a large hollow bolt. This window design proved much stronger than the previous design, in which no steel sleeve is used. Threaded retainer rings hold the optical elements in place inside of the hollow bolt, which is made with an internal thread. The number and position of optical elements can be freely adjusted to achieve the desired magnification.

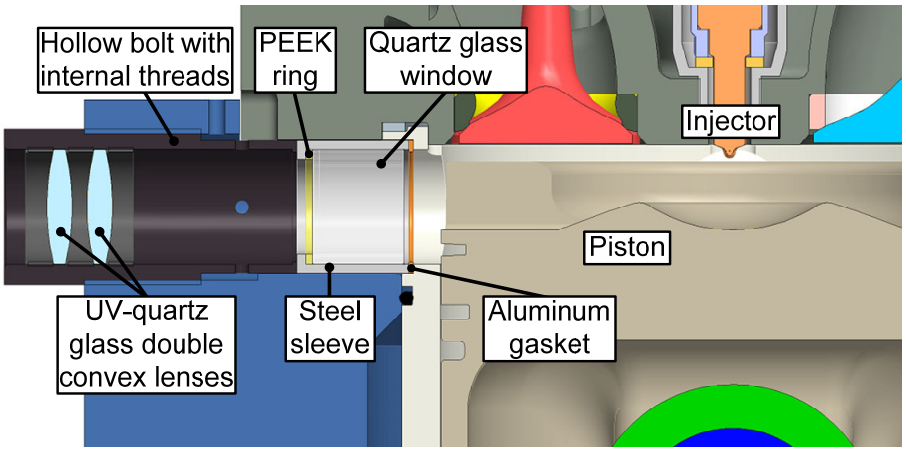

Figure 3-21: CAD cross section of the optical access used for OH chemiluminescence imaging

A sketch of the imaging setup is shown in Figure 3-22, which includes the orientation of the injection jets in the combustion chamber of the engine. Space in the test bench is limited, so the image is reflected on a UV-enhanced aluminium turning mirror mounted on the cylinder housing before being passed through the filter and imaged by the camera. The filter used for these experiments is a combination of a reflection filter and a bandpass filter. As shown in Figure 3-23, the reflection filter passes wavelengths of 310 ± 12 nm and multiples thereof.

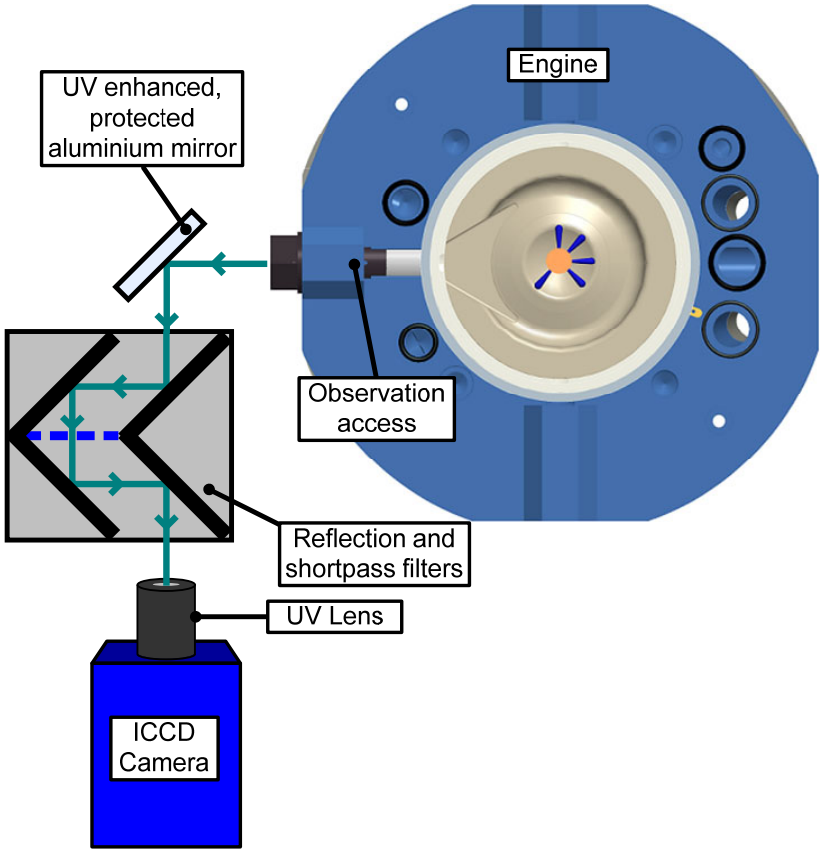

Figure 3-22: Optical setup used for OH chemiluminescence imaging

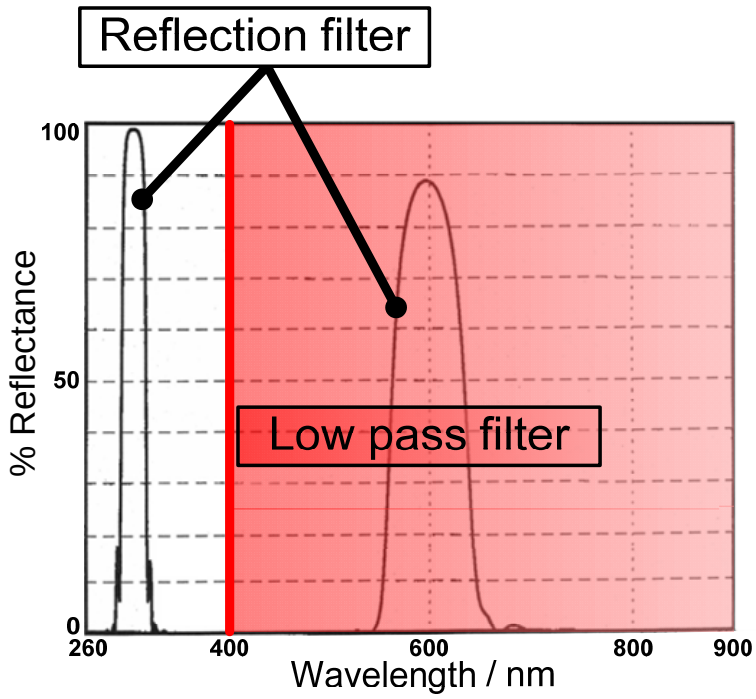

Figure 3-23: Filter transmission curves used for OH chemiluminescence imaging

To image OH chemiluminescence at wavelengths near 310 nm, a short pass filter with a cutoff wavelength of 400 nm is inserted into the reflection filter. This serves to block the visible and infrared components that would otherwise be passed through the reflection filter.

Images are taken through a UV-Nikkor 105 mm f/4.5 lens. With the short pass filter removed from the filter setup, the optics is focused with visible light. When imaging light at 310 nm, the location of the focus will likely be shifted, but because this is a line of sight technique and not a planar, laser assisted technique, the focal shift introduced by the lenses is neglected. An advantage of this Nikkor camera lens is that no additional defocusing is introduced at lower wavelengths, so this should not present further errors in focussing. A LaVision Nanostar ICCD camera is used to take the images. This camera has a pixel resolution of 640x480 and a resolution of 12 bits. The camera is synchronized to the crank angle encoder of the engine via a LaVision programmable timing unit.

3.3.6. Summary of Measurement Techniques

The measurement techniques described in this chapter are summarized in Table 3-3. The phenomena that can be investigated with these techniques, as well as the desired measurement result, the type of illumination, the type of observation (planar or line of sight), the optics used for imaging, the images obtained during the measurement process, and the type of camera used for the work are listed for each measurement technique.

Table 3-3: Summary of measurement techniques developed in this work; where applicable, the configurations employed in the scope of this project are shown in boldface type.

	Mie Scattering	**RAYLIX**	**OH chemiluminescence**	**Two color pyrometric imaging**
Phenomenon to be observed	Fuel injection, vaporization	Soot formation	Fuel / air mixing and combustion processes	Soot formation, nonpremixed rich combustion
Desired result	Liquid fuel penetration depths during the fuel injection event	Soot particle sizes and concentrations; locations of particles in the measurement plane	Location of excited OH radicals; lift-off length, flame structure	Spatially and temporally resolved flame temperatures and soot KL values
Illumination	Planar or **divergent laser beam**, **Nd:YAG laser** or flashlamp	Planar, Nd:YAG laser ($\lambda = 532$ nm)	None	None
Planar / line of sight observation	Line of sight, limited by illumination and soot radiation	Planar	Line of sight	Line of sight
Imaging optics	Endoscope: Ø = 8 mm, observation angle 70°, bandpass filter	Endoscope: Ø = 8 mm, observation angle 70°; image splitting optical relay with dichroic mirror, bandpass filters	Specially developed double-lens system: double-convex UV lenses, L = 60 mm, combination reflection and lowpass filter, UV-Nikkor 105 mm f/4.5 lens	Fiber optic endoscope: observation angle 80°, image splitting optical relay with two bandpass filters and one neutral density filter, Samyang 35 mm f/1.4 lens
Images obtained	Images of scattered / **backscattered** light from liquid fuel droplets ($\lambda = 532$ nm)	Rayleigh scattering image from soot particles ($\lambda = 532$ nm); soot incandescence image ($\sim 400\text{ nm} \leq \lambda \leq \sim 470\text{ nm}$)	Chemiluminescence image ($\lambda \approx 310$ nm)	Natural flame luminosity images: two on one camera chip at two wavelengths ($\lambda_1 = 550$ nm; $\lambda_2 = 700$ nm)
Camera type	CCD	2x ICCD	ICCD	High speed CMOS

4. Results and Discussion

A significant contribution of this work has been devoted to the development of optical measurement techniques in the engine. The results presented are by no means a representation of a complete set of parametric variations, rather a small set of experiments that demonstrate the capabilities of the techniques and provide insight and information to motivate future work. Without any context or understanding of the underlying physical phenomena, this information has little value. Therefore, the discussion in this chapter attempts to explain the observations in the context of Diesel combustion and to provide questions to motivate future research. Where applicable, relevant aspects of the measurement techniques are evaluated.

Two different baseline operating points are considered, from which parametric variations are carried out. One is a naturally aspirated, low load operating point, whereas the other is a boosted part load point. Unless otherwise specified, premium grade Diesel fuel is used for all experiments. Next, data are shown that characterize the standard mid-load point. Results from a rail pressure variation are presented and explained. The observed effects of the pilot injection on the ignition and combustion of the main injection are then summarized. Finally, a comparison between operation with Diesel fuel and with an emulsion of Diesel fuel, ethanol, and water (E10W10) is presented, and the mechanisms responsible for the observed reductions in soot emissions with E10W10 are described. A separate subchapter is devoted to each set of results and each subchapter is divided according to the various measurement techniques that were applied.

4.1. Operating Points

4.1.1. Low Load

In the course of the RAYLIX investigations, it was discovered that measurements were only possible at very low loads. This is attributed to two factors:

- Very high soot concentrations at higher loads quickly absorbed all laser light, thus eliminating the viability of the RAYLIX technique. With Diesel fuel, soot concentrations at low loads were low enough to enable the measurements for a short crank angle window.
- The initial design of the large quartz glass windows proved to be very limited in terms of maximum allowable cylinder pressures. A lower load was necessary to prevent the windows from being destroyed.

This naturally-aspirated low load operating point is summarized in Table 4-1; SOI_I stands for the indicated start of injection, which is the crank angle at which the energizing voltage is first applied to the injector. The fuel injection is divided between a relatively short pilot injection and a main injection. With the original combustion chamber window design, the pilot injection was necessary to decrease pressure gradients and protect the windows.

Table 4-1: Low load engine operating parameters

Engine speed	1175	rpm
Intake pressure	0.1	MPa
Intake temperature	300-310	K
Exhaust pressure	0.11	MPa
Injection pressure	100	MPa
$SOI_{I,\ pilot}$	15	°CA BTDC
Pilot injection duration	280	µs
$SOI_{I,\ main}$	3	°CA BTDC
Main injection duration	520	µs
$IMEP_n$ (diesel)	0.15	MPa
EGR Rate	0 - 30	%

4.1.2. Part Load

Improvements to the quartz glass window design enabled operation with much higher peak cylinder pressures for the OH chemiluminescence investigations and the two color pyrometry measurements. Because the Mie scattering investigations were performed without large windows, higher cylinder pressures were not a problem. For the application of these measurement techniques, it was desirable to examine the quasi-steady phase of the Diesel combustion process, so a boosted, part load operating point was developed with a significantly longer injection duration. As with the low load condition, this operating point is also characterized by a small pilot injection and a main injection. The pilot injection timing was changed for operation with the Diesel ethanol water emulsion; the reasons for this will be explained in a later section. Table 4-2 shows the standard engine operating parameters for this operating point.

Table 4-2: Part load engine operating parameters

Engine speed	1175	rpm
Intake pressure	0.16	MPa
Intake temperature	304-308	K
Exhaust pressure	0.18	MPa
Injection pressure	180	MPa
$SOI_{I,\ pilot}$ (diesel / E10W10)	10 / 13	°CA BTDC
Pilot injection duration	153	µs
$SOI_{I,\ main}$	3	°CA BTDC
Main injection duration (diesel / E10W10)	1570 / 1670	µs
$IMEP_n$ (diesel)	0.61	MPa
EGR Rate	0 - 30	%

4.2. Characterization of the Part Load Operating Point

4.2.1. Cylinder pressure trace

The current design of the engine is such that the cylinder volume is not exactly known for every crank angle. This is because the topmost compression ring loses compression as it passes over the optical access, thus combining additional crevice volume with the cylinder volume. For this reason, a reliable heat release analysis cannot be performed with this engine. Future optimization of the engine design, e.g. by moving the compression ring down or simply removing it, should enable heat release analyses to be performed with this engine.

While a calculated apparent rate of heat release for this engine cannot provide satisfactory insight into the combustion process, the indicated cylinder pressure trace can be used to obtain basic information about the progression of the combustion process. In Figure 4-1, the ensemble-averaged cylinder pressure trace is shown as a thick gray line, and the calculated motored cylinder pressure trace is plotted as a black dotted line.

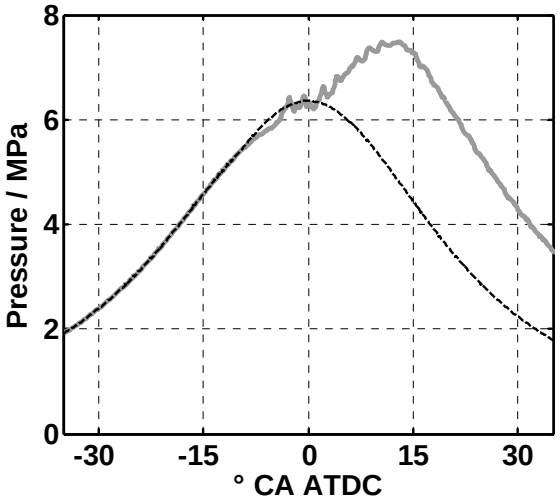

Figure 4-1: Averaged, filtered cylinder pressure trace for the mid load operating point. Gray solid line: fired pressure trace; black dotted line: calculated motored pressure trace.

The first departure of the fired trace from the motored trace shortly after 10 ° CA BTDC is attributed to evaporative cooling effects from the pilot injection and the associated pressure drop. The following rise in fired pressure indicates that the fuel injected during the pilot injection reacts to release energy in the form of heat. The larger hump in the fired pressure trace is attributed to the energy released by fuel injected during the main injection. Closer inspection of the fired pressure trace suggests that the first measurable pressure increase that can be attributed to the combustion of the pilot injection is located between approximately 5 and 6 ° CA BTDC. The apparent start of heat release for the main injection is taken to be the start of the first significant pressure rise after TDC at approximately 1 ° CA ATDC.

4.2.2. Mie scattering

The Mie scattering data provide information about the location of liquid fuel directly downstream of the injector. An example image taken with the backscattering technique employed in this work is shown in Figure 4-2 for a crank angle of 4 ° after the indicated start of injection ($ASOI_I$), which is the crank angle at which current begins to flow through the solenoid in the injector as measured by the indicating system. Also shown in the diagram is a

CAD image of the combustion chamber. The spray jets are numbered 1-5 and the corresponding jets seen in the Mie scattering image are labeled at the top of the figure.

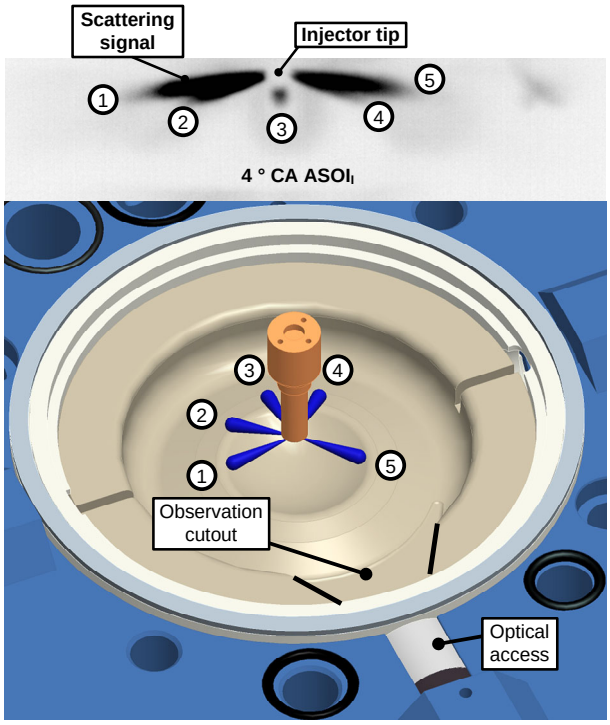

Figure 4-2: Example of Mie scattering image and identification of fuel jets. Standard part load operating point, 4 ° CA ASOI$_I$.

The orientation of the spray jets shown in the figure is typical of the images that can be obtained from the combustion chamber of this engine; it should be noted when viewing all following images. For planar, laser-based investigations, jet number 1 is intersected with the laser and is thus the jet of interest.

The backscattering illumination technique effectively illuminates at least some portion of all of the spray jets. As such, an analysis of the spreading angle of jet number 1 is not possible. It is not known if all of the liquid droplets are captured by this technique, particularly in the region downstream of the apparent tip of the liquid jet. The possibility exists that small concentrations of small droplets would not be imaged with this system due to the small aperture provided by the endoscope. Tests with a larger aperture should provide clarity as to the suitability of this endoscopic measuring system for the measurement of all liquid-phase fuel. However, it is not believed that the true penetration depths are significantly longer than the ones reported here, as the intensity gradients near the tip of the spray are known to be quite large [12]. Despite these uncertainties, a computer-based analysis of the images can provide insight about the liquid fuel penetration depths.

To this end, two different methodologies have been developed. The first method involves computing an ensemble average image of 50 cycles. This image is then thresholded (i.e. made binary) with a threshold value that represents the lowest measured signal intensity that can be differentiated from the background intensity and therefore considered to be measured signal. Pixels in which measured signal is present are given the value of 1; all other pixels have a value of 0. The distance between the injector tip and the pixel with a value of 1 furthest downstream in jet 1 is then taken to be the penetration depth. A second method involves first thresholding the images from individual cycles in a manner similar to the one described

above. These binary images are summed and the resulting image is divided by 50, the number of images. The result is a frequency of occurrence image. Penetration depth is calculated as the distance between the injector tip and the point of 95% occurrence furthest downstream in jet 1. Each of the penetration depths are multiplied by a scaling factor obtained with a calibration target in the midplane of the cylinder (11 pixel / mm) to obtain a measure of length. These procedures are repeated for multiple crank angles; the results are shown in Figure 4-3 for the quasi-steady phase of the combustion process, after the penetration depth has increased from its starting value of 0 mm. The cylinder pressure at the start of injection is approximately 5.6 MPa.

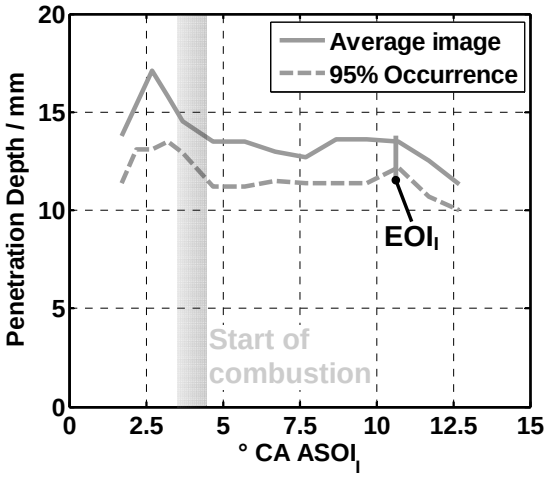

Figure 4-3: Penetration depths for the part load operating point; the start of combustion is indicated by a gray beam

Penetration depths calculated with the 95% frequency of occurrence contour are characteristically shorter than those calculated from the average image. However, both curves exhibit similar behavior. The measured penetration depths reach their maximum near 3 ° CA ASOI$_I$; after this, the penetration depths decrease. Towards the end of the measurable data, a small increase of short duration is observed. It should be noted that the uncertainty in this measurement technique increases as combustion progresses and continuum radiation from the combustion process is intense enough to make a significant contribution to the background radiation, thus increasing uncertainty. Generally, it can be concluded that lift-off lengths for this operating point are measured to be typically between 11 and 15 mm, and the tendency with increasing crank angle is for decreasing penetration depths. This shortening of penetration depths is attributed to the increasing temperatures and pressures within the cylinder, which accelerate the break-up and vaporization processes described in chapter 2. Thus, the penetration depth of the spray is believed to decrease as the combustion progresses. This recession of length, combined with a length recession that is observed (but is not quantifiable due to excessive combustion radiation) at the end of injection will affect the combustion process. An example of these effects will be discussed below with regards to the two color method measurements.

4.2.3. OH Chemiluminescence

The large-aperture optical access described in Chapter 3 made very short exposure durations possible. An example of the measured chemiluminescence signal, averaged over 20 working cycles, is shown in Figure 4-4 for a crank angle of 6 ° CA ASOI$_I$. This is an inverted grayscale representation; darker areas indicate higher signal intensities.

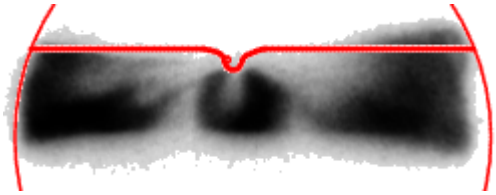

Figure 4-4: OH chemiluminescence image; average of 20 cycles, 10 µs exposure duration; imaged crank angle 6 ° CA $ASOI_I$

As explained in Chapters 2 and 3, this chemiluminescence signal can ideally be used to determine the lift-off length. The suitability of the measured signal for such analyses is evaluated by first choosing a pixel that represents the tip of the injector, and then generating logarithmic radial intensity profiles at various angles around jet 1. The two limiting angles, 0° and 16°, are shown in Figure 4-5.

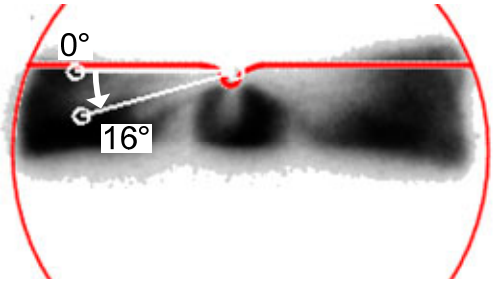

Figure 4-5: Limiting angles for logarithmic intensity profiles

The logarithmic radial intensity profiles are generated every 2° CA and are shown in Figure 4-6 for a crank angle of 6 ° CA ATDC for 5-cycle average images. To create each profile, the image is rotated by the desired angle with a bilinear interpolation scheme, and the pixel intensities are taken from the row containing the injector tip. A scaling in the cylinder's midplane of 4 pixel / mm was determined with a calibration target and applied to the profiles to provide the length units for the radius (r) of mm.

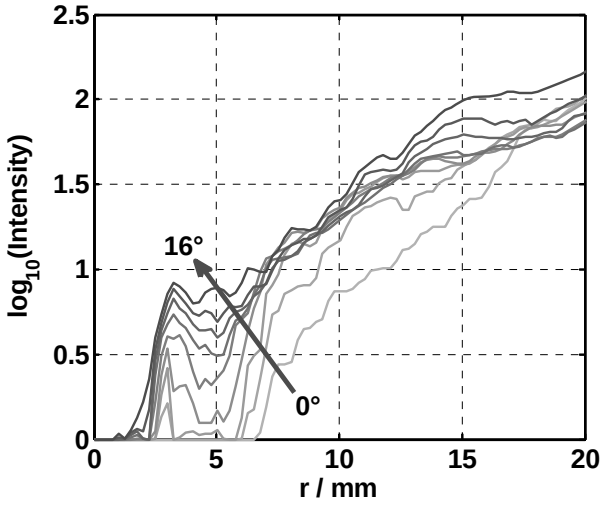

Figure 4-6: Logarithmic radial intensity profiles for a crank angle of 6 ° $ASOI_I$

The very short exposure durations used here mean that intensifier gains are relatively high. At the same time, the gain is adjusted so that no single image contains saturated pixels. This

means that the intensities measured near the injector tip are low and noise degrades image quality. Nonetheless, the characteristic "knee" that has been observed by Higgins and Siebers [27] and others [135] can be seen in some curves. With the engine and injector configuration used here, the intensity profiles at 0° are nearly always lower than those at 16°, which suggests that the lift off lengths near the cylinder head may be longer. Musculus et al. predicted this asymmetry in [134], but the effects of the cylinder head temperature on flame symmetry were shown to be relatively small in [29]. While conclusive evidence of this asymmetry is not presented here, this could be caused by two different effects. First, the cylinder head is cooler than the gas in the cylinder, which tends to cool the region of the cylinder near the head. Lower temperatures lead to longer lift-off lengths. Second, there is likely to be less air available for entrainment near the cylinder head, which would hinder the entrainment process and thus the heating of the fuel. This would also tend to lead to longer lift-off lengths. Future refinements to the experimental apparatus and the measurement techniques should help provide more clarity on this subject.

The analysis here is complicated by the fact that two fuel jets are in the line of sight (jets 1 and 2 as shown in Figure 4-2), and chemiluminescence from jet 3 may also influence intensities measured in the region near the injector. As such, it cannot be stated that the curves shown belong only to the jet in the cylinder midplane. Changing the injector by removing the nozzle hole of jets 2 and 3 would likely have an influence on the flame structure and lift-off length [136]. This is a drawback of the design of this optical engine, but useful information could still be obtained with such a modified injector.

To avoid the sources of error described above as much as possible, a mean of the four logarithmic radial intensity profiles with the smallest angles (0°, 2°, 4°, 6°) is computed and shown in Figure 4-7 for a range of crank angles.

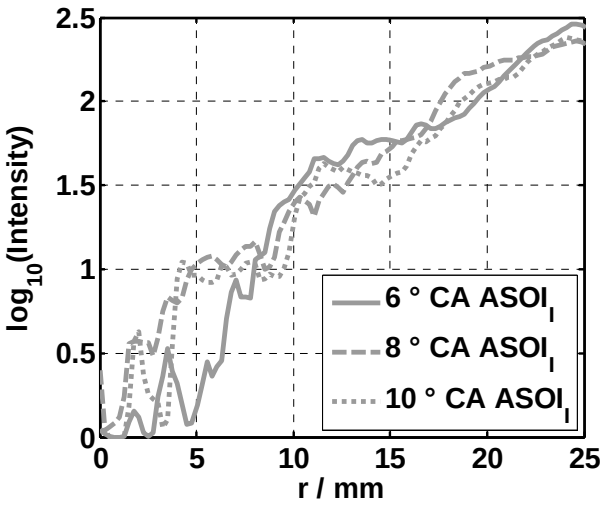

Figure 4-7: Averaged logarithmic radial intensity profiles for the part load operating point at various crank angles

As a result of the averaging technique, the characteristic "knee" is no longer observed in the logarithmic radial intensity profiles. With the pilot injection, the data are not conclusive, but may indicate that the lift-off length contracts as the combustion progresses. Furthermore, it appears that the lift-off lengths for this operating condition are indeed shorter than the liquid penetration depths. This is believed to be a characteristic of Diesel combustion without reduced oxygen concentrations due to EGR.

In order to improve the quality of data, the following changes are suggested for future work:

1. Changes should be made to the injector so that one jet is clearly visible with no interference from the other jets. For the spray pattern shown in Figure 4-2, this could mean removing jets 2 and 3.
2. The field of view provided by these optics is larger than necessary to capture the lift off lengths. A design with a smaller field of view would provide improved spatial resolution.
3. The use of achromatic UV lenses would likely improve image sharpness and spherical aberrations. These may need to be cooled to maintain a safe temperature. This could be realized with slightly smaller lenses and a special cooled adapter. If possible, support from an institute with expertise in optical design could be sought to optimize the design and to include the effects of the quartz glass window on the image quality.
4. To reduce the gain necessary with the ICCD camera, longer exposure durations can be used. An optimum must be found between strong signal intensity and images that are not too adversely affected by motion blur.
5. A more compact filter should be purchased to enable installation of the camera without a mirror. This should help to minimize vibrations that tend to shift the images and make the image processing much more tedious.
6. Only low imaging rates (approximately 0.5 Hz) were possible with the current configuration. This creates a problem for timing sweeps involving several images at each imaged crank angle, as the measurement duration becomes very long. Window fouling becomes significant, and the quality of the results is degraded. This may be improved if a delay generator is used and adjusted by hand, as the programmable timing unit appeared to be the limiting factor.

4.2.4. Two Color Method

The combination of fiber optic endoscope and filters with full widths at half max (FWHM) of 40 nm enables two color pyrometric high-speed imaging at a rate of 10 kHz. At the engine speed of 1175 rpm, this corresponds to a crank angle resolution of approximately 0.7 °. Two methods can be used to calculate flame temperatures and KL values:

1. Images from multiple working cycles (in this case, 20 cycles) are ensemble averaged. Then, temperatures and KL values are calculated for each of the averaged images. This procedure is equivalent to the data averaging procedure discussed by various researchers to reduce calculation time and the mitigate the influence of noise on the data [113, 126, 129]. Images processed in this way are referred to as “data averaged.”
2. Temperature and KL values are calculated for each image of a series of working cycles. These individual cycles can either be presented as such or the results can be averaged, which is equivalent to the result averaging methods described in [113, 126, 129]. Data averaged in this way is referred to as “result averaged.”

Results that have been computed with both of these methods are demonstrated later.

A typical data-averaged flame temperature image is shown in Figure 4-8 for a crank angle of 7.9 ° CA ATDC. The approximate locations of the injector tip and the cylinder head are shown for reference purposes.

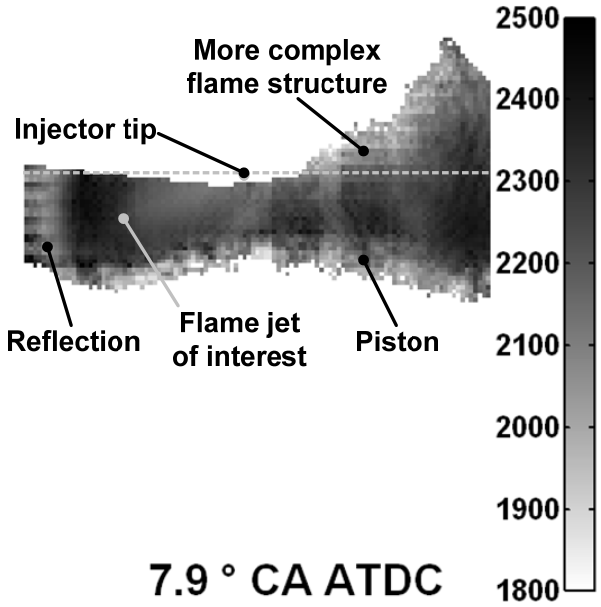

Figure 4-8: Example of a data-averaged flame temperature image, calculated from an ensemble average of 20 working cycles; image at 7.9 °CA ATDC, 10.9 ° CA $ASOI_I$

Inspection of the images, particularly of series of images, reveals regions of the image that do not provide reliable data, either as a result of reflections, because of the nature of the flame structure, or because of excessive camera artifacts. The leftmost region of the image in Figure 4-8 is influenced by reflections on the wall of the piston bowl cut out and by camera artifacts, so these data are not considered reliable. At the bottom of the image, the piston can be seen. Here too, it is believed that the measured signal is altered by reflections, and the results are not taken to be accurate. On the right side of the image, a more complex flame structure is observed. This is because there are two injectors that do not lie in the cylinder's midplane, and the flames from jet 5 (see Figure 4-2) are carried by the swirl flow into the field of view of the camera. Here too, the results should be viewed with some skepticism as to their accuracy. The flame jet of interest, jet 1, can more clearly be seen, but jet 2's influence on the measured temperatures and KL values cannot be discounted as this is a line of sight measurement technique.

Imaging with the high speed camera proves effective at providing temperature and KL information for much of the combustion process. A representative series of these data-averaged temperature and KL images is shown in Figure 4-9 for a range of crank angles. The images have been trimmed so that only the region around jets 1 and 2 (Figure 4-2) is visible. The images in the left column show calculated flame temperatures, and the images in the right column show KL values.

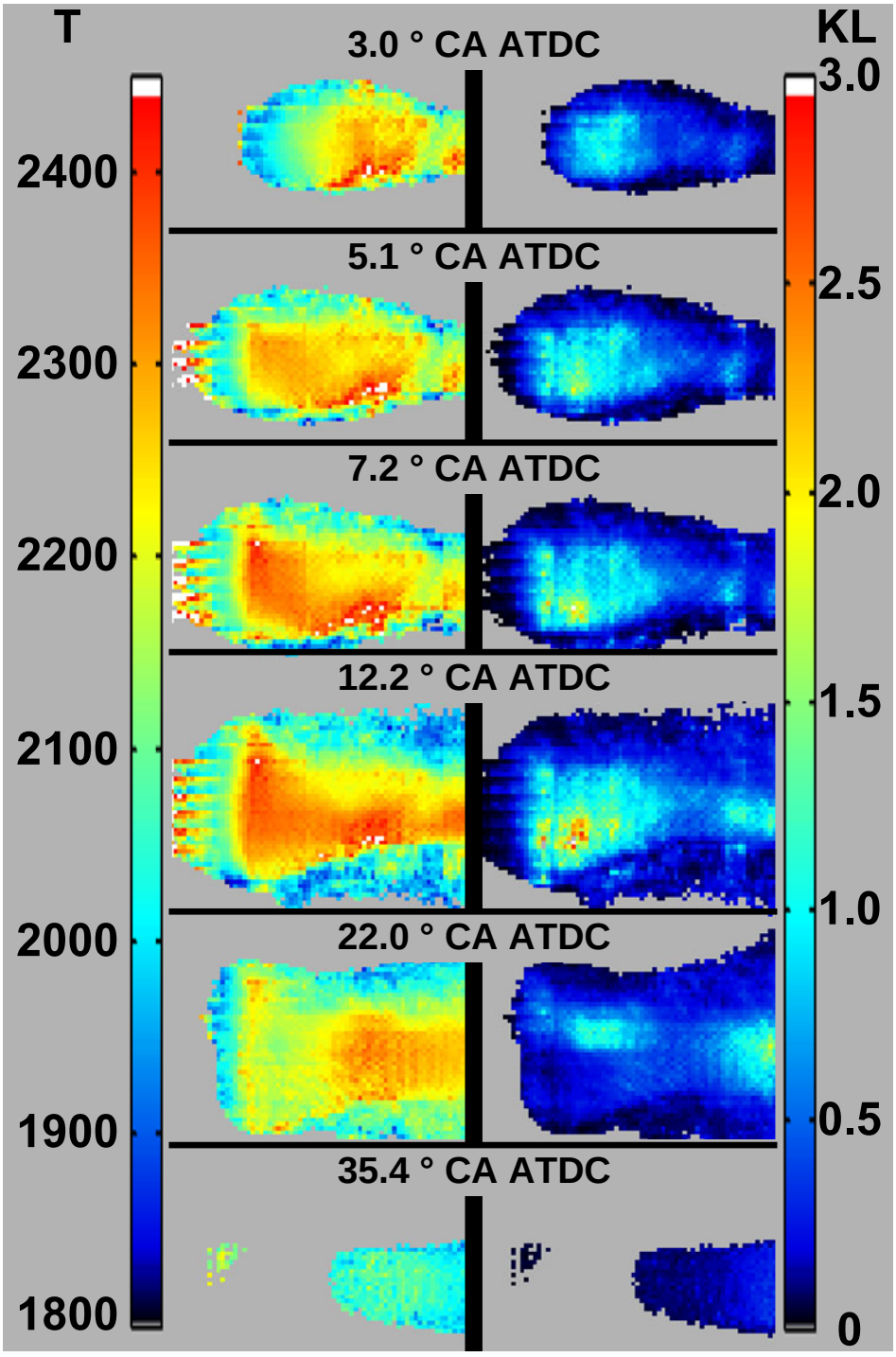

Figure 4-9: Series of data-averaged (over 20 working cycles) temperature (left column) and KL (right column) images for the part load operating point

At a crank angle of 3° ATDC, the jet structure is still being established. Temperatures and KL values in the head increase and the head is observed to elongate as the jet propagates outwards from the injector. By 5.1 ° CA ATDC, temperatures in the head of the jet begin to exceed those further upstream in the jet, the spatial distribution of KL values stabilizes, and the quasi-steady phase of combustion proceeds. Higher temperatures in the jet head can be clearly seen at 7.2 ° CA ATDC, but by 12.2 ° CA ATDC, the injection event has ended and the temperature distribution changes. KL values continue to increase during this phase. The

temperature of the upstream area begins to increase. At 22 ° CA ATDC, the jet structure is no longer seen, and temperatures decrease as the combustion approaches its end. Furthermore, the difference in temperatures in the upstream and downstream regions has decreased. Soot is found in isolated areas of the cylinder and KL values decrease in all regions. The last image at 35 ° CA ATDC shows that the measurable soot is confined to a small region that is typically observed at the right side of these images. This highlights an advantage of the spatial resolution provided by this system: with a fiber optic probe, this behavior during the late combustion would be difficult to measure and describe.

A more detailed quantitative analysis of the results can be performed by selecting three regions of interest for jet 1, averaging the measured temperatures in each of the regions, and showing the progression of these average temperatures as they change with crank angle. These regions are depicted in Figure 4-10.

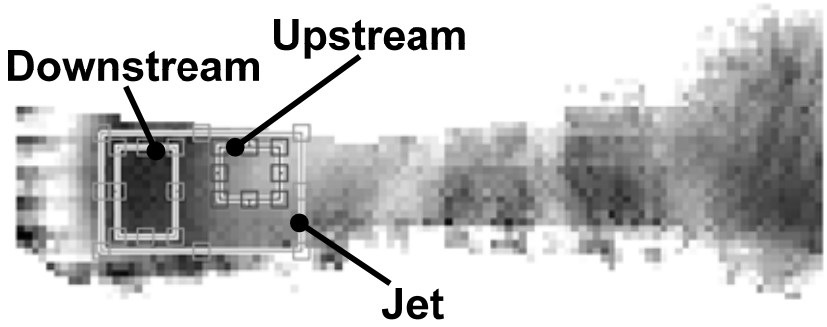

Figure 4-10: Three regions of interest for analysis of the two color pyrometry images.

The regions of interest are labeled “Jet”, “Upstream”, and “Downstream”, in reference to their locations relative to jet 1. This naming convention is used throughout this work when two color method results are presented. The data averaged images are analyzed in this manner and the temperature results are shown in Figure 4-11. The end of indicated injection at 7.8 ° CA ATDC is shown on the diagram; based on Mie scattering results, it is believed that the actual end of injection occurs between 9 ° and 10 ° CA ATDC.

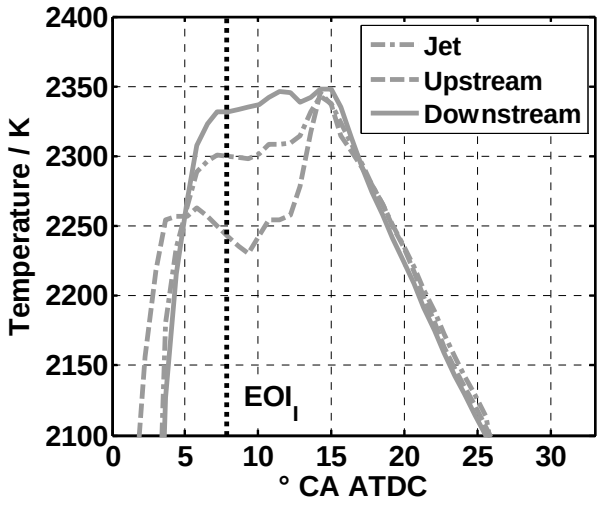

Figure 4-11: Data averaged mean temperature profiles for three regions of interest

During the early combustion phase, combustion temperatures are highest in the upstream portion of the jet. However, these temperatures level off near 2250 K, and the temperatures in the downstream portion of the jet become significantly higher (approaching 2350 K). The mean temperatures in the "Jet" region of interest tend to be in between those of the upstream and the downstream temperatures. After the injection ends, the temperatures in the upstream portion of the jet are observed to increase significantly, whereas temperatures in the downstream portion of the jet remain initially high and then decrease. After approximately 15 ° CA ATDC, temperatures in all three regions of interest are nearly the same and decrease at approximately the same rate. The influence from the flames of jets 2 and 3 on the upstream portion of the jet cannot be discounted, but are considered to be of secondary importance for the following discussion of the temperature profile in the upstream region.

The reason for this behavior in the upstream portion of the jet is explained as follows. According to the current state of knowledge of Diesel combustion (see Chapter 2), the highest temperatures are found in the head of the jet, which agrees with the trends shown in Figure 4-11. The upstream portion of the jet involves break up and vaporization of the liquid fuel via entrainment of air. This requires sensible enthalpy from the air and thus decreases temperatures, so that the combustion temperatures are decreased for a given stoichiometry. As the combusting mixture progresses downstream and more air is entrained, more energy is released by combustion and the temperature continues to increase. As mentioned above, as the injection event ends, the liquid penetration depth decreases. This phenomenon has been observed and explained by others (see, for example, [137]). A simple control volume analysis of a liquid fuel jet entraining air provides important insight into this decrease in penetration depth, as is done in [137]. The control volume shown in Figure 4-12 is placed around an arbitrary portion of the jet. Fuel flows into the control volume (subscript f), as does air that is entrained by the jet (subscript a). Assuming a constant mass inside the control volume with steady-state conditions, the resulting flow out of the control volume is the sum of the mass flows of entrainment air and fuel.

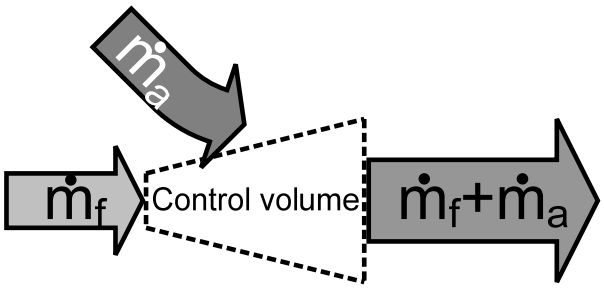

Figure 4-12: Control volume for a portion of a fuel jet with entrainment air

At the end of the injection, the mass flow of fuel into the control volume slows down and stops, as does the flux of momentum that accompanies the fuel. However, the already entrained air and the fuel in the control volume continue to move out of the control volume. For a constant density inside the control volume, the mass that is no longer being provided by the injection must be replaced with entrained air, so the entrainment increases. This increased entrainment rate travels as a wave outward from the injector [137]. Increased entrainment means that the fuel can be vaporized faster, so the penetration depth decreases. At the same time, this means that fuel is more rapidly heated by the enhanced air entrainment, so combustion can take place further upstream than before. The region of high flame temperatures is observed to retract upstream towards the injector, and the timing coincides well with the end of the injection.

For the three regions of interest shown in Figure 4-10, the mean KL values (calculated from KL_1: wavelength of 550 nm) can be plotted as a function of crank angle; these are shown in Figure 4-13.

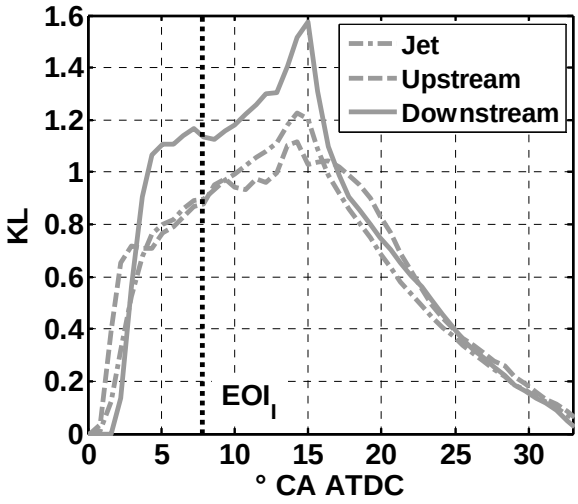

Figure 4-13: Data averaged (over 20 working cycles) mean KL profiles for three regions of interest

Inspection of the profiles reveals that after the initial transient, measured KL values are higher in the downstream region of interest. This is the expected behavior for Diesel combustion (see Chapter 2), as the highest soot concentrations should exist in the head of the jet. For every region of interest, soot concentrations increase nearly continuously until approximately 14 ° CA ATDC. This indicates that soot formation rates are higher than oxidation rates. If indeed the lift-off lengths decrease as the combustion process progresses (see Figure 4-7 and its explanation), it would suggest that increasingly rich conditions exist in the upstream region, and so soot concentrations would be expected to increase with time. Just before 14° CA, KL values increase sharply to their absolute maximum values. This is likely associated with the combustion of the last fuel to be injected and the enhanced entrainment due to the end of injection. After reaching their maxima, the KL values for every region of interest decrease continuously towards a value of 0. The upstream KL values begin to decrease slightly before the upstream values, which indicates that oxidation dominates formation at an earlier time in the upstream region. However, the upstream KL values decline rapidly at first, so that after approximately 18 ° CA ATDC, the KL values for all three regions of interest are nearly the same and decline at similar rates.

The ability of the two color pyrometric system to measure combustion temperatures for individual working cycles provides insight into the cyclic variability observed with this operating point. Shown in Figure 4-14 are the mean temperature and KL profiles for two individual working cycles (shown as thin lines) and the data averaged temperature and KL profiles (shown as a thick line) for both the upstream (top) and the downstream (bottom) regions. These two working cycles (A and B) have been chosen to demonstrate that some temperature profiles (i.e. A) are characterized by lower than average temperatures, whereas some demonstrate considerably higher temperatures for portions of the cycle (B). These deviations from the mean behavior will be discussed below, first for cycle A and then for cycle B.

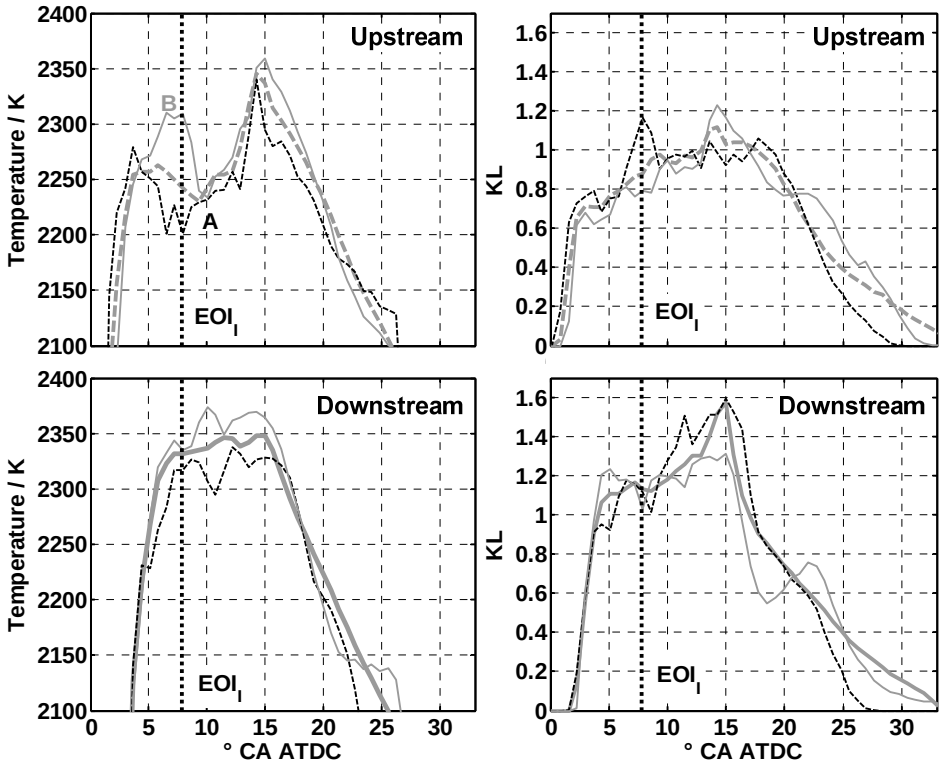

Figure 4-14: Mean temperature and KL profiles in the downstream and upstream regions for two individual working cycles (thin lines); data-averaged (over 20 working cycles) mean temperature and KL profiles in the upstream and downstream regions (thick lines)

Upstream temperatures and KL values for cycle A increase faster than average and remain at slightly higher than average values until shortly before 5 ° CA ATDC. Then, upstream temperatures decrease significantly, drop below the mean temperature near 5 ° CA ATDC and reach a minimum near 6.5 ° CA ATDC: Shortly after the decrease in temperature starts, soot KL values increase sharply and peak at approximately 170% of the mean KL value near EOI_I. After this, temperatures and KL values behave somewhat similarly to the average profiles. During the later phase of combustion, however, the rate of temperature decrease is slower than average and the KL values decrease faster than the average. Measurable soot in the upstream region ceases to be detected much earlier than for the data-averaged cycle. For this same working cycle, downstream temperatures and KL values increase at a rate very similar to the average until shortly before 5 ° CA ATDC. Both the measured temperature and the KL value stop increasing momentarily. Downstream temperatures remain lower than average for most of the remainder of the cycle. A noticeable depression in the temperature is detected several crank angle degrees after the upstream temperature depression. At the same time of this downstream temperature decrease, downstream KL values increase sharply and reach nearly the same peak value as the data-averaged KL value at the same crank angle. These observed trends are explained by the following theory.

The substantial decrease in upstream temperatures near 5 ° CA ATDC results from a locally higher fuel concentration. This has the following consequences:

- More sensible enthalpy is required from the air to vaporize and heat the larger amount of fuel, thus decreasing combustion temperatures.

- The mixtures found in this region are rich of stoichiometric (see Chapter 2), so this potential increase in the fuel/air ratio also leads to a decrease in combustion temperatures.
- The increased local fuel/air ratio increases the amount of soot formed. This is measured near EOI_I. Increased soot concentrations increase the flame's radiative heat losses, thus suppressing temperatures.

The KL values in the downstream region stop their initial increase prematurely, which indicates that local soot formation rates have stopped or are balanced by oxidation rates. The temperatures momentarily stop increasing, as well. This may be due to the temporary and short-lived presence of a lean mixture. Temperatures in the downstream region remain lower than average. The rich pocket that was observed in the upstream region travels downstream due to the momentum imparted by the high-velocity fuel jet. A depression in downstream temperatures is observed, followed by a substantial increase in downstream KL values. These observations are characteristics of a richer combustion and of spray-driven transport phenomena. If it is assumed that the same amount of fuel is injected through each injector nozzle in each cycle, then the presence of a rich mixture early in the combustion process could lead to leaner mixtures at later phases. The soot is formed at more advanced crank angles and therefore has more time to be oxidized. The dramatic decrease in downstream KL values late during the combustion may be indicative of this.

Cycle B behaves much differently than cycle A and in some ways, as is seen in Figure 4-14, mirrors the behavior of cycle A. Upstream temperatures and KL values first increase at approximately the average rate, but at slightly later crank angles. After the data-averaged mean upstream temperature essentially levels off, the temperatures for cycle B continue to increase and remain at significantly higher levels until after EOI_I. After this, they decrease and follow the same trend as the mean temperatures during the entrainment-driven temperature increase. Upstream temperatures decrease slightly faster than average during the late combustion phase. Upstream KL values remain slightly lower than average until just before reaching their maximum at the same crank angle as the averaged trace. The maximum upstream KL value for this cycle is higher than average. In the late phase of combustion, as KL values are in decline, the upstream KL value for this cycle ceases its decline for approximately 3-4 ° CA, after which the values decrease to zero. Downstream temperatures for cycle B increase at the average rate, but remain somewhat higher than the average until the late stages of combustion. Downstream KL values also increase in a similar fashion to the average, and are briefly above average until approximately 7 ° CA ATDC. After this, the KL values remain below average and do not exhibit the typical dramatic increase associated with the end-of-injection entrainment enhancement. During the late combustion phase, KL values are initially below average. Slightly before the observed cease of temperature decline, the KL values increase by more than 35% before resuming their decline. As with cycle A, a theoretical explanation for these observations is presented.

The significantly larger temperatures observed upstream for much of the early phase of combustion, combined with the lower than average soot KL values, suggests that for these early stages, combustion occurs at leaner than average fuel-air ratios that are closer to stoichiometric. As a result, downstream temperatures are typically above average. Downstream KL values are initially higher than average, possibly because soot formation reactions are also endothermic (see Chapter 2), but generally remain at or below average for most of the combustion process. If the conditions early in the combustion process are lean, then it may be expected that conditions later are rich, because the same amount of fuel is assumed to be consumed. This appears to occur relatively late in the combustion process, as soot is formed after temperatures have declined significantly. However, the temperature slows

its decline, which suggests that a pocket of rich mixture is being actively combusted. Apparently, the cylinder contents have not yet expanded and cooled below a critical temperature, and the soot can be oxidized before the end of combustion.

The data shown thus far have been taken from sets of measurements that were performed before significant fouling occurred, so the effects of fouling have been neglected. It is desirable to develop a method to correct for window fouling so that measurements taken with fouled windows can be corrected. The procedure developed in this work is described in Chapter 3 and evaluated here. To this end, series of measurements were taken for various parameter variations, and a reference operating point was measured at the beginning and at the end of each set of measurements. The measurements taken at the beginning of the series cannot be adjusted according to the procedure defined in Chapter 3. The measurements at the end are processed both with and without the fouling correction for the sake of comparison. Typical results achieved with this correction technique are shown in Figure 4-15 for the data-averaged temperatures in the downstream region for two measurement series (labeled "1" and "2"). The thick gray lines are the reference measurements taken at the beginning of each series. The reference measurements taken with the fouled window at the end of each series are shown in uncorrected form (thin gray lines) and in corrected form (dashed black lines).

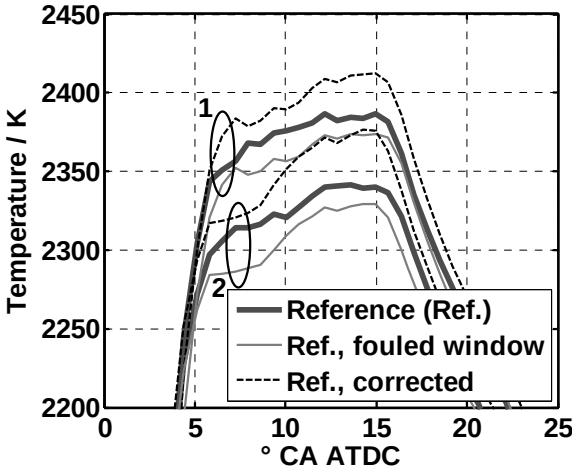

Figure 4-15: Mean data-averaged temperature profiles in the downstream region for two different measurement series. Reference measurement points at the beginning: thick gray lines; reference measurement points with fouled windows: thin gray lines (without correction); dashed black lines (with correction).

It is apparent from the profiles that window fouling leads to measured temperatures that are too low. The correction overcompensates, so that the corrected temperatures are higher than for the corresponding reference taken at the beginning of each series. The following factors may contribute to this overcompensation:

1. As shown in Chapter 3, the degree of fouling is overestimated for the last measurement in a series due to the assumption that fouling stops with the last measurement and not when the engine is switched off. Experience with motored operation of this engine has demonstrated that windows are rapidly fouled by oil that is in the cylinder. Although care was taken to switch the engine off as soon as possible after the last measurement in a series, the engine coast-down process takes a considerable amount of time, during which additional fouling may occur.

2. The halogen lamps used for the reference images were not bright enough to illuminate a significant portion of the calibration target, and signal intensities were generally low. Small errors introduced by noise may have significant impacts on the quality of the correction.
3. Although the current flowing through the lamps was held as constant as possible, the possibility exists that the lamp intensity drifted between two consecutive calibration target images (one image with the fouled window and one shortly thereafter with the reference window). This would degrade the reliability of the fouling correction.

Improvements to the measurement process should help decrease the amount of fouling that occurs before and after the measurements are taken, thus reducing errors in fouling compensation. The 20 W lamps used in this work may be powerful enough to illuminate a calibration target, but their position with the current prototype calibration target design is likely not optimal. Such optimization could potentially provide satisfactory illumination. Additionally, the output of the lamps could be monitored to improve their temporal stability. Care would need to be taken to make sure that this monitoring is independent of sensor temperature, as the calibration target is inserted into a hot engine.

With the system in its current configuration, temperature differences of less than approximately 50 K that are observed within a series of measurements of a parameter variation may not be significant. This will be taken into consideration for the data shown below.

4.3. Rail Pressure Variation

In this subchapter, the effects of rail pressure on soot emissions for the part load operating point are investigated. Rail pressures of 1600 bar and 2000 bar are investigated and compared with the baseline 1800 bar case. For each rail pressure, the pilot injection duration is adjusted to maintain the same pilot injection mass as with the 1800 bar case, and the main injection durations are adjusted to maintain a constant $IMEP_n$ across all three measurement points. Consequently, the injection duration is longest for the injection pressure of 1600 bar, followed by the injection pressure of 1800 bar, and finally by the pressure of 2000 bar. The start of injection was held constant for all three operating points. Measurements made with a smoke meter, combined with the exhaust gas emissions and other parameters measured during the investigations, are used to determine the engine-out specific soot emissions (normalized by the indicated power). These emissions are normalized by the value determined at a rail pressure of 1800 bar are shown below in Figure 4-16 for the sake of comparison.

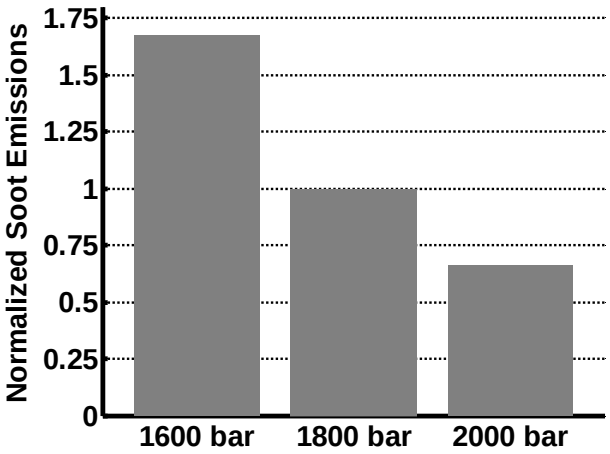

Figure 4-16: Normalized engine-out indicated specific soot emissions for rail pressures of 1600, 1800, and 2000 bar

Clearly, an increase in fuel injection pressure from the 1800 bar baseline results in lower engine-out soot emissions, and a decrease in injection pressure leads to increased soot emissions. A variety of the optical measurement techniques employed in this work are utilized to gain insight into the processes responsible for this behavior.

4.3.1. Mie Scattering

The averaged, thresholded Mie scattering images are used to calculate the penetration depths for a portion of the quasi-steady combustion phase for each of the three operating points. In each case, combustion luminosity eventually made interpretation of the scattering signal impossible, and the ends of the curves occur at different crank angles. In Figure 4-17, the penetration depths are shown for all three cases. The start of combustion for the main injection as indicated by the cylinder pressure diagrams is shown as a vertical gray bar; it is approximately the same for all injection pressures. The cylinder pressure at the beginning of injection is approximately 5.6 MPa. The indicated ends of injection (EOI_I) are also shown in the diagram as short vertical bars corresponding to each rail pressure.

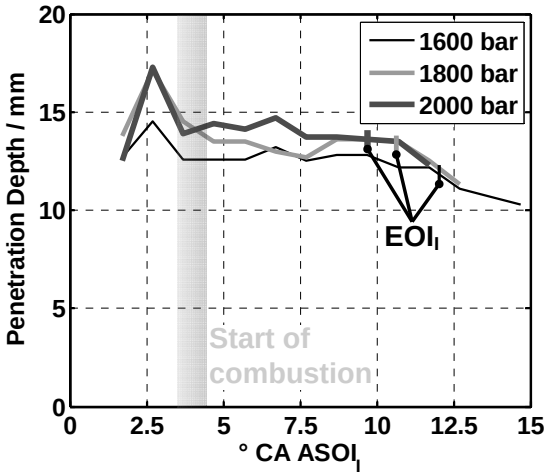

Figure 4-17: Liquid penetration depths for rail pressures of 1600 (thin black line), 1800 (light gray line), and 2000 (thick dark gray line) bar; the start of the main combustion is indicated with a gray beam

A clear trend is not observed in the data, although the penetration depths for a rail pressure of 1600 bar may be marginally shorter than for the other rail pressures. More carefully controlled experiments in a pressure chamber have shown that the penetration depth is not affected by the injection pressure to any significant extent [14]. The reasons for this are explained by Siebers in [14] as follows: fuel vaporization in a Diesel spray is governed by air entrainment (as described in Chapter 2). The rate at which air is entrained (and sensible enthalpy is made available to vaporize fuel) dictates the rate at which the fuel is vaporized and therefore the penetration depth. Assuming steady state, incompressible flow, the velocity of fuel being injected through the injector nozzle (v_f) is given by [51]:

$$v_f = C_D \cdot \sqrt{\frac{2\,\Delta p}{\rho_f}} \tag{4.1}$$

where:

C_D is the nozzle discharge coefficient

ρ_f is the density of the fuel, assumed to be constant

Δp is the pressure drop across the nozzle

The corresponding fuel mass flow rate is defined as:

$$\dot{m}_f = \rho_f \cdot v_f \cdot \pi \cdot d^2/4 \qquad (4.2)$$

where:

d is the diameter of the nozzle

From these relationships, it is apparent that the fuel velocity and thus the fuel mass flow rate increase with the square root of the increase in injection pressure drop. If the rate of entrainment and vaporization were independent of the fuel's velocity, then the time taken to vaporize a given mass of fuel would remain the same, and the liquid fuel would penetrate further into the cylinder before being completely vaporized. Thus, penetration depth would increase with increasing injection pressure. However, the air entrainment rate is also proportional to the fuel's velocity [14]:

$$\dot{m}_a \propto \sqrt{\rho_a \rho_f} \cdot d \cdot x \cdot v_f \cdot \tan(\alpha/2) \qquad (4.3)$$

where:

ρ_a is the air density

x is the distance along the jet axis

α is the spreading angle of the spray jet (see Figure 2-2)

Because the air entrainment rate also scales with the square root of the injector nozzle pressure drop, the liquid fuel is vaporized faster with higher injection pressures, so the penetration depth is not expected to be significantly affected by rail pressure. The results presented in Figure 4-17 are certainly not conclusive, but they do not present sufficient evidence to suggest that rail pressure has a significant effect on the liquid penetration depth for this operating point.

4.3.2. OH Chemiluminescence

In order to investigate possible differences in the mixing process, logarithmic radial intensity profiles are calculated in the same manner as shown in Figure 4-7 for 5-cycle-averaged images at a crank angle of 8 ° $ASOI_I$. This crank angle is representative of the quasi-steady phase of combustion for each of the injection pressures. The profiles are plotted below in Figure 4-18.

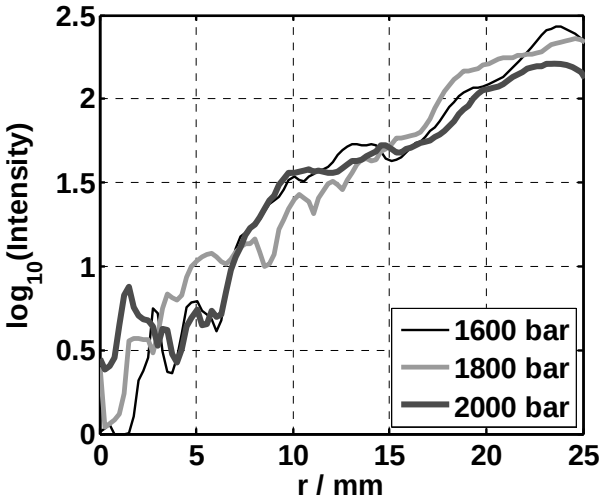

Figure 4-18: Averaged logarithmic radial intensity profiles for the part load operating point at 8 ° CA $ASOI_I$

As was the case with the standard operating point, it is difficult to identify a "knee" in these profiles, so a determination of the lift-off length is not possible. However, the profiles are indeed very similar, particularly those for injection pressures of 1600 and 2000 bar. There are differences in the profiles at radial distances less than 5 mm, but it is unclear if these are related to differences in lift-off lengths. It seems likely that the chemiluminescence signal from jets 2 and 3 interferes with the signal from jet 1, thus confounding the results shown in Figure 4-18. Optimizations to the injector and optical access designs, as well as improved experimental procedures, should improve the ability of this technique to examine lift-off lengths in detail (see 4.2.3).

That said, it is expected that an increase in fuel velocity associated with an increase in injection pressure leads to an increase in lift-off length (see [28]). For the injection pressures studied here, the expected change in lift-off length would be on the order of several mm. Siebers and Higgins also show that this increased lift-off length implies that an increased amount of air has been entrained upstream of the lift-off length. The resulting rich premixed reaction zone downstream of the lift-off length would then be characterized by leaner mixtures, so decreasing soot formation rates are expected with increasing injection pressures.

4.3.3. Natural Soot Luminosity

The two color pyrometric data from the rail pressure variation experiment were unable to be correctly processed. Temperatures and KL values are not available for this variation, but an examination of the natural soot luminosity as measured through the 700 nm bandpass filter (see Chapter 3) can provide some insights about the differences between the three operating points. The fouling correction procedure failed to produce plausible correction factors, so the intensities have not been corrected. For this reason, the luminosity values of the 2000 bar and the 1600 bar cases may be biased towards lower intensities. Mean, data-averaged combustion luminosities (in arbitrary units) are plotted in Figure 4-19 for the upstream and downstream regions shown in Figure 4-10.

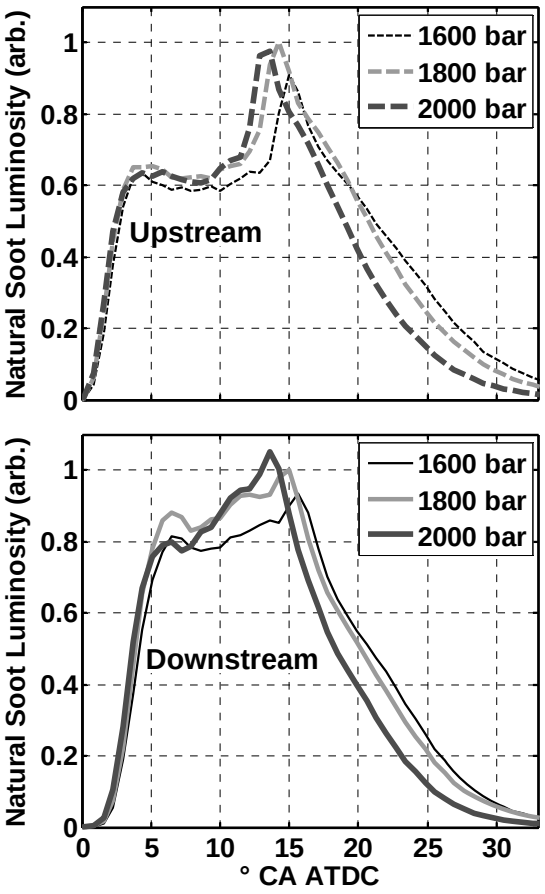

Figure 4-19: Mean, data-averaged soot luminosities (measured through the 700 nm bandpass filter) for the upstream (top) and downstream (bottom) regions of interest with rail pressure as a parameter

The locations of peak upstream luminosities show a definite trend with changing rail pressure. As rail pressure is decreased from 2000 bar, the peak luminosities are observed to occur at later crank angles. Higher luminosities are observed for the lower injection pressures during the late phase of combustion. For the downstream region, a similar trend for the locations of peak soot luminosities is observed. The behavior of the downstream luminosities, however, is not logical. As stated in 4.3.2, it is hypothesized that more soot forms as a result of the shorter lift off lengths that are expected with lower rail pressures. Between 2000 and 1800 bar, such a trend can be observed, as intensities are higher for 1800 bar than for 2000 bar. It is believed that the soot formation at a rail pressure of 1600 bar is indeed higher than for a rail pressure of 1800 bar. This increased soot formation likely leads to higher rates of window fouling and thus to artificially low measured intensities. Despite any such errors, the soot luminosities remain higher during the late phase of combustion at lower rail pressures.

The longer injection durations required to achieve the same load at a rail pressure of 1600 bar mean that soot must be oxidized at later crank angles. The cylinder contents have expanded more and temperatures are lower, so oxidation is hindered. This mechanism is believed to contribute significantly to the increased soot emissions at lower injection pressures. If indeed soot formation rates are higher during the early stage of combustion for lower injection pressures, then radiative heat losses are likely to be higher for the lower injection pressures. This may also contribute to the higher soot luminosities measured at later stages of the combustion. It is unclear if the change in injection pressure also has a measurable effect on the enhancement of air entrainment for the pressures involved here. This could potentially

impact soot formation during the late combustion phase, as well. Improvements to these two color pyrometry techniques will enable a more detailed parametric study and provide conclusive data that more thoroughly address these hypotheses.

Increased rail pressures may lead to changes in the liquid penetration depth, but theory suggests that these changes are not significant. Measured OH chemiluminescence intensities provide some preliminary evidence that lift-off lengths may be affected by rail pressure to some extent, but these results should be viewed critically. Future developments of this measurement technique (see 4.2.3) should enable comparisons of these trends with data from the literature. Natural soot luminosity data is also inconclusive, but suggests that a significant cause of increased engine-out soot emissions is the fact that fuel is injected later in the cycle at lower rail pressures. Thus, soot must be oxidized in a cooler environment, and the probability that this oxidation is not complete by the time the exhaust valve opens is higher.

4.4. Effects of the Pilot Injection

As part of the first implementation of the OH chemiluminescence imaging technique developed in this work, an operating point without a pilot injection was observed. The main injection timing was advanced by 2 ° CA to maintain a similar point of 50% mass fraction burned, and the duration of the main injection was adjusted to achieve the same $IMEP_n$. Averaged, filtered cylinder pressure traces for both operating points are shown in Figure 4-20, along with the indicated starts and ends of the injection events. Starts of injection are indicated with dashed lines, whereas ends of injection are shown with solid lines. Black lines correspond to the operating point without a pilot injection, and gray lines correspond to the standard part load operating point with a pilot injection. EOI_I stands for the indicated end of injection, and $EOI_{I,p}$ stands for the indicated end of injection for the pilot injection.

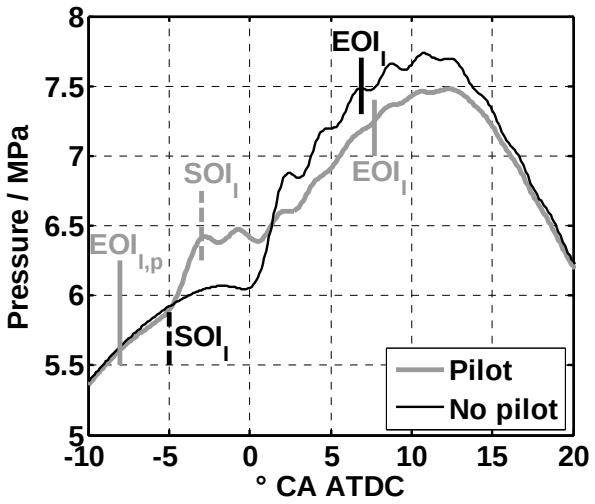

Figure 4-20: Averaged, filtered cylinder pressure traces for the part load operating points with (thick gray line) and without (thin black line) a pilot injection

The pressure trace for the operating point without a pilot injection is characterized by steeper rates of pressure increase as a significant portion of the fuel that has been injected into the cylinder before the time of ignition ignites. This phenomenon is well understood. Even with the filtering technique used for these data, the pressure trace for the operating point with no pilot injection shows significant fluctuations, which is attributed to acoustic effects resulting

from the rapid premixed phase of combustion. Peak pressures are slightly higher for the case with no pilot injection.

For these investigations, Mie scattering data are not available. It is hypothesized that the liquid penetration depths are shortened by the heat released by the pilot injection. Higher local temperatures would likely contribute to faster vaporization of the fuel. However, the results shown in Figure 4-17 suggest that the change in penetration depth would likely not be more than two or three mm.

Information based on optical measurements about the interaction between the pilot injection and the main injection, particularly at the time of ignition, has not been widely published. Hasse and Peters have, however, modeled this interaction for a smaller Diesel engine, thus providing a theoretical basis for understanding the phenomena involved [138]. Here, the OH chemiluminescence technique is applied to provide information about this phenomenon.

4.4.1. OH Chemiluminescence

The first such set of optical measurements devoted to this purpose is a comparison of OH chemiluminescence imaging data. To this end, series of chemiluminescence images are taken for a range of crank angles. At each imaged crank angle, five images are taken and averaged. Each averaged image is thresholded with a threshold value of 10% of its maximum value. This method is effective at early crank angles, during which imaged intensities are low, because the threshold value scales with the highest intensity of the image. At later crank angles, when image intensities are high, the threshold effectively removes unwanted reflections that result from high intensities. Finally, for each thresholded image, an average of all pixel intensities higher than the threshold is computed. This is performed for a range of crank angles and plotted against the crank angle after the start of the main injection in Figure 4-21.

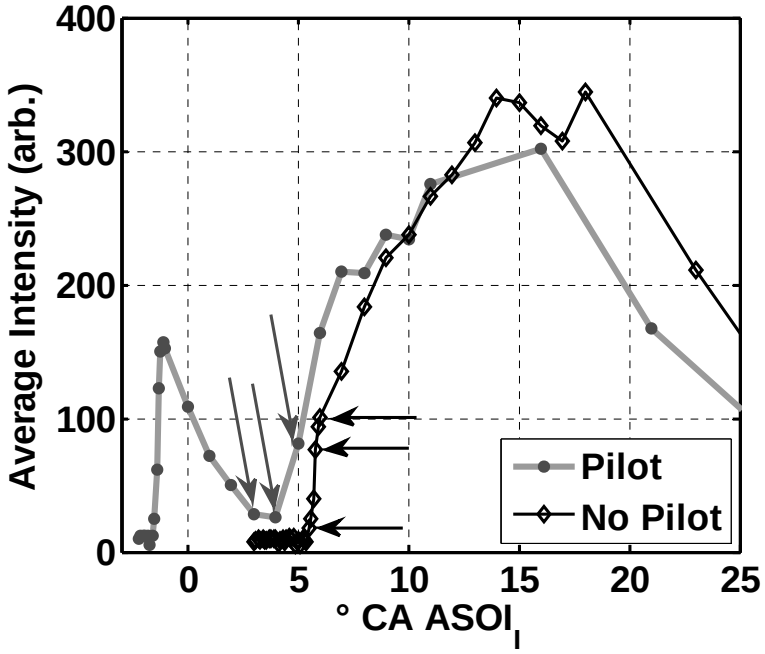

Figure 4-21: Average OH chemiluminescence intensity profiles as a function of crank angle after the start of the main injection for the part load operating point with and without a pilot injection

It is clear from the plot for the pilot injection case that near stoichiometric, high temperature combustion results from both injections, as distinct curves are observed for each one.

Analysis of the two color pyrometry images indicates that no measurable soot luminosity is observed during the combustion of the pilot injection, which suggests that significant mixing takes place during the ignition delay of the pilot injection. The average chemiluminescence intensity does not decrease to zero after the pilot combustion peak. The rate of decline becomes less, and then the average intensity begins to increase again as a result of the combustion of the main injection. It is possible that for the highest intensities measured, some of the signal results from unwanted soot luminosity passing through the filter. What is of interest for this study is the ignition behavior of the main injection, so soot luminosity is neglected as a source of experimental error. The average chemiluminescence intensities for the operating point without a pilot injection begin their increase after a longer delay period. This does not appear to agree with the ignition delay behavior that can be inferred from the cylinder pressure traces in Figure 4-20. This suggests that OH chemiluminescence intensity is not a suitable indicator of heat release, but also that the ignition and/or inflammation of the main injection is significantly altered by the pilot injection. In order to better understand this phenomenon, images are examined each operating point at three different crank angles before and after the rapid increase in OH chemiluminescence signal. These crank angles are indicated with arrows in Figure 4-21. The chemiluminescence images for five individual cycles at crank angles of 3, 4, and 5 ° CA $ASOI_I$ are shown in the first five rows in Figure 4-22; the average images of the five individual images for each crank angle are shown in the bottom row.

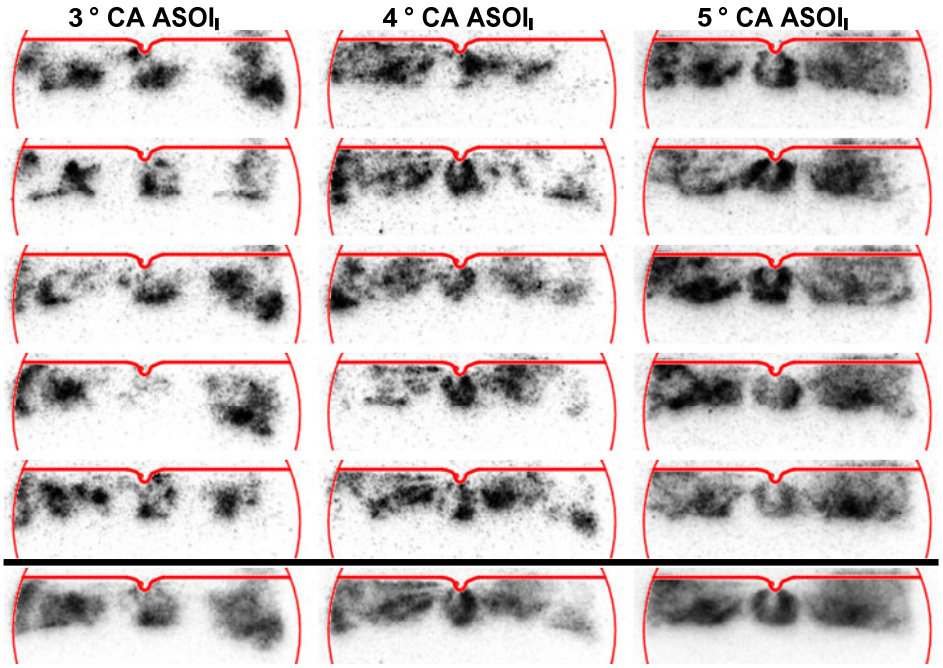

Figure 4-22: OH chemiluminescence images for the part load operating point with a pilot injection; the bottom row of images is comprised of ensemble averages of the five individual cycle images

As seen in Figure 4-21, at a crank angle of 3 ° CA $ASOI_I$, the chemiluminescence of the pilot injection is for the most part finished and a significant contribution from the main injection is not yet observed. An examination of the images reveals that the measured (relatively weak) OH signal occurs in three regions that correspond to the downstream regions of the injector nozzles. A jet like structure is not apparent, which suggests that this chemiluminescence is still related to the combustion of the pilot injection. At 4 ° CA ATDC, the average intensity has decreased slightly, but in many of the individual cycles and in the average image, a jet structure can begin to be identified (for jet 1 shown in Figure 4-2) as what appear to be low

intensity streaks surrounded by at least some OH chemiluminescence. This is indicative of a direct interaction between high-velocity liquid fuel and regions of near stoichiometric combustion, and has significant implications for the entrainment and heating processes of the main injection, and thus for the ensuing combustion process. At 5 ° CA $ASOI_I$, average chemiluminescence intensities increase significantly and a more defined jet structure can be identified. Shortly thereafter, the jet structure stabilizes during the quasi-steady phase of combustion.

In a manner similar to Figure 4-22, chemiluminescence images for the part load operating point without a pilot injection are shown for several crank angles in Figure 4-23; as before, the bottom row of images is comprised of ensemble averaged images.

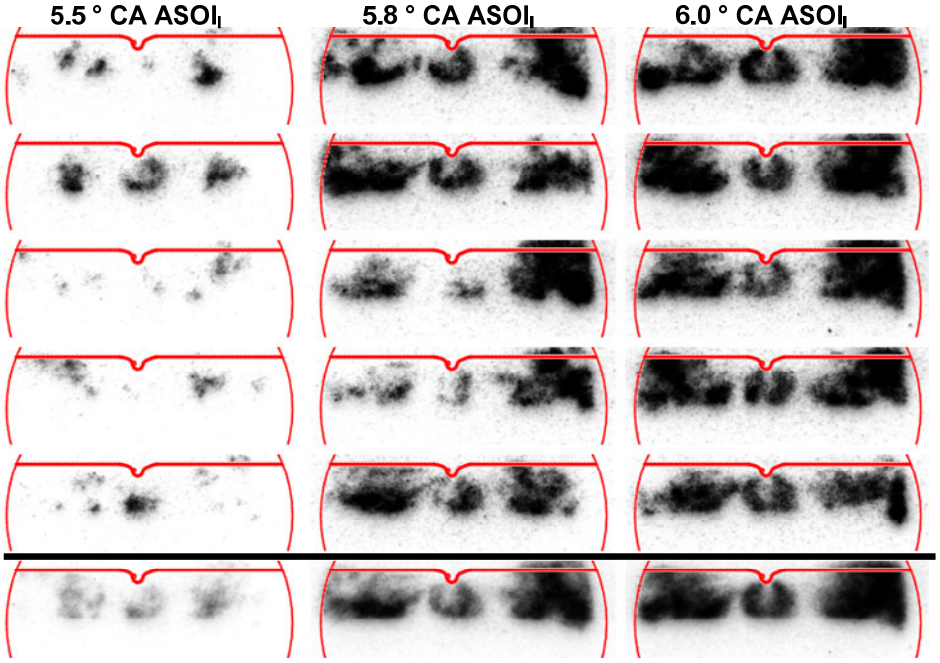

Figure 4-23: OH chemiluminescence images for the part load operating point without a pilot injection; the bottom row of images is comprised of ensemble averages of the five individual cycle images

For the crank angle of 5.5 ° CA $ASOI_I$, the OH chemiluminescence observed in individual cycles exhibits significant fluctuations, both in terms of the spatial distribution and the intensity. Some individual cycle images and the average image suggest, however, that the locations in which chemiluminescence is measured are confined to three regions of the cylinder that are downstream of the nozzle holes. At 5.8 ° CA $ASOI_I$, a more developed jet structure can be seen in many, but not all, of the individual cycles and in the ensemble average image. At 6 ° CA $ASOI_I$, this jet structure is more prominent as the quasi-steady portion of the combustion progresses.

The differences between Figure 4-22 and Figure 4-23 are difficult to quantify but are indicative of substantial differences in the ignition processes of the main injection. The simulations performed by Hasse and Peters show that with a pilot injection the ignition of the main injection involves the interaction of the main injection's mixture field with the combusting mixture field of the pilot injection [138]. This leads to the development of a premixed, near-stoichiometric, strained flame that propagates towards the main injection and ultimately leads to its ignition. The transfer of heat and mass between these two mixture fields governs the ignition of the main injection; this cannot occur during the ignition of the pilot injection or the main injection without a pilot injection. Furthermore, the authors show that

high scalar dissipation rates (caused by large gradients in mixture fraction) increase the propagation speed of the premixed flame that ignites the main injection, so the ignition delay of the main injection is shortened by these higher mixture gradients. For autoignition of a Diesel jet without a pilot injection, higher scalar dissipation rates inhibit autoignition [138]. The thin, low-intensity streaks seen in Figure 4-22 likely indicate that interaction between the two mixture fields occurs, but it is difficult to assess this as the chemiluminescence intensity does not provide mixture field specific information. Simultaneous Mie scattering and OH chemiluminescence may prove to be a useful measurement technique for future investigations. Variations in pilot injection quantity and timing may provide more insight into the phenomena that govern the ignition of the main injection. Optimization of the optically accessible engine (i.e. by removing the uppermost compression ring to reduce sources of error in the cylinder volume calculation) are expected to enable heat release analyses, which should accompany the optical investigations.

The fact that the combustion of the pilot injection takes place in the same location in which fuel for the main injection is injected has implications for the entrainment and mixing processes that follow. It is expected that the higher temperatures resulting from the combustion energy released by the pilot injection improve vaporization. The lift-off length is known to decrease with higher in-cylinder temperatures (see [28]). At the same time, the oxygen content of the cylinder is locally depleted because fuel has been consumed. Lower oxygen concentrations have been observed to increase lift-off lengths [139]. A comparison of logarithmic radial OH chemiluminescence profiles (each is generated from a five-cycle ensemble average image and the average profile of the 180°, 182°, 184°, and 186° profiles as shown in Figure 4-5) is shown in Figure 4-24 with the crank angle as a parameter.

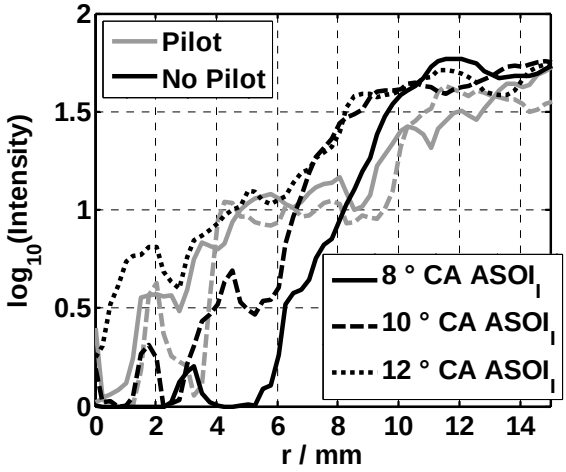

Figure 4-24: Averaged logarithmic radial intensity profiles for the part load operating point with (gray curves) and without (black curves) a pilot injection for a range of crank angles

As discussed above, lift-off lengths cannot yet be quantified with this experimental setup. However, general trends in apparent lift-off lengths can be obtained from comparing data at different crank angles and with different operating parameters. For the part load operating point without a pilot injection, a recession in lift-off length is observed with progressing crank angle. This does not appear to be the case with the pilot injection, as the interpretation of these profiles is less straightforward. However, for a given crank angle (as measured after the indicated start of injection), the implied lift-off lengths may be shorter with a pilot injection. It is therefore hypothesized that the temperature increase that results from the combustion of the pilot injection overwhelms any oxygen concentration effects to create shorter lift-off lengths

with the pilot injection. This is expected to lead to advancement of soot formation with a pilot injection.

4.4.2. Two Color Method

The fouling correction for the comparison between operation with and without a pilot injection yielded plausible values. The reference measurement point, which in this case is the part load operating point with a pilot injection, was measured first, so no correction is applied. Immediately following this, the part load operating point without a pilot injection was measured, and these data have been corrected for fouling. The mean upstream and downstream temperatures and KL values are shown in Figure 4-25. They are plotted against the crank angle after the indicated start of the main injection, not after top dead center. For the downstream KL profiles, the median profiles are also shown. This is because at the high measured soot concentrations, uncertainties are also high (see Chapter 3). Some of the KL values could not be accurately computed and have been set to zero, so a median value for the region of interest effectively removes the bias that would otherwise result from this numerical instability. For all other measurements, the mean and the median values are essentially indistinguishable.

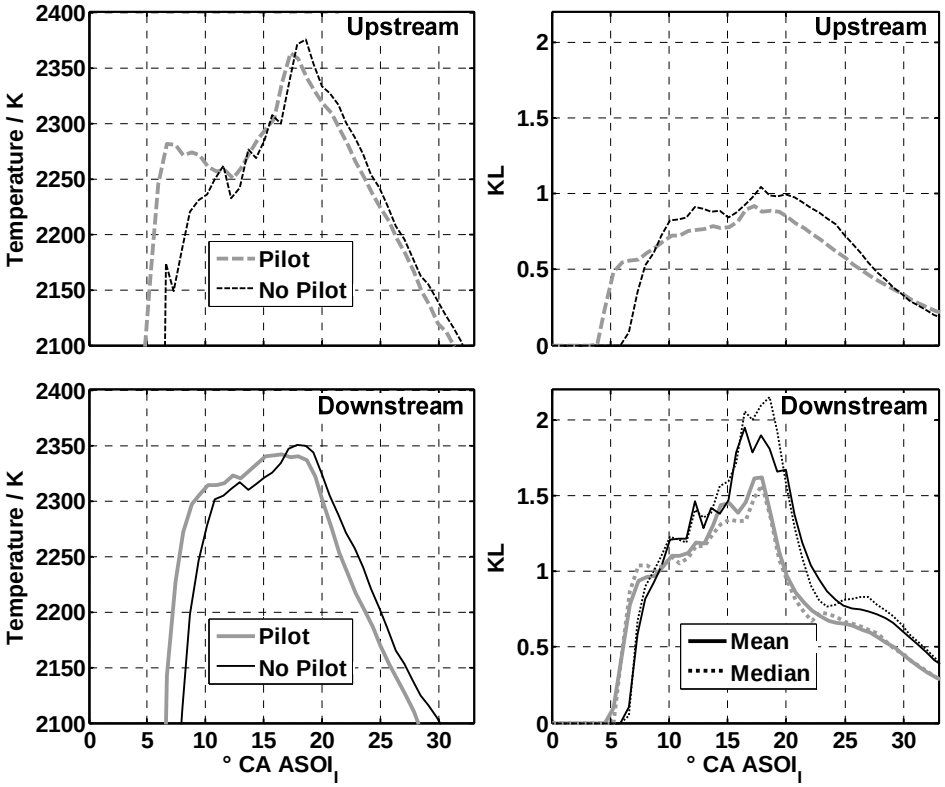

Figure 4-25: Mean, data averaged (over 20 working cycles) temperature and KL profiles in the downstream and upstream regions for the part load operating point with a pilot injection (gray lines) and without a pilot injection (black lines); data are plotted against degrees crank angle after the indicated start of the main injection; median downstream KL profiles are shown as dotted lines for the sake of comparison with the mean

The upstream temperature profiles exhibit different trends. The initial peak that is observed at approximately 7 ° CA $ASOI_I$ that occurs with a pilot injection is not observed without a pilot injection. The upstream temperatures begin to increase later in comparison to the start of injection without a pilot injection. However, the upstream temperatures continue to increase

and the peak temperatures may even be slightly higher without the pilot injection (uncertainty associated with the fouling correction prevents a definite conclusion). The duration of the main injection is longer without a pilot injection, so upstream temperatures without a pilot take longer to reach their peak. The ensuing temperature falloff occurs at approximately the same rate both with and without the pilot injection. Downstream temperatures take longer to increase without a pilot injection, but it is important to note that the main injection timing without a pilot is advanced by 2 ° CA, so the initial temperature increases nearly overlap when plotted as a function of crank angle after TDC. Peak temperatures are comparable, and as is the case with upstream temperatures, it takes longer to reach the peak temperature without a pilot injection. As with the upstream temperatures, the falloff occurs at a similar rate in both cases. Upstream KL values increase later without a pilot injection, but are higher than those with a pilot for much of the combustion process. Only late during the combustion does KL decrease at a faster rate without a pilot injection, so KL values are lower without a pilot injection during the latest stages of combustion. Downstream KL values without a pilot injection begin their increase later, but eventually exceed the values with a pilot injection. Peak KL values without a pilot injection are approximately 25% higher than is the case with a pilot injection, but the decline in KL values at the end of combustion is similar for both cases, particularly considering that the main injection is advanced by 2 ° CA without the pilot injection. Even without the fouling correction, the maximum KL is higher without a pilot injection than it is with a pilot injection, so this phenonemon is certain to occur. The measured engine-out specific soot emissions are slightly higher for the case without a pilot injection, which may be counterintuitive, but coincide with the higher amount of measured in-cylinder soot.

Particularly during the earlier stages of combustion, the lift-off lengths appear to be shorter with the pilot injection (see Figure 4-24), which indicates that less mixing may take place. Furthermore, the gas that is entrained is normally air, but with a pilot injection, the possibility exists that post combustion gases are re-entrained. Both of these phenomena would lead to richer mixtures just downstream of the liquid tip, which would result in higher soot formation rates. This is believed to be the reason that upstream KL values increase much sooner after the start of the main injection with a pilot injection. Shorter lift off lengths indicate that the combustion takes place closer to the injector tip, which may explain the higher upstream temperatures with a pilot injection at the beginning of the combustion. It is unclear why the upstream temperature decreases for a time after its first peak with a pilot injection. Without the pilot injection, lift-off lengths appear to be longer at the onset of the quasi-steady phase of combustion (see Figure 4-24), but they are observed to become increasingly shorter. The amount of premixing in the spray jet becomes less with time, and soot formation increases in the upstream region. This is supported by the higher upstream KL values without a pilot and explains why the upstream temperatures without a pilot increase continuously until they reach their maximum. The higher downstream KL values without a pilot injection are also attributed to these decreasing lift-off lengths. Because the combustion without a pilot injection is advanced by 2 ° CA, soot can be better oxidized in a hotter environment, and downstream KL values decrease at a very similar rate for both cases. Late during the combustion, a slightly more pronounced “hump” in the downstream KL values is observed for the case without a pilot injection, which may also contribute to the slightly higher measured engine-out soot emissions. The cause of this hump is unknown, and there are no corresponding features observed in the flame temperature traces.

4.5. Comparison of E10W10 and Diesel

Previous investigations in a single cylinder, heavy duty engine have demonstrated potential for significant reductions in engine-out NO_x and soot through the use of Diesel-ethanol-water emulsions [140]. In particular, a macroemulsion of 10 vol% ethanol, 10 vol% water, and 80 vol% Diesel fuel (referred to here as E10W10) showed the strongest emission reduction potential of the blends that were tested. In combination with EGR, NO_x emissions could be reduced even further without substantial increases in soot formation. In this work, the mechanisms responsible for this behavior are investigated. The behavior of the premium Diesel fuel is compared with the behavior of E10W10 macroemulsion; some data about these fuels are given in Table 4-3.

Table 4-3: Comparison of premium Diesel fuel and E10W10

	Diesel	E10W10	
H/C atomic ratio	1.87	2.16	-
O/C atomic ratio	0	0.14	-
Density	831	843	kg/m^3
LHV	43	36.4	MJ/kg
Cetane number	57	n.A.	-
AFR_s	14.6	12.4	kg/kg

For Diesel fuel, the cetane number was obtained from an analysis of the fuel; such an analysis was not available for E10W10. The density of E10W10 is slightly higher than that for Diesel fuel, but its mass-based energy content is significantly lower. This means that a larger mass of E10W10 must be injected to achieve a given load, and more momentum exchange between the fuel and the in-cylinder gases will take place. The enthalpies of vaporization of ethanol and water are significiantly larger than for Diesel fuel (approximately 310% and 840% of the enthalpy of vaporization of Diesel fuel, respectively [141,142]), which means more sensible enthalpy will be required of the entrained air to heat the fuel to its ignition temperature, and temperatures at the start of combustion will likely be lower. Furthermore, the stoichiometric air-fuel ratio (AFR_s) is smaller for E10W10. As a result, for a given amount of air entrainment, the resulting mixture will be leaner for E10W10, which will have significant effects on the ensuing combustion and soot formation processes.

To facilitate comparison of the soot formation processes for these two fuels, the RAYLIX measurement technique was applied for the first time in the combustion chamber of the engine. For reasons described in 4.1.1, this first application was only possible at the low load operating point. The fueling parameters (injection pressure, injection timings, and injection durations) were held constant for this low load point, so the $IMEP_n$ with E10W10 was 0.13 MPa, which is 87% of the $IMEP_n$ with Diesel fuel. Furthermore, EGR rates of 15% and 30% were investigated with both fuels. For these cases, the intake and exhaust pressures were slightly altered as the EGR valve was opened, but intake temperatures were held to the temperature range given for the baseline case in Table 4-1. Cylinder pressure traces for both fuels with EGR rates of 0% and 30% are shown for the sake of comparison in Figure 4-26.

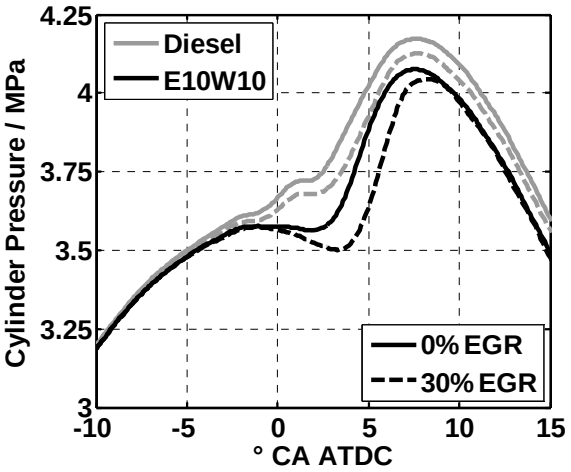

Figure 4-26: Cylinder pressure traces for the low load operating point with Diesel fuel and E10W10; traces with 30% EGR are displayed as dashed lines

It is apparent that the behavior of the combustion is significantly altered through the use of E10W10, particularly during the early stages of combustion. While a distinct pressure increase attributed to the combustion of the pilot injection is visible with Diesel fuel, such an increase is not observed with E10W10. The combustion with E10W10 is significantly delayed and the combustion of the pilot injection appears to be suppressed to a large extent. For this operating point, EGR delays combustion; this is associated with the lower oxygen concentrations that result from EGR.

Ethanol, like other simple alcohols, is known in the field of HCCI research for its ignition inhibition qualities [141, 143, 144, 145]. Chemical kinetics simulations performed in these works indicate that ethanol consumes hydroxyl radicals that are important for cool flame reactions of the hydrocarbon base fuel. Two important reactions for the consumption of OH radicals have been identified, eg. by [145]:

$$CH_3CH_2OH + \cdot OH \rightarrow CH_3CH_2O\cdot + H_2O \quad (4.4)$$

$$CH_3CH_2OH + \cdot OH \rightarrow CH_3CH\cdot OH + H_2O \quad (4.5)$$

Experimental results with ethanol directly injected into the cylinder of an HCCI engine show that rates of heat release for premixed, homogeneous combustion are decreased for the cool flame reactions and retarded and increased for the high temperature reactions [141]. In the case of E10W10, it is not known to what extent the presence of water in the fuel inhibits reactions 4.4 and 4.5. However, as discussed in [143], water doesn't affect cool flame chemistry, but it reduces the intensity of the low temperature oxidation reactions because of its high enthalpy of vaporization. This leads to decreased rates of high temperature heat release, as well. Ignition delays were also shown in [146] to increase through the use of a Diesel-water emulsion. To summarize, the higher heats of vaporization of ethanol and water, combined with the hydroxyl-consuming characteristics of ethanol, lead to cooler pre-combustion temperatures and ultimately to retardation of the high temperature heat release.

For the low load operating point, normalized, indicated specific engine out soot emissions (as measured with the smoke meter) are computed and shown in Figure 4-27 for both fuels and EGR rates of 0%, 15%, and 30%.

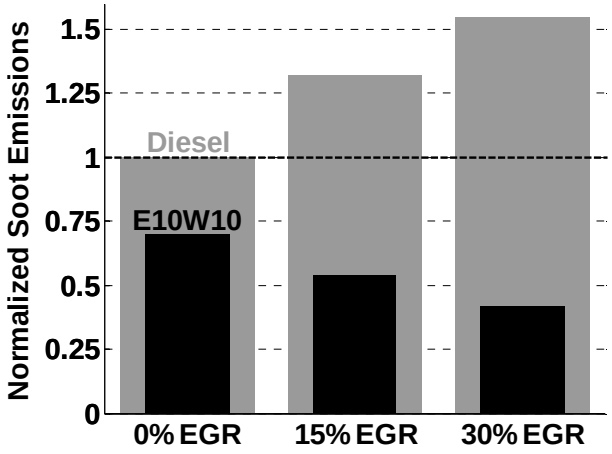

Figure 4-27: Normalized engine-out indicated specific soot emissions for Diesel fuel (gray) and E10W10 (black) with 0%, 15%, and 30% EGR

With Diesel fuel, soot emissions are observed to increase with increasing EGR rate, whereas with E10W10, soot emissions decrease as the EGR rate increases. This reasons for these differences in behavior are discussed below in 4.5.3.

For the part load operating point, an attempt was made to create similar thermodynamic conditions (pressure and, to a first approximation, temperature) for the beginning of the main injection for both fuels, so that the quasi-steady combustion process could be studied in more detail. This was accomplished by advancing the pilot injection by a crank angle of 3 ° compared to the baseline case (Table 4-3). The duration of the pilot injection was not changed, but the duration of the main injection was increased to maintain the same $IMEP_n$ for both fuels (see Table 4-2). The cylinder pressure traces for the part load operating point are shown with both fuels in Figure 4-28.

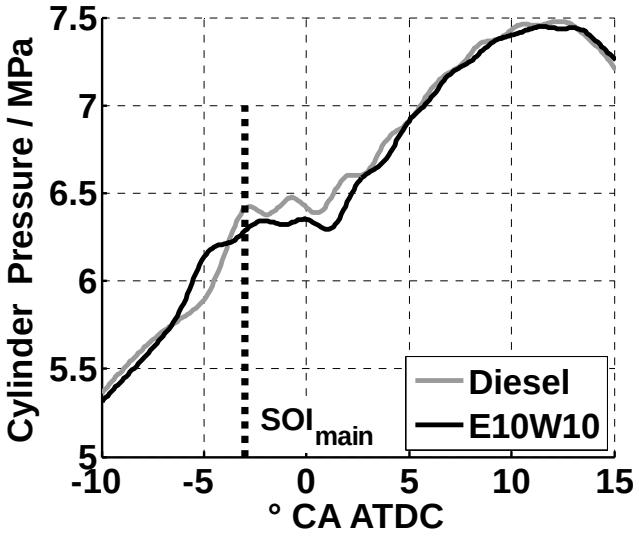

Figure 4-28: Cylinder pressure traces for the part load operating point with Diesel fuel and E10W10; the indicated start of the main injection is shown with a dotted line at 3 ° CA BTDC.

The advanced pilot injection with E10W10 is necessary due to its slower intial combustion behavior. This yields a main combustion event that behaves more like the operating point with Diesel fuel, as seen in the cylinder pressure trace. Without EGR, the reduction in engine-out specific soot emissions with E10W10 compared to Diesel fuel is 27%.

4.5.1. Mie Scattering

Musculus et al. show that with a Diesel-water emulsion of 20% water by mass, steady state penetration depths are significantly longer than with number 2 Diesel fuel [146]. In the case of a relatively low motored TDC temperatures, wall impingement was shown to occur with the 20%-water emulsion. Operation with E10W10 was not included in the Mie scattering investigations of the part load operating point. For the low load operating point, the Rayleigh scattering images taken during the RAYLIX investigations provide qualitative information about the differences in the penetration depth. For this, the raw elastic scattering images are ensemble averaged over 20 working cycles, and then thresholded with a threshold value of 12,000 counts. The averaged images are selected for each fuel with the furthest apparent liquid penetration depth, at the end of the injection event. The value of the threshold is more or less arbitrarily chosen, but does not affect the conclusions that can be drawn. The thresholded images are subtracted from one another to illustrate the differences in the fuel's maximum penetration depth. This composite image is shown in Figure 4-29; gray indicates the presence of a scattering signal for E10W10 in locations where no scattering signal for E10W10 is detected, and black indicates the presence of Diesel scattering in the absence of E10W10 scattering. The approximate locations of the cylinder head and the injector tip are shown with gray lines for reference.

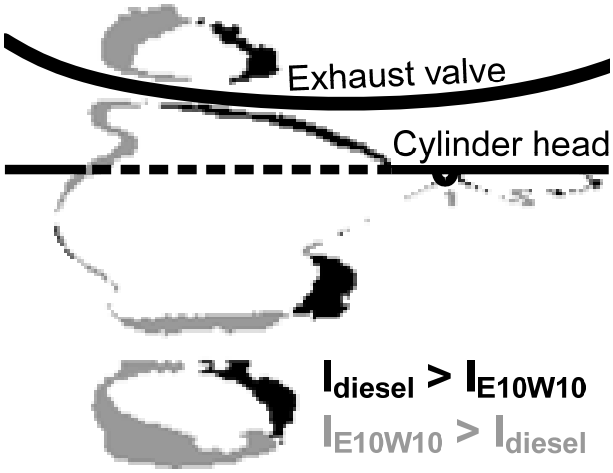

Figure 4-29: Composite thresholded images for Diesel fuel and E10W10, 1.1 ° CA $ASOI_I$; gray indicates the presence of an E10W10 scattering signal and the absence of a Diesel scattering signal; black indicates scattering with Diesel but not with E10W10

The interpretation of this particular scattering image is complicated by reflections (seen in Figure 4-29 as regions above and below the fuel jet on the left. Furthermore, blooming occurs in pixels where scattering intensity is high due to the presence of a dense liquid spray core. This manifests itself in the vertical direction, which prevents calculation of the jet spreading angle. However, for the low load operating point, practically no difference can be determined in the furthest downstream extents of the scattering signals. Although the wall of the piston bowl is not imaged, it can be stated that wall impingement does not occur for this low load operating point with a relatively short main injection duration. The causes for the differences in the scattering signals upstream of the tips of the scattering signal are unknown; the influence of signal disturbances makes this impossible to determine from these data. For the longer injection duration required for the part load operating point, differences in the quasi-steady liquid penetration depths may exist.

4.5.2. OH Chemiluminescence

For the part load operating point, radial logrithmic OH chemiluminescence intensity profiles are computed for five-cycle ensemble averaged images. The average of the profiles for angles of 180°, 182°, 184°, and 186° (as shown in Figure 4-5) is computed at 8 ° and 10 ° CA $ASOI_I$. These profiles are displayed in Figure 4-30 for both Diesel fuel and E10W10.

At a crank angle of 8 ° $ASOI_I$, significant differences are observed between the profiles for Diesel fuel and E10W10. The apparent lift-off length is substantially longer for E10W10. The longer ignition delays for the pilot injection likely mean that ignition occurs further downstream, and the inflammation of the main injection through interaction with the pilot injection mixture field is likely altered. The establishment of the quasi-steady phase of combustion is apparently delayed in comparison to operation with Diesel fuel. By 10 ° CA $ASOI_I$, the logarithmic radial intensity profiles are similar for Diesel fuel and E10W10.

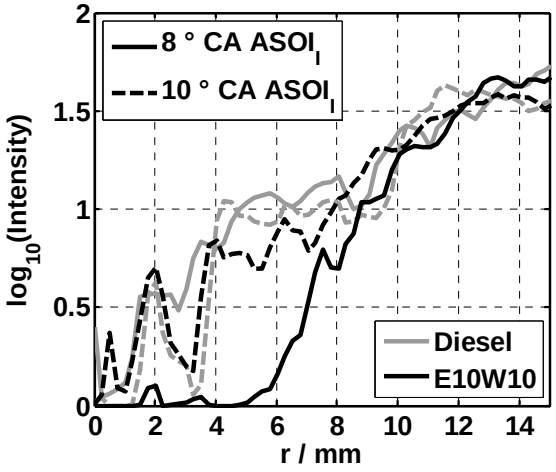

Figure 4-30: Averaged logarithmic radial intensity profiles for the part load operating point with Diesel fuel (gray curves) and with E10W10 (black curves)

For the quasi-steady phase of combustion, these results suggest that the air entrainment process is not significantly affected by the presence of ethanol and water in the fuel. If the air entrainment rates are indeed the same, then air fuel equivalence ratios at the lift-off length are expected to be leaner for E10W10. The expected consequence of this phenomenon is a reduction in soot formation rates with E10W10. Due to the differences in the transient behavior leading up to the quasi-steady phase of combustion, the two fuels are expected to exhibit differences in their soot formation processes. This is discussed below.

4.5.3. RAYLIX

Investigations with the low load point reveal the capabilities and limitations of the RAYLIX measurement technique in this practical combustion device. The small aperture afforded by the endoscope make high camera gain factors necessary, which negatively affects the signal to noise ratio. Scattering of the laser light by liquid fuel droplets makes interpretation of the Rayleigh scattering signal difficult early during the combustion process. Furthermore, high concentrations of soot are believed to form in the spray jet and are high enough to attenuate the incident laser light, thus rendering the measurement technique unable to provide information for much of the combustion process. This phenomenon is well documented in the literature for commercial-grade Diesel fuels. Raw Rayleigh scattering and LII images are shown in Figure 4-31 for one measurement taken at a crank angle of 6.8 ° ASOI$_l$. Two distinct regions can be identified in the Rayleigh image; it is non-linearly scaled as the more upstream region is much brighter. This brighter scattering is attributed to Mie scattering by the liquid fuel droplets. Because the downstream region is similar to the appearance of the downstream region in the LII image, the scattering is attributed to soot particles and is thus likely in the Rayleigh scattering regime. The LII image indicates that soot is distributed throughout the downstream portion of the jet and not simply at the edges, which agrees with the current understanding of Diesel combustion presented in Chapter 2.

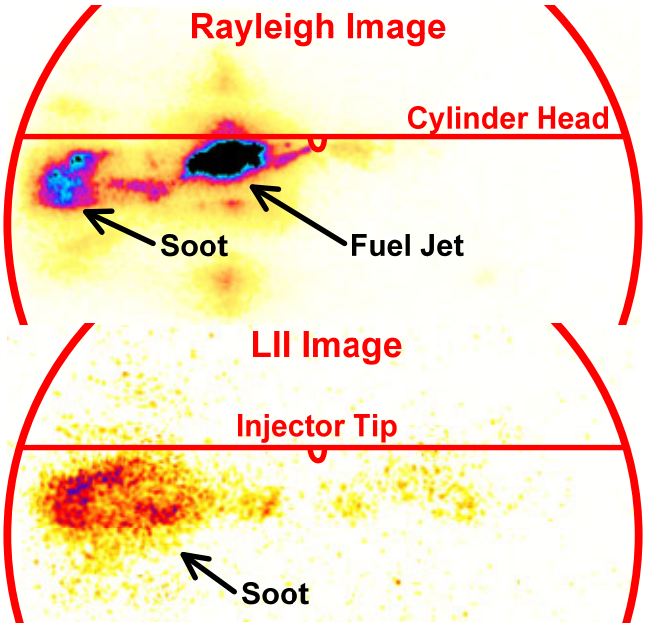

Figure 4-31: Single-shot raw Rayleigh and LII images (from the same measurement) with a non-linear, false color representation; imaged at 6.8 ° CA $ASOI_I$

These images are an example of a successful RAYLIX measurement. Because the soot cloud and the fuel jet are distinguishable, the LII signal can be used as a threshold to reliably mask the result images. At later crank angles, it is believed that some of the soot leaves the observation volume, which would make a quantitative analysis with the RAYLIX technique impossible. However, before this phenomenon can be observed, both signals cease to exist. This is attributed to attenuation of the laser light as described above. As a result of these limitations, complete RAYLIX measurements are possible for a brief crank angle window from approximately 6.8 ° CA $ASOI_I$ to 8 ° CA $ASOI_I$. At approximately 2.8 ° CA $ASOI_I$, the first LII signal appears, so some information about the soot formation processes can be obtained over a broader crank angle range. For this work, these measurements provide insights about the early soot formation processes for both Diesel fuel and E10W10.

In Figure 4-32, estimated mean particle diameters are shown for Diesel fuel and with E10W10 for EGR rates of 0, 15, and 30%. Each image is computed from an individual working cycle and is representative of the results obtained at 6.9 ° CA $ASOI_I$ for each operating point.

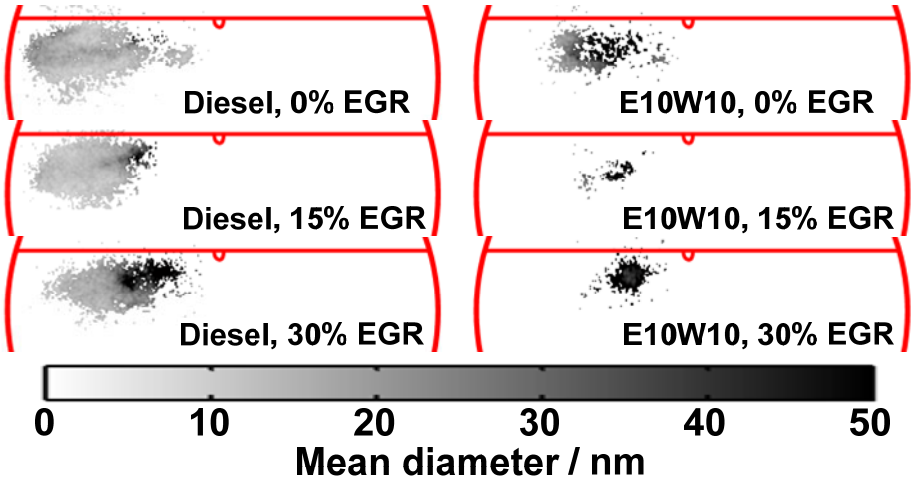

Figure 4-32: Individual cycle images of mean particle diameter for a crank angle of 6.9 ° CA $ASOI_I$; comparison between Diesel fuel and E10W10 for EGR rates of 0, 15, and 30%

As was the case with the raw LII image, it is observed that soot is distributed in the downstream portion of the jet with Diesel fuel. Soot particle diameters are between approximatey 10 and 20 nm, which indicates that the soot particles being measured here are primary particles. For Diesel fuel, the area over which soot can be measured decreases with increasing EGR rates. With E10W10, much less soot is observed at these early stages of combustion, such that the measurement system is at its detection limit. Interference with liquid fuel makes interpretation of the results extremely difficult, as very unrealistic particle sizes (> 50 nm) are calculated for many regions. It is possible that liquid fuel and soot particles exist in close proximity to one another, but this cannot be determined with this measurement technique. For the case of E10W10 with 15% and 30% EGR, the calculated results are essentially unusable. The presence of LII signal this close to the liquid fuel is unexpected; so for these cases it is uncertain if what is being measured is truly soot. One potential source of uncertainty could be that the laser causes some PAH species to fluoresce, which would be imaged as part of the LII measurement and falsely interpreted as an LII signal. Larger aperture optics should enable the LII imaging window to be temporally shifted to approximately 15-20 ns after the laser pulse, which should significantly reduce the fluorescent interference with the incandescence signal [147].

Particle volume fractions are computed and displayed in Figure 4-33 for the same working cycles shown in Figure 4-32. At this early stage of soot formation, concentrations are typically very low, on the order of several ppm. Here too, significant differences are observed between the two fuels. Concentrations for E10W10 are lower and much less soot is formed.

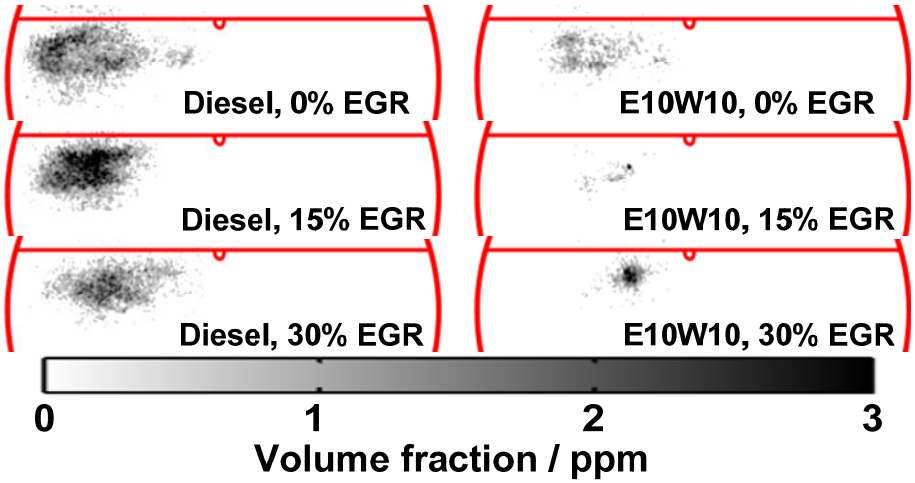

Figure 4-33: Individual cycle images of particle volume fraction for a crank angle of 6.9 ° CA ASOII; comparison between Diesel fuel and E10W10 for EGR rates of 0, 15, and 30%

Because the LII signal is available over a wider crank angle range and is much less susceptible to problems with scattered light from liquid fuel droplets, it is used to compute volume fraction images for all of the measurements taken. For each pixel of each image, the volume fraction is multiplied by the volume represented by one pixel, and the sum of all pixels is computed for each image. This sum represents the total volume of soot measured in the observation volume for each image. It is not weighted by the distance from the spray axis, so it may not accurately portray the total amount of soot found in the jet. This step is not necessary to see the significant differences that exist between Diesel fuel and E10W10. The median soot volumes for each imaged crank angle, fuel, and EGR rate are shown in Figure 4-34.

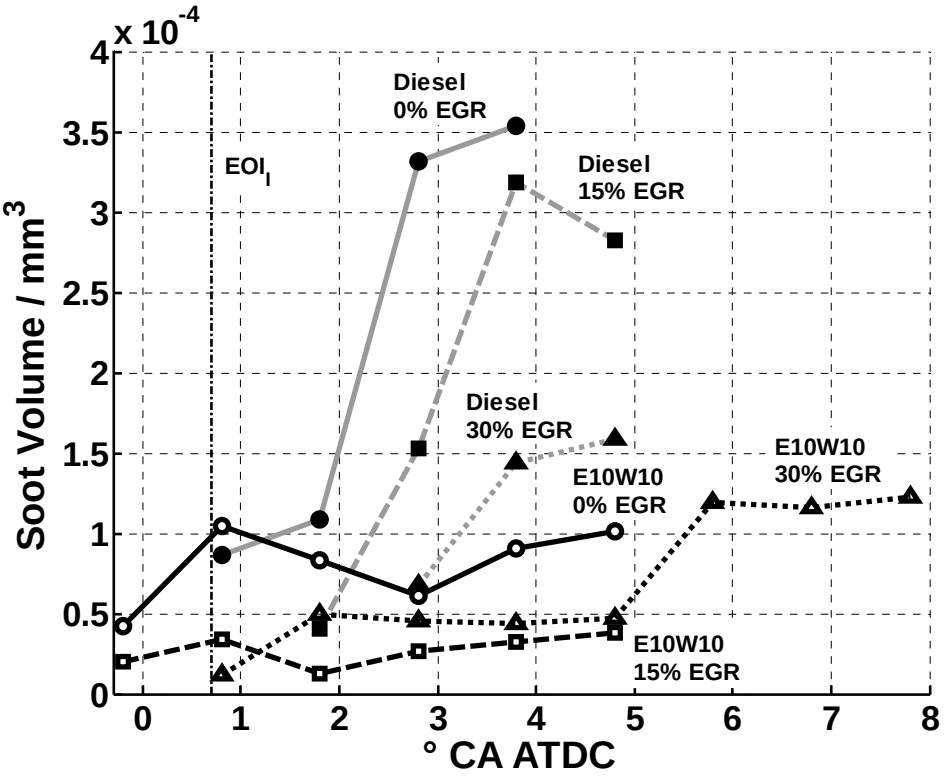

Figure 4-34: Soot volume in the measurement volume as a function of crank angle for Diesel fuel (gray lines) and E10W10 (black lines) for different EGR rates: 0% EGR (solid lines), 15% EGR (dashed lines), and 30% EGR (dotted lines)

With Diesel fuel, EGR is observed to delay the onset of observable soot formation and to decrease soot formation rates early in the soot formation process. This agrees with results measured in diffusion flames under much more highly controlled conditions [148]. In [148], the authors discuss the reasons for this behavior. The decreased oxygen concentrations and higher inert gas fractions associated with EGR decrease combustion temperatures. Therefore, the rates of endothermic soot formation reactions (see Chapter 2) are also slowed. Increased CO_2 concentrations are also associated with EGR; this leads to an increase in OH radicals via the equilibrium shift of the following reaction:

$$CO + \cdot OH \leftarrow\rightarrow CO_2 + H \qquad (4.6)$$

The presence of water vapor in a diffusion flame has been shown to effectively inhibit soot formation via the following reaction [149]:

$$H_2O + H \rightarrow \cdot OH + H_2 \qquad (4.7)$$

The additional OH radicals reduce concentrations of soot precursors and thus suppress soot formation. Also, water plays a role in the HACARC mechanism of soot formation [60]; it consumes radical sites and suppresses soot particle surface growth.

As shown in Figure 4-27, engine-out soot emissions are observed to increase with increasing EGR rates. Because the rates of soot formation early during the soot formation process are hindered by EGR, the oxidation reactions must be hindered to a larger extent so that more soot exists in the cylinder after the combustion has finished.

The beginning of soot formation, as indicated by the initial detection of an LII signal, occurs earlier with E10W10 than with Diesel fuel. As was the case with Diesel fuel, EGR delays the onset of measurable soot formation. However, the amounts of soot that are measured are at the system's detection limit and are very low for all EGR rates. They remain low and for the

case with E10W10 and 30% EGR, the amount of soot in the observation volume can be measured until nearly 8 ° CA $ASOI_I$.

As mentioned above, water vapor plays a role to suppress soot formation via several mechanisms. In the emulsion, water reduces the stoichiometric air-fuel equivalence ratio, so that for a given amount of air entrainment, the mixture is leaner. Its high heat capacity requires more sensible enthalpy from the air to heat the fuel to the point of ignition. Ethanol also reduces the fuel's stoichiometric air-fuel ratio and has a higher heat capacity than Diesel fuel. If a larger amount of air is required to heat the E10W10 to its ignition temperature, then this would suggest that combustion takes place further downstream after enough entrainment mixing and heating has occurred to sustain the combustion reactions. Figure 4-30 indicates that this is the case at least early during the combustion event. As discussed above, ethanol inhibits low temperature chemistry and thus delays high temperature ignition by consuming OH radicals, thereby increasing the time available for mixing. The combination of more air required to heat the fuel, lower stoichiometric air-fuel ratios, and longer ignition delays for E10W10 mean that conditions downstream of the liquid jet are likely leaner than for Diesel fuel, which would also likely lead to decreased soot formation rates. As demonstrated in [150], combustion of ethanol and other oxygenates leads to reduced production of PAHs and soot precursors when compared to a typical, non-oxygenated hydrocarbon fuel. The discussion of soot formation in Chapter 2 makes clear that soot formation mechanisms are strongly dependent on fuel chemistry, so these kinds of differences are not unexpected. These factors combine so that the soot production rates for this low load operating point are very low with E10W10. Increasing the EGR rate likely suppresses soot formation reactions to a larger extent, so that even with the poor conditions for oxidation, less soot is emitted. Thus, the engine-out soot emissions decrease with increasing EGR rates for E10W10.

4.5.4. Two Color Method

Two color pyrometry was applied to the part-load operating point to gain more insight about the different soot formation processes with Diesel fuel and E10W10. In Figure 4-28, the start of the main combustion as indicated by the start of pressure rise after TDC occurs slightly earlier for Diesel fuel than for E10W10. The maximum intensity of the data averaged raw images (in this case, the images taken at a central wavelength of 700 nm) provides information about the start of measurable soot. These maximum intensities are shown as functions of crank angle for both Diesel fuel and E10W10 in Figure 4-35.

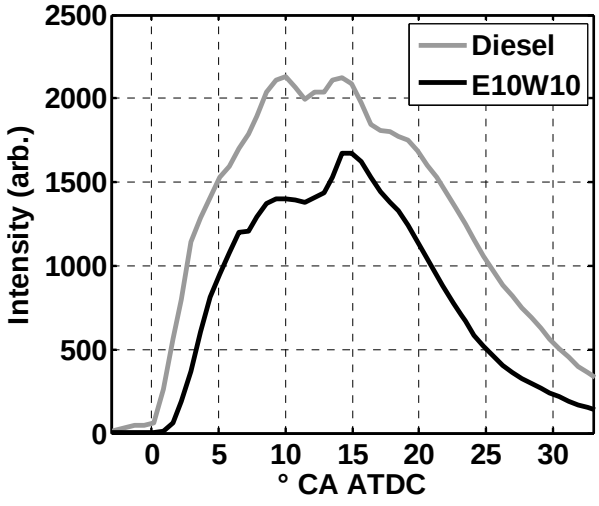

Figure 4-35: Maximum data-averaged soot luminosities (measured through the 700 nm bandpass filter) for Diesel fuel (gray) and E10W10 (black) as functions of crank angle for the part load operating point.

In agreement with the pressure increases associated with the main combustion, the maximum intensity for Diesel fuel begins to increase before that of E10W10. Small amounts of measurable soot are detected even before TDC with Diesel fuel, and the maximum intensity is always higher for Diesel fuel. This is a different behavior than was observed with the soot volume measurements for the low load operating point (see 4.5.3), where measurable soot was detected sooner for E10W10. However, the intensity measured in one image is not simply a function of the amount of soot contained in a given observation volume, but also its temperature. A direct comparison of the soot volume measured in a planar observation volume with integrated line-of-sight luminosities is of limited value. Instead, the soot temperatures and KL values are calculated and plotted in Figure 4-36 for the upstream and downstream regions shown in Figure 4-10.

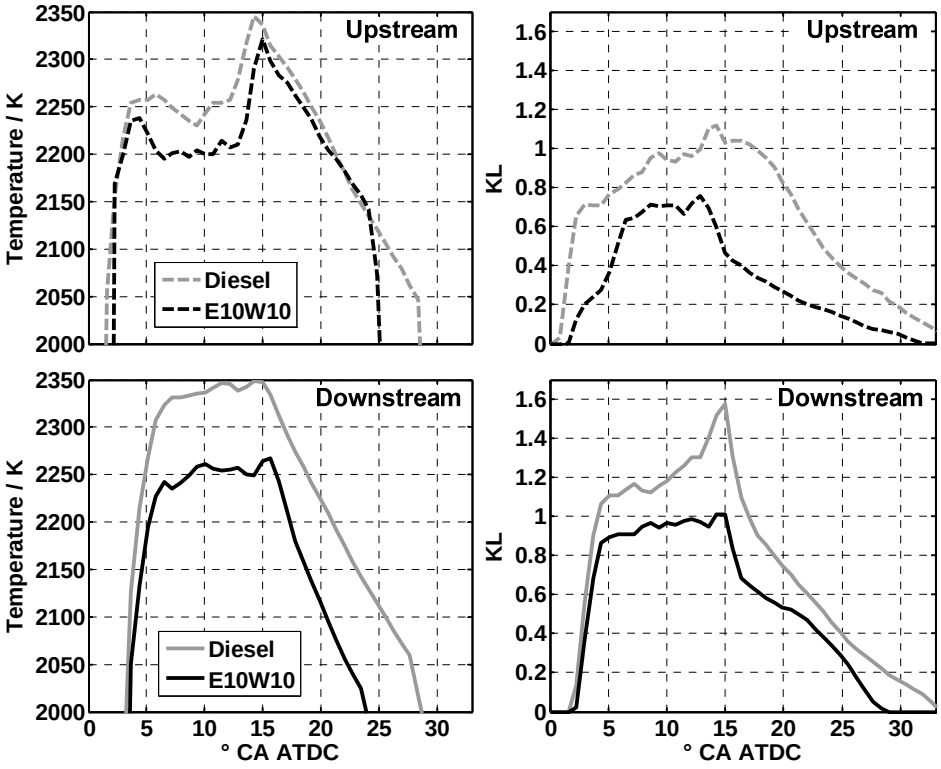

Figure 4-36: Mean, data averaged (over 20 working cycles) temperature and KL profiles in the downstream and upstream regions for the part load operating point with Diesel fuel (gray lines) and E10W10 (black lines)

The differences in combustion temperatures with Diesel fuel and E10W10 are different for the upstream and downstream regions. Upstream temperatures increase similarly for both fuels, but reach different values during the quasi-steady phase of combustion. Temperatures in the upstream region are approximately 50 K lower for E10W10 than for Diesel fuel. However, the injection duration is longer for E10W10 (to compensate for the fuel's lower energy content) and the large upstream temperature increase associated with the enhanced air entrainment after the end of the injection occurs later. Upstream temperatures decline at similar rates for both fuels, but after approximately 24 ° CA ATDC, the temperature for E10W10 falls off much more rapidly. With E10W10, upstream KL values increase at a slower rate, reach significantly lower peak values, and reach a value of zero faster at the end of combustion. The upstream KL differences are largest particularly during the late phases of combustion. The differences in the downstream temperatures are larger than the differences in

upstream temperatures. The downstream temperatures for E10W10 first increase at a slower rate than for Diesel fuel, and the quasi-steady temperatures are between 50 K and 100 K lower with E10W10. Temperatures with E10W10 remain lower for the remainder of the combustion despite the longer injection durations necessary with E10W10. After the end of injection, upstream temperatures with E10W10 become higher than the downstream temperatures, which is not the case with Diesel fuel. KL values for Diesel fuel increase during the quasi-steady stage of combustion and after the end of injection, but the magnitude of this increase is much smaller for E10W10. The KL values for E10W10 decrease at a similar rate for E10W10, but because the peak KL values are so much lower for E10W10, they reach the value of zero much sooner than for Diesel fuel.

To help understand what can be responsible for these temperature differences, the adiabatic flame temperatures have been calculated for n-heptane (used in place of Diesel fuel) and a mixture of n-heptane, 10 vol% ethanol, and 10 vol% water using the STANJAN equilibrium code [151]. The starting pressure was taken to be constant at 6.3 MPa and the starting temperature was estimated with a polytropic compression (polytropic exponent: 1.36) to be 722 K. These are plotted as a function of the air-fuel equivalence ratio (λ) in Figure 4-37.

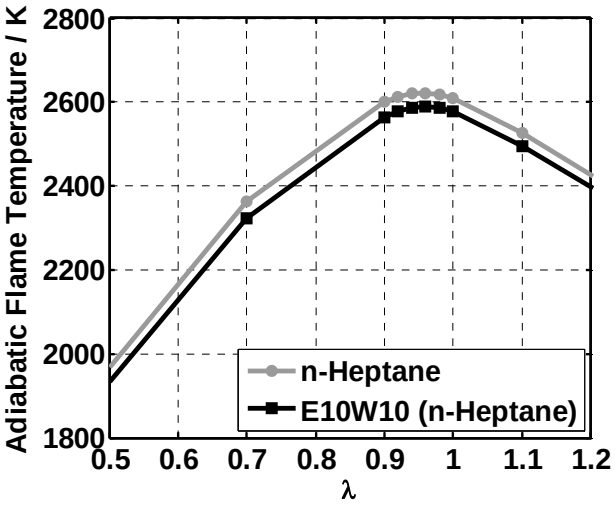

Figure 4-37: Adiabatic flame temperatures for n-heptane and an E10W10 mixture with n-heptane as a function of λ

The adiabatic equilibrium flame temperatures represent the highest theoretical combustion temperatures (without taking non-equilibrium effects into account) for a given value of λ and a given starting temperature. For n-heptane, adiabatic flame temperatures are typically between approximately 35 and 40 K higher than for the E10W10 mixture with the same value of λ and starting temperature. Measured temperature differences larger than this are most likely the result of either differences in the starting temperatures or of differences in the stoichiometry.

Differences in combustion temperatures between Diesel fuel and E10W10 are expected for the following reasons.

- The higher heats of vaporization of ethanol and water require more sensible enthalpy to be heated to the fuel's ignition temperature; mixing and vaporization in the upstream portion of the jet is likely to reflect this. For a given amount of entrained air, the temperature of the E10W10-air mixture before combustion will be lower, thus decreasing combustion temperatures.

- The aforementioned ignition inhibiting qualities of ethanol and the longer initial lift-off lengths (see Figure 4-30) suggest that at least some of the combustion takes place further downstream than with Diesel fuel. Thus, any heating provided by the combusting fuel would have less of an effect on the upstream region with E10W10.
- Equations 4.1 and 4.2 can be used to estimate the difference in the fuel mass flow rate between the Diesel and E10W10; it is less than 1%. If the same mass of air is entrained for both fuels (inspection of equations 4.1 and 4.3 reveals that the air entrainment mass flow rate is independent of fuel density), then the air-fuel equivalence ratio for E10W10 is closer to stoichiometric, so temperatures would tend to be higher. This counteracts the lower temperatures that result from the E10W10 vaporization process, but is apparently not the dominating factor.
- Adiabatic flame temperatures are lower with E10W10. If the diffusion flames occur at the locations at which the air-fuel equivalence ratios are the same for both fuels, then the temperatures for E10W10 will be accordingly lower.

Downstream temperatures with E10W10 are typically approximately 50 K hotter than the upstream temperatures, whereas with Diesel fuel this difference is closer to 70 K. The effects mentioned above are believed to contribute to this.

The lower upstream and downstream soot KL values for E10W10 can be explained by the factors described in 4.5.3. The downstream KL values do not show a strong increase associated with the end of injection as is seen with Diesel fuel. During this phase, upstream temperatures rapidly increase by more than 100 K for E10W10, and reach values higher than the maximum downstream temperature. The upstream temperatures with Diesel fuel never exceed the maximum downstream temperature, which suggests that the nature of the entrainment that occurs after the end of injection may different for E10W10. The higher density of E10W10 may increase the intensity of this late entrainment, as it is somewhat dependent on the density of the fuel. This would mean that this last stage of combustion takes place under leaner conditions than with Diesel fuel. Upstream KL values decrease more significantly with E10W10 during this stage, which indicates that soot oxidation rates are faster than formation rates. This too may be explained by leaner conditions caused by more intensive air entrainment. This is a significant difference between the two fuels and may be part of an important mechanism that is responsible for the lower engine-out soot emissions that are made possible by E10W10. During the late phase of combustion, the rates of decrease of KL values do not exceed the rates of KL decrease that are observed with Diesel fuel, which suggests that fuel-specific differences contribute less in the late stages of combustion and soot burn out.

5. Summary and Outlook

As Diesel engines continue to be widely used and developed, the reduction of engine-out pollutants remains an important research topic. This requires an understanding of the impact of the pollutants that are formed and the mechanisms responsible for their formation in the combustion chamber, but also of the extremely complex and dynamic Diesel combustion process.

The complex combustion processes in a modern heavy duty Diesel engine with direct injection remain the subject of research activities, and can be summarized as follows: liquid fuel is injected at high pressures into a hot, dense environment near top dead center. The liquid fuel must be atomized, vaporized, and mixed with the hot air, whereby the hot entrained air heats the fuel to its autoignition temperature. The fuel that is injected before ignition occurs reacts rapidly after the autoignition reactions have started. Soon, a lifted turbulent diffusion flame forms around each spray plume. The fuel that continues to be injected and heated by mixing with air reacts just upstream of the tip of the liquid spray, but sufficient air entrainment has not occurred to enable complete combustion of the fuel-air mixture. The products of this rich premixed reaction propagate downstream into the oxygen-poor center of the combustion plume. Here, the thermochemical environment is well-suited for soot formation and growth. These products of the rich, premixed reaction zone are consumed in the thin diffusion flame front that forms at the periphery of the plume, where mixing with air leads to a near-stoichiometric flame front. The high temperatures in this flame front are effective at oxidizing soot but also lead to the production of NO_x. The combustion products are mixed with the cooler, unburned gas, which can potentially freeze pollutant concentrations at levels above their equilibrium values. Soot is deposited on combustion chamber walls and some of this likely appears later in the exhaust after it desorbs during the blowdown process. During the combustion, the piston moves down in its working stroke and the temperatures and pressures inside the cylinder decrease as work is extracted from the gas. This reduces the likelihood of the last pockets of soot being oxidized and thus contributes to engine-out soot emissions.

Unburned hydrocarbons and carbon monoxide form under conditions in which oxidation cannot be completed, typically due to overleaning or quenching. These pollutants gain importance as highly diluted, low temperature combustion systems are developed.

The mechanisms responsible for soot formation are extremely complex. Pyrolysis and decomposition of the fuel in an oxygen-poor environment leads to the formation of aromatic and small polyaromatic hydrocarbons (PAH). These steps are highly reversible and strongly dependent on fuel chemistry and local stoichiometry. Growth of these PAHs is modeled as a polymerization process that involves the repeated abstraction of hydrogen atoms to create radical sites, followed by the addition of carbon in the form of acetylene to close newly formed rings. As the PAHs grow, they also collide with one another and stick together. In this way, the first particle nuclei are formed by coagulation of PAHs. Particle growth continues via coagulation, but also via surface growth and agglomeration. Surface growth occurs either through PAH condensation or acetylene addition, and is responsible for the majority of soot mass addition. Agglomeration occurs when these primary particles collide and stick together without changing shape. The complex structure and size of these agglomerates depends on the thermochemical environment to which the particles are exposed. Oxidation of soot particles can occur at every step in the process, and is temperature dependent. OH radical attack is largely responsible for soot oxidation at higher temperatures, whereas oxidation with O_2 becomes more important at lower temperatures.

Nitric oxide (NO) can form by a multitude of mechanisms, but for conventional Diesel combustion systems, the thermal mechanism is of primary importance. This mechanism involves reactions between molecular oxygen and nitrogen molecules, molecular nitrogen and oxygen molecules, and molecular nitrogen with hydroxyl radicals. It is dependent on the temperature and the fuel-oxidizer ratio, with the highest formation rates occurring with mixtures that are slightly lean of stoichiometric, as temperatures are high and excess oxygen is available.

Modern heavy duty engines employ a variety of technologies in order to meet emissions regulations. These often include multistage turbocharging, common rail fuel injection systems with maximum injection pressures in excess of 2000 bar, and extensive exhaust gas aftertreatment systems. Aftertreatment systems are typically comprised of an oxidation catalyst, a Diesel particulate filter, one or more SCR catalysts, and ammonia slip catalysts. The development of these systems is highly integrated with the engine control strategy. These systems are complex and costly, create packaging problems, and are detrimental to fuel economy. State-of-the-art Diesel combustion research continues with highly diluted, heavily boosted operation to increase lift-off lengths for the purpose of reducing or eliminating soot formation. This proves to be challenging and the benefits come at the price of very high mechanical stresses and increased pumping losses.

The first goal of this work was to develop and build a new, optically accessible, heavy duty Diesel engine. A design with three flat, circumferentially positioned optical accesses (two in-line laser accesses and one orthogonal observation access) was successfully implemented. Following this, a set of optical diagnostic techniques was developed for application in the combustion chamber of the new optical engine. These included:

- A Mie backscattering technique for the observation of liquid-phase fuel
- The RAYLIX measurement technique to provide planar images of mean particle diameters and concentrations
- An OH chemiluminescence imaging technique to provide information about the first locations of near-stoichiometric combustion and lift-off lengths
- A two color pyrometric imaging technique to provide spatially resolved information about flame temperatures and soot extinction

This work represents the first application of the RAYLIX technique in the combustion chamber of a Diesel engine. It is a combination of planar Rayleigh scattering, planar laser induced incandescence, and total extinction. The OH chemiluminescence technique represents a significant improvement in terms of spatial resolution and optical aperture in comparison to previously applied endoscopic techniques. An image-splitting optical relay and comprehensive image processing software were specially developed to process the pyrometric imaging data and provide flame temperature and soot KL images. This set of optical diagnostic tools is by no means complete, but provides significant information about many aspects of the combustion and soot formation and oxidation processes.

In the course of the development of these techniques, two engine operating points were considered: a naturally-aspirated, low load point; and a boosted part load operating point. The low load point was specifically developed for the application of the RAYLIX technique with Diesel fuel. Measurements at part load provide more significant information about the quasi-steady phase of the combustion, so a variety of parameter variations was performed with this operating point.

For the part load operating point, liquid penetration depths are measured to be on the order of 11 to 15 mm. Furthermore, these penetration depths are observed to decrease as the combustion process progresses. This retraction is attributed to heating by the combustion process, which leads to faster vaporization of the liquid fuel. Quantitative measurement of the lift-off lengths via the OH chemiluminescence imaging techniques is not yet possible, but the results obtained in this work suggest that lift-off lengths are typically shorter than the liquid penetration depths, which is not unexpected for operation without EGR. Two color pyrometric imaging provides significant spatially and temporally resolved information. Flame temperatures are observed to be highest in the downstream region of the spray plume, which agrees with the current understanding of Diesel combustion. Temperatures in the upstream portion of the jet are approximately 70-80 K lower than in the downstream region, but increase dramatically as the injection process finishes. This behavior is attributed to enhanced air entrainment caused by the loss of momentum transfer by the high-velocity fuel jet. Fuel is vaporized more rapidly, so combustion can take place further upstream than during the quasi-steady phase of combustion. Soot KL values increase rapidly before the quasi-steady phase of combustion begins, but the rate of increase slows as the quasi-steady combustion commences. Downstream KL values are between 20 and 40% higher than the upstream values for the majority of the combustion, but after the end of injection, the upstream and downstream KL values are nearly the same as oxidation decreases the amount of soot in the cylinder. Temperature and KL data from individual working cycles provides insight into the phenomena responsible for the signal fluctuations that are typical of two color pyrometric data. These are shown to be related to phenomena that take place within the cylinder.

An increase in injection pressure is shown to effectively decrease engine-out soot emissions. Mie scattering and OH chemiluminescence imaging indicate that the increased injection pressure does not affect liquid penetration depths or flame lift-off lengths in a significant or systematic way. The lack of an effect on lift-off lengths does not agree with the results of other researchers. Improvements to the imaging technique are suggested to provide data with improved quality and resolution so that this phenomenon can be further investigated. Natural flame luminosity data indicate that the longer injection durations required to maintain a constant engine load lead to more soot being formed later during the working cycle, which means that oxidation likely takes place in a larger volume at lower temperatures. Here too, the continued development of the pyrometric imaging technique will provide more clarity.

The use of a pilot injection to decrease rates of cylinder pressure rise and thus combustion noise has significant effects on the inflammation and combustion of the main injection. OH chemiluminescence images provide evidence of direct interaction between the combusting mixture field of the pilot injection and the liquid fuel injected during the main injection. Without a pilot injection, a clear recession in lift-off lengths is observed as combustion progresses. Such a clear, systematic recession is not observed with a pilot injection. The trends in temperatures and KL values reflect the decreasing lift-off lengths and the corresponding richer premixed zone that are observed without the pilot injection. Higher KL values are observed without a pilot injection, particularly later during the combustion process. Because the injection timing is advanced without the pilot injection, this soot can apparently be effectively oxidized, and the net effect on engine-out soot emissions is relatively small.

Because operation with a macroemulsion of 10 vol% ethanol, 10 vol% water, and 80 vol% Diesel fuel (E10W10) showed strong potential for decreased engine out soot and NO_x emissions, Diesel combustion with E10W10 was examined optically. The energy content of E10W10 is nearly 17% lower than that of Diesel fuel, and its latent heat of vaporization is higher than for Diesel fuel. Finally, a stoichiometric mixture of E10W10 and air contains less air than a stoichiometric mixture of Diesel fuel and air. For a given amount of air entrainment

into a vaporizing fuel jet, the resulting mixture will be leaner with E10W10. For the low load operating point, the ignition inhibition characteristics of ethanol, coupled with the increased heat of vaporization for E10W10, suppresses combustion of the pilot injection and delays combustion of the main injection. For the part load operating point, the pilot injection was advanced to compensate for these effects and to create similar in-cylinder thermodynamic conditions for the main injection.

Indications from the Rayleigh scattering measurements are that the addition of water and ethanol to the fuel does not create a problem with wall impingement for the low load operating point, as the injection duration is relatively short. The OH chemiluminescence imaging results suggest that lift-off lengths may take longer to stabilize with E10W10, but significant differences in the quasi-steady lift off lengths are not observed with the part load operating point. This suggests that the air entrainment process is not significantly affected by operation with E10W10, but that the mixture in the premixed rich reaction zone is leaner with E10W10. The RAYLIX measurement technique could be successfully applied to the low load operating point. These measurement results indicate that soot formation rates are suppressed with E10W10, and engine-out soot emissions decrease more substantially with the use of EGR. The reaction of water with hydrogen atoms is believed to contribute to these lower soot formation rates as more hydroxyl radicals are formed. Water's role in consuming soot radical sites suppresses particle surface growth as well. While the use of EGR increases soot emissions with Diesel fuel, the engine-out soot emissions with E10W10 decrease with increasing EGR rates. It is hypothesized that the already low soot formation rates observed with E10W10 are suppressed to a greater extent with the use of EGR, so that the total amount of soot that is formed can easily be oxidized. Two color pyrometry measurements of the part load operating point show that combustion temperatures are much lower for E10W0 than for Diesel fuel, particularly in the downstream region. The increase in upstream temperatures with E10W10 is more substantial than for Diesel fuel, and accompanies a decrease in upstream KL values that is much more significant than is observed with Diesel fuel. This has important implications for engine-out soot emissions, as the rates of KL decrease are not necessarily higher for E10W10 during the burn out phase of combustion.

The further development and application of the measurement techniques presented in this work, as well as other optical techniques, will provide higher quality data that will enable more quantitative analyses (i.e. lift-off lengths). Collaboration with other research groups (such as the Engine Combustion Network [152]) will ensure that research continues on topics that are of interest to the combustion development community. The precise control of air-fuel premixing in a lifted, turbulent diffusion flame over the entire injection period inside a Diesel engine has been identified as the key to avoiding soot formation. The further development of advanced Diesel combustion systems may well focus on eliminating the necessity for one or more components of the exhaust gas aftertreatment system. In-depth knowledge of the underlying processes will be crucial to these endeavors. Optical measurement techniques that provide good temporal and spatial resolution, as well as quantitatively meaningful measurement results, will help the development of simulation tools necessary for a more complete understanding of such an advanced combustion system.

References

[1] Spicher, U., *Analyse der Effizienz Zukünftiger Antriebssysteme für die Individuelle Mobilität,* Motortechnische Zeitschrift (MTZ), Issue 2, pp. 98-105, 2012.

[2]*EU Transport in Figures: Statistical Pocketbook 2011*, European Comission; European Union, Luxembourg, 2011. doi:10.2832/47741

[3] Capros, P., Mantzos, L., Tasios, N., De Vita, A., Kouvaritakis, N., *EU energy trends to 2030: update 2009*, European Comission, Directorate-General for Energy, Luxembourg, 2009. doi:10.2833/21664

[4] *A Sustainable future for transport: Towards an integrated, technology-led and user-friendly system,* European Commission; European Communities, 2009. doi:10.2768/13118

[5] Bockhorn, H. (coordinator), *Collaborative Research Centre 606: Non-Stationary Combustion: Transport Phenomena, Chemical Reactions, Technical Systems.* Funding Proposal 1.1.2009-31.12.2012, German Research Foundation, August 2008.

[6] Busch, S., Kleindienst, M., Dahnz, C., Wagner, U., and Spicher, U. *Design and Flow Analysis of a Novel Optically Accessible Heavy Duty Diesel Research Engine.* ASME Conf. Proc. 2011., 837 (2011), DOI:10.1115/ICEF2011-60024.

[7] Busch, S., Spicher, U., *Untersuchungen der Zylinder-Innenströmung in einem optisch zugänglichen Heavy Duty Dieselmotor*, in "Innovative Automobiltechnik III: Zukunftsweisende Arbeiten von Nachwuchsforschern in der Industrie und an Universitäten." Tschöke, H., Krahl, J., Munack, A., ed. Cuvillier Verlag, Göttingen: 2012.

[8] Merker, G., Schwarz, C., Stiesch, G., Otto, F. *Verbrennungsmotoren, Simulation der Verbrennung und Schadstoffbildung.* 3rd ed. Teubner Verlag, 2006.

[9] Baumgarten, C., *Mixture Formation in Internal Combustion Engines.* Springer-Verlag, Berlin: 2006.

[10] Pischinger, S., Vorlesungsumdruck: Verbrennungsmotoren, Band II. Lehrstuhl für Verbrennungskraftmaschinen, Rheinisch-Westfälische Technische Hochschule Aachen, 2007.

[11] Baumgarten, C., *Modellierung des Kavitationseinflusses auf den primären Strahlzerfall bei der Hochdruck-Dieseleinspritzung.* VDI Fortschritt-Bericht, Reihe 12, Nr. 543, 2003.

[12] Espey, C. and Dec, J., *The Effect of TDC Temperature and Density on the Liquid-Phase Fuel Penetration in a D. I. Diesel Engine**, SAE Technical Paper 952456, 1995, doi:10.4271/952456.

[13] Wiartalla, A., *Untersuchung der Rußbildung bei der Dieselmotorischen Verbrennung in einer Modellbrennkammer.* Doctoral Thesis, Rheinish-Westfälischen Technischen Hochschule Aachen, 1995.

[14] Siebers, D., *Liquid-Phase Fuel Penetration in Diesel Sprays.* SAE Technical Paper 980809, 1998, doi:10.4271/980809.

[15] Taschek, M., *Einsatz qualitativer und quantitativer optischer Messverfahren an einem Diesel-Transparentmotor.* Doctoral thesis, Universität Erlangen-Nürnberg, 2007.

[16] Reynolds, W.C. *The Element Potential Method for Chemical Equilibrium Analysis: Implementation in the Interactive Program STANJAN.* Version 3, Stanford University, 1986.

[17] Kitamura, T., Ito, T., Senda, J., Fujimoto, H. *Mechanism of smokeless Diesel combustion with oxygenated fuels based on the dependence of the equivalence ratio and temperature on soot particle formation.* International Journal of Engine Research, Vol. 3, No. 4, 2002.

[18] Kook, S., Bae, C., Miles, P., Choi, D., Pickett, L. *The Influence of Charge Dilution and Injection Timing on Low-Temperature Diesel Combustion and Emissions.* SAE Technical Paper 2005-01-3837, 2005, doi:10.4271/2005-01-3837.

[19] Dec, J., Espey, C., *Chemiluminescence Imaging of Autoignition in a DI Diesel Engine.* SAE Technical Paper 982685, 1998, doi:10.4271/982685.

[20] Westbrook, C., *Chemical Kinetics of Hydrocarbon Ignition in Practical Combustion Systems.* Proceedings of the Combustion Institute, Vol. 28, pp. 1563-1577, 2000.

[21] Espey, C., Dec, J., *Planar Laser Rayleigh Scattering for Quantitative Vapor-Fuel Imaging in a Diesel Jet.* Combustion and Flame, Vol. 109. pp. 65-86, 1997.

[22] Higgins, B., Siebers, D., Aradi, A., *Diesel-Spray Ignition and Premixed-Burn Behavior.* SAE Technical Paper 2000-01-0940, 2000, doi:10.4271/2000-01-0940.

[23] Dec, J., *A Conceptual Model of DI Diesel Combustion Based on Laser-Sheet Imaging*.* SAE Technical Paper 970873, 1997, doi:10.4271/970873.

[24] Dec, J., Espey, C., *Ignition and Early Soot Formation in a DI Diesel Engine Using Multiple 2-D Imaging Diagnostics*.* SAE Technical Paper 950456, 1995, doi:10.4271/950456.

[25] Flynn, P., Durrett, R., Hunter, G., zur Loye, A., Akinyemi, O., Dec, J., Westbrook, C., *Diesel Combustion: An Integrated View Combining Laser Diagnostics, Chemical Kinetics, And Empirical Validation*. SAE Technical Paper 1999-01-0509, 1999, doi:10.4271/1999-01-0509.

[26] Dec, J., Coy, E., *OH Radical Imaging in a Diesel Engine and the Structure of the Early Diffusion Flame*.* SAE Technical Paper 960831, 1996, doi:10.4271/960831.

[27] Higgins, B. and Siebers, D., *Measurement of the Flame Lift-Off Location on DI Diesel Sprays Using OH Chemiluminescence.* SAE Technical Paper 2001-01-0918, 2001, doi:10.4271/2001-01-0918.

[28] Siebers, D. and Higgins, B., *Flame Lift-Off on Direct-Injection Diesel Sprays Under Quiescent Conditions.* SAE Technical Paper 2001-01-0530, 2001, doi:10.4271/2001-01-0530.

[29] Musculus, M., *Effects of the In-Cylinder Environment on Diffusion Flame Lift-Off in a DI Diesel Engine.* SAE Technical Paper 2003-01-0074, 2003, doi:10.4271/2003-01-0074.

[30] Dec, J. and Canaan, R., *PLIF Imaging of NO Formation in a DI Diesel Engine.* SAE Technical Paper 980147, 1998, doi:10.4271/980147.

[31] Musculus, M., *On the Correlation between NOx Emissions and the Diesel Premixed Burn.* SAE Technical Paper 2004-01-1401, 2004, doi:10.4271/2004-01-1401.

[32] Spicher, U., Velji, A., Huynh, H.N., Kruse, F., *Flammenausbreitung Dieselmotor II: Untersuchung der räumlichen Flammenausbreitung und der Strömungsvorgänge im Dieselmotor.* Abschlussbericht: FVV Vorhaben Nr. 367, Heft 424, 1988.

[33] Polonowski, C., Mueller, C., Gehrke, C., Bazyn, T., Martin, G., Lillo, P. *An Experimental Investigation of Low-Soot and Soot-Free Combustion Strategies in a Heavy-Duty, Single-Cylinder, Direct Injection, Optical Diesel Engine.* SAE Int. J. Fuels Lubr. 5(1):51-77, 2012, doi:10.4271/2011-01-1812.

[34] Wirths, M., König, G., Nording, K., Wenzel, P., Krüger, C., *Analyse der Erreichbarkeit niedrigster Rohemissionen am Heavy-Duty-Einzylindermotor anhand experimenteller und numerischer Untersuchungen,* 10th International Symposium on Combustion Diagnostics, Baden-Baden, 2012.

[35] Suhre, B. and Foster, D., *In-Cylinder Soot Deposition Rates Due to Thermophoresis in a Direct Injection Diesel Engine.* SAE Technical Paper 921629, 1992, doi:10.4271/921629.

[36] Dec, J., Tree, D. *Diffusion-Flame / Wall Interactions in a Heavy-Duty DI Diesel Engine.* SAE Technical Paper 2001-01-1295, 2001, doi:10.4271/2001-01-1295.

[37] Tree, D. and Dec, J., *Extinction Measurements of In-Cylinder Soot Deposition in a Heavy-Duty DI Diesel Engine.* SAE Technical Paper 2001-01-1296, 2001, doi:10.4271/2001-01-1296.

[38] Kent, J.H. and Wagner, H.Gg., *Why Do Diffusion Flames Emit Smoke?* Combustion Science and Technology, Vol. 41, pp. 245-269, 1984.

[39] Dec, J. and Kelly-Zion, P., *The Effects of Injection Timing and Diluent Addition on Late-Combustion Soot Burnout in a DI Diesel Engine Based on Simultaneous 2-D Imaging of OH and Soot.* SAE Technical Paper 2000-01-0238, 2000, doi:10.4271/2000-01-0238.

[40] *IARC: Diesel Engine Exhaust Carcinogenic.* International Agency for Research on Cancer, World Health Organization, press release No. 213, June 12, 2012.

[41] Raub, J., Mathieu-Nolf, M., Hampson, N., Thom, S., *Carbon monoxide poisoning – a public health perspective.* Toxicology, Vol. 145, pp.1-14, 2000.

[42] *Nitrogen Dioxide,* United States Environmental Protection Agency, Office of Air and Radiation, online: www.epa.gov/airquality/nitrogenoxides/, Dec. 10, 2012.

[43] Foust, R. *Photochemical Smog.* Lecture 40, Environmental Chemistry. Northern Arizona University, online: http://jan.ucc.nau.edu/~doetqp-p/courses/env440/env440_2/lectures/env440topics.html, Dec. 10, 2012.

[44] *Ozone - Good Up High Bad Nearby.* United States Environmental Protection Agency, Office of Air and Radiation. EPA-451/K-03-001, June 2003.

[45] ISO 23210:2009: *Stationary source emissions – Determination of PM10/PM2,5 mass concentrations in flue gas – Measurement at low concentrations by use of impactor,* 2009.*s*

[46] *Particulate Matter: National Summary of Particulate Matter Emissions.* United States Environmental Protection Agency, online: www.epa.gov/cgi-bin/broker?_service=data&_debug=0&_program=dataprog.national_1.sas&polchoice=PM, February 21, 2013.

[47] Nel, A., *Air Pollution-Related Illness: Effects of Particles,* Science Magazine, Vol. 308, pp. 804-806, May 6, 2005.

[48] Kampa, M., Castanas, E., *Human health effects of air pollution.* Environmental Pollution, Vol. 151, pp. 362-367, 2008.

[49] Oberdörster, G. and Utell, M., *Ultrafine Particles in the Urban Air: To the Respiratory Tract – And Beyond?* Environmental Health Perspectives, Vol. 110, Number 8, pp. A440-A441, August 2002.

[50] *Particulate Matter,* United States Environmental Protection Agency, Office of Air and Radiation, online: www.epa.gov/airquality/particlepollution/index.html, Dec. 10, 2012.

[51] Heywood, J., *Internal Combustion Engine Fundamentals*. McGraw-Hill, Inc., New York: 1988.

[52] Miles, P.C., Petersen, B.R., Sahoo, D., *Quantitative mixture preparation studies in late-injection Diesel combustion systems using Toluene LIF*. 10th International Symposium on Combustion Diagnostics, Baden-Baden, Germany, pp. 232-241, May 2012.

[53] Dryer, F.L and Glassman, I., *High-Temperature Oxidation of CO and CH_4.* 14th Symposium (International) on Combustion, Vol. 14, Issue 1, 1972.

[54] Private communication with Prof. Robert Dibble, October 4, 2011.

[55] McEnally, C., Pfefferle, L., Atakan, B., Kohse-Höinghaus, K., *Studies of aromatic hydrocarbon formation mechanisms in flames: Progress towards closing the fuel gap.* Progress in Energy and Combustion Science 32, 2006.

[56] Ebert, L., *Is Soot Composed Predominantly of Carbon Clusters?* Science 23, Vol. 247 no. 4949, pp. 1468-1471, March 1990.

[57] Lee, K., Cole, R., Sekar, R., Choi, M., Kang, J., Bae, C., Shin, H. *Morphological Investigation of the Microstructure, Dimensions, and Fractal Geometry of Diesel Particulates.* Proceedings of the Combustion Institute, Vol. 29, pp. 647-653, 2002.

[58] Zhu, J., Lee, K., Yozgatligil, A., Choi, M., *Effects of engine operating conditions on morphology, microstructure, and fractal geometry of light-duty Diesel engine particulates.* Proceedings of the Combustion Institute, Vol. 30, pp. 2781-2789, 2005.

[59] Frenklach, M. and Wang, H. *Detailed Modeling of Soot Particle Nucleation and Growth.* Twenty-Third Symposium (International) on Combustion / The Combustion Institute, pp. 1559-1566, 1990.

[60] Mauss, F., Trilken, B., Breitbach, H., Peters, N. *Soot Formation in Partially Premixed Diffusion Flames at Atmospheric Pressure.* In "Soot Formation and Combustion, Mechanisms and Models," Bockhorn, H., ed. Springer-Verlag, Berlin: 1994.

[61] Wang, H., *Formation of nascent soot and other condensed-phase materials in flames.* Proceedings of the Combustion Institute, Vol. 33, pp. 41-67, 2011.

[62] Howard, J., *Carbon Addition and Oxidation Reactions in Heterogeneous Combustion and Soot Formation.* Twenty-Third Symposium (International) on Combustion / The Combustion Institute, pp. 1107-1127, 1990.

[63] Frenklach, M. and Wang, H., *Detailed Mechanism and Modeling of Soot Particle Formation.* In "Soot Formation and Combustion, Mechanisms and Models," Bockhorn, H., ed. Springer-Verlag, Berlin: 1994.

[64] Harris, S. and Weiner, A., *Surface Growth of Soot Particles in Premixed Ethylene/Air Flames.* Combustion Science and Technology, 31:3-4, pp. 155-167, 1983.

[65] Tree, D. and Svensson, K., *Soot processes in compression ignition engines.* Progress in Energy and Combustion Science, Vol. 33, pp. 272-309, 2007.

[66] Harris, S. and Kennedy, I., *The Coagulation of Soot Particles with van der Waals Forces.* Combustion Science and Technology, Vol. 59, pp. 443-454, 1988.

[67] Neer, A. and Koylu, U., *Effect of operating conditions on the size, morphology, and concentration of submicrometer particulates emitted from a Diesel engine.* Combustion and Flame, Vol. 146, pp. 142-154, 2006.

[68] Pischinger, R., Klell, M., Sams, T., *Thermodynamik der Verbrennungskraftmaschine*. 2nd ed. Springer-Verlag, Vienna: 2002.

[69] Glassman, I., Nishida, O., Sidebotham, G., *Critical Temperatures of Soot Formation.* In "Soot Formation and Combustion, Mechanisms and Models," Bockhorn, H., ed. Springer-Verlag, Berlin: 1994.

[70] Haynes, B.S. and Wagner, H. GG., *Soot Formation*. Progress in Energy and Combustion Science, Vol. 7, pp. 229-273, 1981.

[71] Song, J., Alam, M., Boehman, A., Kim, U., *Examination of the oxidation behavior of bioDiesel soot.* Combustion and Flame, Vol. 146, pp. 589-604, 2006.

[72] Al-Qurashi, K., Boehman, A., *Impact of exhaust gas recirculation (EGR) on the oxidative reactivity of Diesel engine soot.* Combustion and Flame, Vol. 155, pp. 675-695, 2008.

[73] Bowman, C., *Control of Combustion-Generated Nitrogen Oxide Emissions: Technology Driven by Regulation.* Twenty-Fourth Symposium (International) on Combustion / The Combustion Institute, pp. 859-878, 1992.

[74] Busch, A., *Stoßwellenuntersuchungen zum Zerfall stickstoffhaltiger Verbindungen mit spektroskopischen Methoden.* Doctoral thesis, Karlsruhe Institute of Technology, 2010.

[75] Turns, S., *An Introduction to Combustion, Concepts and Applications.* 2nd ed., McGraw-Hill, Boston: 2000.

[76] Zeldovich, Y.B., *The Oxidation of Nitrogen in Combustion and Explosions,* Acta Physiochimica U.R.S.S., XXI, 1946.

[77] Warnatz, J., Maas, U., Dibble, R.W. *Combustion: Physical and Chemical Fundamentals, Modeling and Simulation, Experiments, Pollutant Formation.* 4th Ed. Springer-Verlag, Berlin: 2006.

[78] Lavoie, G., Heywood, J., Keck, J., *Experimental and Theoretical Study of Nitric Oxide Formation in Internal Combustion Engines.* Combustion Science and Technology, Vol. 1, pp.313-326, 1970.

[79] Fenimore, C.P., *Formation of Nitric Oxide in Premixed Hydrocarbon Flames.* Thirteenth Symposium (International) on Combustion, The Combustion Institute, Vol. 13, pp.373-380,1971.

[80] Moskaleva, L.V. and Lin, M.C., *The Spin-Conserved Reaction CH + N2 → H + NCN: A Major Pathway to Prompt NO Studied by Quantum/Statistical Theory Calculations and Kinetic Modeling of Rate Constant.* Proceedings of the Combustion Institute, Vol. 28, pp. 2393-2401, 2000.

[81] Website: http://www.Dieselnet.com/standards/, Available Dec. 8, 2012.

[82] Herrmann, H., Nielson, B., Gropp, C., Lehmann, J. *Mittelschwerer NFZ-Motor von Mercedes-Benz; Teil 1: Motor- und Agbasreinigungskonzept.* MTZ, Issue 10, 2012.

[83] *China's first Euro VI vehicle Diesel engine born in Yuchai.* Press release, available online: http://www.yuchai.com/gf_en/picture/1309324224054792.htm, Dec. 8, 2012.

[84] Krüger, W., Kleffel, J., Dietrich, P., Koch, D. *10,7-L-NFZ-Motor von Daimler für Euro VI und Tier 4,* MTZ, Issue 12, 2012.

[85] *World premiére: Scania Euro 6 – first engines ready for the market.* Press release P11301EN / Per-Erik Nordström, March 31, 2011.

[86] *Volvo Power: D16/D13/D11 Powertrain – Product Tour.* Product Broschure, Volvo Group North America LLC, 2010.

[87] *New Volvo engine for Euro 6.* Press release, Volvo Truck Coporation, July 5, 2012.

[88] Jaussi, F., Pfeifer, A., Csato, J. *Der IndustrieDieselmotor nach 2012 – Verbrauchssenkung trotz Emissionserfüllung?* Proceedings of the 9th Dresdener Motorenkolloquium, pp. 38-46, 2011.

[89] Wirths, M., König, G., Nording, K., Wenzel, P., Krüger, C., *Analyse der Erreichbarkeit niedrigster Rohemission am Heavy-Duty-Einzylindermotor anhand experimenteller und numerischer Untersuchungen.*, Proceedings of the 10th Annual Symposium on Combustion Diagnostics, pp. 41-62, Baden-Baden, 2012.

[90] Deslandes, W., Dupont, A., Baby, X., Charnay, G., Boree, J., *PIV Measurements of Internal Aerodynamic of Diesel Combustion Chamber*. SAE Technical Paper 2003-01-3083, 2003.

[91] Lee, W., Solbrig, C.E., Litzinger, T.A., Santoro, R.J. *Planar Laser Light Scattering for the In-Cylinder Study of Soot in a Diesel Engine*. SAE Technical Paper 902125, 1990.

[92] Schindler, K. *Integrated Diesel European Action (IDEA): Study of Diesel Combustion*. SAE Technical Paper 920591, 1992.

[93] Henle, A., *Entkopplung von Gemischbildung und Verbrennung bei einem Dieselmotor.* Doctoral thesis, Technische Universität München, 2006.

[94] Pflaum, S., Wachtmeister, G. *Dieselmotor im Grenzbereich*. MTZ Conference: Heavy Duty Engines, Bonn, Nov. 19 2008.

[95] *Standard Optics Information: HOQ 310.* Available from optics.heraeus-quarzglas.com, June 10, 2011.

[96] Petersen, B. and Miles, P., "PIV Measurements in the Swirl-Plane of a Motored Light-Duty Diesel Engine," *SAE Int. J. Engines* 4(1):1623-1641, 2011, doi:10.4271/2011-01-1285.

[97] Merola, S., Vaglieco, B.M., Corcione, F.E., Mancaruso, E. *In-Cylinder Combustion Analysis by Flame Emission Spectroscopy of Transparent CR Diesel Engine*. SAE Technical Paper 2003-01-1112, 2003.

[98] Donkerbroek, A.J., *Combustion in an optical Diesel engine studied by light-based diagnostics*. Doctoral Thesis, Radboud University Nijmegen, The Netherlands, 2010.

[99] Espey, C., Dec, J. *Diesel Engine Combustion Studies in a Newly Designed Optical-Access Engine Using High-Speed Visualization and 2-D Laser Imaging*. SAE Technical Paper 930971, 1993.

[100] Mie, G., *Beträge zur Optik trüber Medien, speziell kolloidaler Metallösungen.* Annalen der Physik, Vierte Folge, Band 25, No. 3. 1908.

[101] Suntz, R., *Laserspektroskopische Untersuchung laminarer und turbulenter Flammen.* Professorial dissertation, Fakultät für Chemie, Universität Karlsruhe (TH), 1999.

[102] van de Hulst, H.C., *Light Scattering by Small Particles.* Dover Publications, Inc., New York: 1981.

[103] Zhao, F., Hiroyasu, H. *The applications of laser Rayleigh scattering to combustion diagnostics.* Progress in Energy and Combustion Science, Vol. 19, Issue 6, 1993.

[104] Hentschel, J., *Untersuchung gepulster laminarer rußender Methan-Luft Diffusionsflammen unter erhöhtem Druck.* Doctoral thesis, Universität Karlsruhe (TH), 2006.

[105] Pinson, J., Mitchell, D., Santoro, R., and Litzinger, T., *Quantitative, Planar Soot Measurements in a D.I. Diesel Engine Using Laser-induced Incandescence and Light Scattering*, SAE Technical Paper 932650, 1993, doi:10.4271/932650.

[106] Musculus, M.P.B., Pickett, L., *Diagnostic considerations for optical laser-extinction measurements of soot in high-pressure transient combustion environments.* Combustion and Flame, Vol. 141, pp. 371-391, 2005.

[107] Musculus, M., *AEC001: Heavy-Duty Low-Temperature and Diesel Combustion Heavy-Duty Combustion Modeling.* FY 2010 DOE Vehicle Technologies Program Annual Merit Review, Advanced Combustion Engine R&D/Combustion Research. U.S. Dept. of Energy, Office of Vehicle Technologies. 2010

[108] Weeks, R.W. and Duley, W.W. *Aerosol-particle sizes from light emission during excitation by TEA CO_2 laser pulses.* Journal of Applied Physics, Vol. 45, No. 10, Oct. 1974.

[109] Eckbreth, A., *Effects of laser-modulated particulate incandescence on Raman scattering diagnostics.* Journal of Applied Physics, Vol. 48, No. 11, Nov. 1977.

[110] Melton, L., *Soot diagnostics based on laser heating.* Applied Optics, Vol. 23, No. 13, 1984.

[111] Dasch, C., *Continuous-wave probe laser investigation of small soot particles in a flame.* Applied Optics, Vol. 23, No. 13, 1984.

[112] Ni., T., Pinson, J.A., Gupta, S., and Santoro, R.J. *Two-dimensional imaging of soot volume fraction by the use of laser-induced incandescence.* Applied Optics, Vol. 34, No. 30, 1995.

[113] Zhao, H., Ladommatos, N., *Optical diagnostics for soot and temperature measurement in Diesel engines.* Progress in Energy and Combustion Science, Vol. 24, Issue 3, 1998. ISSN 0360-1285, 10.1016/S0360-1285(97)0003-6.

[114] Incropera, F., DeWitt, D., *Fundamentals of Heat and Mass Transfer.* 5th ed. John Wiley & Sons, New York: 2002.

[115] Geitlinger, H., Striebel, Th., Suntz, R., and Bockhorn, H., *Two-Dimensional Imaging of Soot Volume Fractions, Particle Number Densities and Particle Radii in Laminar and Turbulent Diffusion Flames.* in 27th Symposium (Int.) on Combustion, The Comb. Institute, Pittsburg, 1998.

[116] Velji, A., Yeom, K., Wagner, U., Spicher, U. et al., *Investigations of the Formation and Oxidation of Soot Inside a Direct Injection Spark Ignition Engine Using Advanced Laser-Techniques*. SAE Technical Paper 2010-01-0352, 2010, doi:10.4271/2010-01-0352.

[117] Stumpf, M., *Einfluss motorischer Betriebsparameter auf die Eigenschaften von Rußpartikeln und deren messtechnische Erfassung.* Doctoral thesis, Universität Karlsruhe (TH), 2008.

[118] Stumpf, M., Velji, A., Spicher, U., Jungfleisch, B., Suntz, R., Bockhorn, H. *Investigations on Soot Emission Behavior of A Common-Rail Diesel Engine during Steady and Non-Steady Operating Conditions by Means of Several Measuring Techniques*. SAE Technical Paper 2005-01-2154, 2005, doi:10.4271/2005-01-2154.

[119] Chang, H., Charalampopoulos, T.T., *Determination of the wavelength dependence of refractive indexes of flame soot.* Proceedings of the Royal Society of London, Ser. A: Math., Physics, and Engineering Sciences, V. 430, No 1880, 1990.

[120] Bougie, B., Ganippa, L.C., van Vliet, A.P., Meerts, W.L., Dam, N.J., ter Meulen, J.J. *Soot particulate size characterization in a heavy-duty Diesel engine for different engine loads by laser-induced incandescence.* Proceedings of the Combustion Institute, V. 31, Issue 1. pp. 685-691, 2007.

[121] Reissing, J., Kech, J.M., Mayer, K., Gindele, J., Kubach, H., Spicher, U., *Optical Investigations of a Gasoline Direct Injection Engine,* SAE Technical Paper 1999-01-3688, 1999, doi:10.4271/1999-01-3688.

[122] Hottel, H.C. and Broughton, F.P., *Determination of True Temperature and Total Radiation from Luminous Gas Flames: Use of Special Two-Color Optical Pyrometer.* Industrial & Engineering Chemistry Analytical Edition 1932 4 (2), 166-175.

[123] Spicher, U., Krebs, R., Dresen-Rausch, J. *Soot Formation Analysis within the Combustion Chamber of Diesel Engines by Optical Fibers,* CIMAC: Proceedings of the International Congress on Combustion Engines, Florence, IT, April 22-26, 1991.

[124] Stojkovic, B., Fansler, T., Drake, M., Sick, V., *High-speed imaging of OH* and soot temperature and concentration in a stratified-charge direct-injection gasoline engine.* Proceedings of the Combustion Institute 30 (2005), 2657-2665.

[125] Hampson, G. and Reitz, R., *Two-Color Imaging of In-Cylinder Soot Concentration and Temperature in a Heavy-Duty DI Diesel Engine with Comparison to Multidimensional Modeling for Single and Split Injections*. SAE Technical Paper 980524, 1998, doi:10.4271/980524.

[126] Yan, J. and Borman, G., *Analysis and In-Cylinder Measurement of Particulate Radiant Emissions and Temperature in a Direct Injection Diesel Engine.* SAE Technical Paper 881315, 1988, doi:10.4271/881315.

[127] Matsui, Y., Kamimoto, T., and Matsuoka, S., *A Study on the Time and Space Resolved Measurement of Flame Temperature and Soot Concentration in a D. I. Diesel Engine by the Two-Color Method.* SAE Technical Paper 790491, 1979, doi:10.4271/790491.

[128] Matsui, Y., Kamimoto, T., and Matsuoka, S., *A Study on the Application of the Two–Color Method to the Measurement of Flame Temperature and Soot Concentration in Diesel Engines.* SAE Technical Paper 800970, 1980, doi:10.4271/800970.

[129] Li, X. and Wallace, J., *In-Cylinder Measurement of Temperature and Soot Concentration Using the Two-Color Method.* SAE Technical Paper 950848, 1995, doi:10.4271/950848.

[130] Svensson, K., Mackrory, A., Richards, M., and Tree, D., *Calibration of an RGB, CCD Camera and Interpretation of its Two-Color Images for KL and Temperature.* SAE Technical Paper 2005-01-0648, 2005, doi:10.4271/2005-01-0648.

[131] J. Vattulainen, V. Nummela, R. Hernberg, and J. Kytola, *A system for quantitative imaging diagnostics and its application to pyrometric in-cylinder flame-temperature measurements in large Diesel engines.* Measurement Science and Technology 11, 103-119 (2000).

[132] di Stasio, S. and Massoli, P., *Influence of the soot property uncertainties in temperature and volume-fraction measurements by two-colour pyrometry.* Measurement Science and Technology, Vol. 5, pp. 1453-1465, 1994.

[133] Gaydon, A.G.: *The Spectroscopy of Flames.* Chapman and Hall, second edition, 1974

[134] Musculus, M., Dec, J., and Tree, D., *Effects of Fuel Parameters and Diffusion Flame Lift-Off on Soot Formation in a Heavy-Duty DI Diesel Engine*. SAE Technical Paper 2002-01-0889, 2002, doi:10.4271/2002-01-0889.

[135] Ito, T., Kitamura, T., Ueda, M., Matsumoto, T. et al., *Effects of Flame Lift-Off and Flame Temperature on Soot Formation in Oxygenated Fuel Sprays.* SAE Technical Paper 2003-01-0073, 2003, doi:10.4271/2003-01-0073.

[136] Solsjö, R., Jangi, M., Chartier, C., Andersson, Ö., Bai, X.S. *Jet-Jet Interaction in Diesel Engine Combustion*, Paper HC1-3. Proceedings of the 8th International Conference on Modeling and Diagnostics for Advanced Engine Systems, Fukuoka, Japan, July 23 – 26, 2012.

[137] Kook, S., Pickett, L.M., Musculus, M.P.B., *Influence of Diesel Injection Parameters on End-of-Injection Liquid Length Recession.* SAE International Journal of Engines, Paper Number 2009-01-1356, 2009.

[138] Hasse, C., Peters, N., *Modelling of ignition mechanisms and pollutant formation in direct-injection Diesel engines with multiple injections.* International Journal of Engine Research, Vol. 6, 2005.

[139] Siebers, D., Higgins, B., Pickett, L., *Flame Lift-Off on Direct Injection Diesel Fuel Jets: Oxygen Concentration Effects,* SAE Paper Number 2002-01-0890, 2002.

[140] Bach, F., Lüft, M., Bartosch, S., Spicher, U., *Einfluss von Diesel-Ethanol-Wasser-Emulsionskraftstoffen auf die Dieselmotor-Emissionen.* MTZ Artikel m05-11-17, Ausgabe 05/2011, pp. 408-414, 2011.

[141] Ogawa, H., Miyamoto, N. ,Kaneko, N., Ando, H., *Combustion Control and Operating Range Expansion in an HCCI Engine with Selective Use of Fuels with Different Low-Temperature Oxidation Characteristics.* SAE Japan Paper Number 20030157; SAE Paper Number 2003-01-1827, 2003.

[142] Ciniviz, M., Köse, H., Canli, E., and Solmaz, Ö. *An experimental investigation on effects of methanol blended Diesel fuels to engine performance and emissions of a Diesel engine.* Scientific Research and Essays, Vol. 6 (15), pp. 3189-3199, August 11, 2011.

[143] Ogawa, H., Miyamoto, N., Kaneko, N., Ando, H., *Combustion control and operating range expansion in an homogeneous charge compression ignition engine with direct in-cylinder injection of reaction inhibitors.* International Journal of Engine Research, Vol. 6, pp. 341-359, 2005.

[144] Hashimoto, K., *Effect of Ethanol on the HCCI Combustion.* SAE Japan Number 20077106, SAE Number 2007-01-2038, 2007.

[145] Hashimoto, K., *Inhibition Effect of Ethanol on Homogeneous Charge Compression Ignition of Heptane.* SAE Paper Number 2008-01-2504, 2008.

[146] Musculus, M., Dec., J., Tree, D., Daly, D. et al., *Effects of Water-Fuel Emulsions on Spray and Combustion Processes in a Heavy-Duty DI Diesel Engine,* SAE Technical Paper 2002-01-2892, 2002, doi:10.4271/2002-01-2892.

[147] Private communication with Mark Musculous. January 8, 2013.

[148] Angrill, O., Geitlinger, H., Streibel, T., Suntz, R., and Bockhorn, H., *Influence of Exhaust Gas Recirculation on Soot Formation in Diffusion Flames,* 28th Symposium (International) on Combustion, The Combustion Institute, Vol. 28, p. 2643, 2000.

[149] Zhang C., Atreya A., Lee K., *Sooting structure of methane counterflow diffusion flames with preheated reactants and dilution by products of combustion*, 24th International Symposium on Combustion (The Combustion Institute), pp. 1049-1057, 1992.

[150] Kohse-Höinghaus, K., Oßwald, P,. Cool, T., Kasper, T., Hansen, N., Qi, F., Westbrook, C., and Westmoreland, P., *Verbrennungschemie der Biokraftstoffe: von Ethanol bis BioDiesel,* Angewandte Chemie, Number 122, pp. 3652-3679, 2010.

[151] Reynolds, W.C. *The Element Potential Method for Chemical Equilibrium Analysis: Implementation in the Interactive Program STANJAN,* Version 3, Stanford University, 1986.

[152] Engine Combustion Network, www.sandia.gov/ecn/